International journal
for science, technics and
innovations for the industry

MACHINES TECHNOLOGIES MATERIALS

YEAR XX Issue 4 / 2026 ISSN PRINT 1313-0226
ISSN WEB 1314-507X



Published by
Scientific technical
Union of Mechanical Engineering

MACHINES. TECHNOLOGIES. MATERIALS

INTERNATIONAL SCIENTIFIC JOURNAL

ISSN PRINT 1313-0226, ISSN WEB 1314-507X, YEAR XX, ISSUE 4/ 2026

INTERNATIONAL EDITORAL BORARD

EDITOR IN CHIEF:

Georgi Popov	Technical University of Sofia	BG

MEMBERS:

Abdrakhman Naizabekov	Rudny industrial institute	KZ
Ahmet H. Ertas	Bursa Technical University	TR
Albert Albers	Karlsruhe Institut of Technology	DE
Andrzej Golabczak	Lodz University of Technology	PL
Dimitar Karaivanov	University of Chemical Technology and Metallurgy, Sofia	BG
Dobre Runchev	Ss. Cyril and Methodius University in Skopje	NM
Emilia Abadjieva	Akita University	JP
Erdem Camurlu	Akdeniz University, Antalya	TR
Eugen Sheregii	University of Rzeszow	PL
Franz Haas	Graz University of Technology	AT
Galina Nicolcheva	Technical University of Sofia	BG
Gennadii Bagliuk	Institute for Problems of Materials Science NAS of Ukraine, Kiev	UA
Georgii Raab	Ufa State Aviation Technical University	RU
Gregory Gurevich	Shamoon College of Engeeniring, Ashdod	IL
Hiroyuki Moriyama	Tokai University, Hiratsuka	JP
Idilia Batchkova	University of Chemical Technology and Metallurgy, Sofia	BG
Iryna Charniak	National Academy of Science, Belarus	BY
Ivan Kralov	Technical University of Sofia	BG
Ivan Kuric	University of Zilina	SK
Iurie Melnic	Technical University of Moldova	MD
Jaroslaw Piatkowski	Silesian University of Technology	PL
Julieta Kaleicheva	Technical University of Sofia	BG
Katia Vutova	Institute of Electronics, Bulgarian Academy of Sciences	BG
Maria Nikolova	Angel Kanchev University of Ruse	BG
Natasa Naprstkova	Jan Evangelista Purkyne University in Usti nad Labem	CZ
Nikola Šibalić	University of Montenegro	ME
Oana Dodun	Gheorghe Asachi Technical University of Iasi	RO
Ognyan Andreev	Technical University of Sofia	BG
Predrag Dasic	High Technical Mechanical School of Trstenik	RS
Rasa Kandrotaite	Kaunas University of Technology	LT
Raul Turmanidze	Georgian Technical University, Tbilisi	GE
Roumen Petrov	Ghent University	BE
Sergey Dobatkin	National University of Science and Technology "MISIS", Moscow	RU
Souren Mitra	Jadavpur University, Kolkata	IN
Svetlana Gubenko	National Metallurgical Academy of Ukraine, Dnipro	UA
Vedran Mrzljak	University of Rijeka	HR
Wu Kaiming	Wuhan University of Science and Technology	CN

TECHNICAL EDITORS:

M. Sc. Eng. Radoslav Daskalov,
M. Sc. Eng. Oleg Mihailov

All articles are published after peer review by two independent reviewers.

Scientific and technical union of mechanical engineering
108 R. S. Rakovski str., Sofia, Bulgaria
www.stumejournals.com, office@stumejournals.com

C O N T E N T S

MACHINES

Tripod type parallel robots manipulators
Zhumadil Baigunchekov, Damir Zhangabergen, Salawat Kalbiyat 127

Low-power induction motor for pumping system applications
Rachev Svilen, Yanko Takavidov 131

On the Geometric Role of the Distribution Parameter in Conic Spatial Rack Drives
Emilia Abadjieva 137

TECHNOLOGIES

A Study of Hybrid Adhesive-Mechanical Joints Between Metals and Composites Formed Using Thermal Drilling Technology
Anna Guzanová, Dagmar Draganovská 142

Automatic quality control of blanked parts based on segmentation of shear and fracture zones using a convolutional neural network
Vyacheslav Tamila, Vladimir Klubovich, Yury Kastsiuchenka, Hanna Mantsivoda 146

Thermal and acoustic insulation studies of composite lime and lime-cement plasters based on foam glass granules and thermally treated rice husks
Yonka Ivanova, Todor Partalin, Lyuben Lakov 149

New technology for producing a screw reinforcement profile from bar scrap of ferrous metals
Pavel Tsyba, Valery Chigirinsky, Sergey Kuzmin, Maxim Bogachev, Sergey Lezhnev, Evgeniy Panin 152

Monitoring the production process in production organization
Miroslav Prístavka, Hristo Beloev, Karol Durczak, Mitko Nikolov, Krzysztof Kapela 155

Features of modeling complex twist deformation for obtaining multilayer metal cord structures
Vyacheslav Tomilo, Yury Bobarikin2, Yury Martyanov 159

MATERIALS

Microstructural and Mechanical Performance of SiO_2-Reinforced Nickel-Based Nanocomposite Coatings
Regita Bendikiene, Antanas Ciuplys, Deyan Veselinov, Hristo Skulev 162

Experiment preparation with Phase Changing Materials for industrial application
Veneta Yosifova, Milena Haralampieva, Posen Petrov 167

Synthesis of polyphase materials containing pseudowollastonite
Bojidar Jivov, Mihaela Aleksandrova, Vladimir Petkov, Marieta Gacheva, Mariela Dimitrova, Stancho Yordanov, Dimo Mihaylov 171

Increasing the Durability of Agricultural Working Bodies by Creating Nanostructured Coatings Using Plasma Jet Spraying
Corneliu Munteanu, Iurie Melnic, Bogdan Istrate, Fabian Cezar Lupu, Vitali Vișanu, Constantin Zîrnescu, Vladimir Badiul 174

Tripod type parallel robots manipulators

Zhumadil Baigunchekov*, Damir Zhangabergen , Salawat Kalbiyat
Department of Mechanics, Al-Farabi Kazakh National University, 050040 Almaty, Kazakhstan
bzh47@mail.ru

Abstract: *Parallel robot manipulators (or parallel manipulators) feature closed kinematic chains. Compared to serial manipulators, they possess high load-carrying capacity, high positioning accuracy, and good dynamic characteristics. Most parallel manipulators with six degrees of freedom (DOF) utilize six legs and are commonly referred to as hexapods. This article focuses on the study of three-legged parallel manipulators, known as tripods. In comparison with hexapods, tripods offer larger workspaces and fewer singular configurations. The paper examines 3-PRRS and 3-PRPS tripods as examples, where P, R, and S denote prismatic, revolute, and spherical joints, respectively. Their structural synthesis was performed, their geometry investigated, and the inverse kinematics problem was solved.*
Keywords*: PARALLEL MANIPULATORS, TRIPODS, TRANSFORMATION MATRICES, GEOMETRY, INVERSE KINEMATICS.*

1. Introduction

Parallel robot manipulators, or parallel manipulators, are manipulators formed by connecting a moving platform to a fixed platform (or base) using various types of kinematic chains. The moving platform is the working body of the parallel manipulator, executing specified motion laws. The kinematic chains connecting the moving and fixed platforms, known as the legs of parallel manipulators, form closed loops. Closed kinematic chains in parallel manipulators increase their rigidity. Therefore, compared to serial manipulators, which have open kinematic chains, parallel manipulators possess a high load-carrying capacity, high positioning accuracy, and good dynamic characteristics. The most well-known parallel manipulator is the Stewart–Gough platform [1,2], which has 6 DOF and 6 legs of the SPS or UPS type, where S, P, and U represent spherical, prismatic, and universal kinematic pairs, respectively. The DOF of the kinematic chains is determined by the Somov–Malyshev [3] or Grübler–Kutzbach [4] formulas. This platform has been widely used as a flight simulator. Parallel manipulators with 6 DOF and 6 legs are referred to as fully parallel manipulators [5]. Fully parallel manipulators typically have small workspaces and complex singular configurations. Expanding the workspace and reducing the singular configurations of fully parallel manipulators can be achieved by decreasing the number of legs connecting the moving platform to the base. Existing three-legged parallel manipulators, known as tripods, generally possess only three DOF; thus, they cannot fully provide the specified spatial motions of the moving platform. Well-known three-legged parallel manipulators include the 3-RRR spherical parallel manipulator [6,7] (where R is a revolute joint), in which the rotation axes of all six revolute joints intersect at a single point, and the Delta robot [8]. There are certain types of 6-DOF tripods in which each of the three legs consists of spatial kinematic chains such as ESR [9] (where E is a planar joint), RES [10], RRPS [11], or URS [12]. We have developed new 6-DOF tripods of the 3-PRRS, 3-PRPS, and 3-CCC types (where C is a cylindrical joint), which are protected by patents of the Republic of Kazakhstan [13, 14]. This paper presents methods for structural synthesis, geometric analysis, and solutions to the inverse kinematics problem for the 3-PRRS and 3-PRPS tripods.

2. Structural synthesis and geometry of 3-PRRS and 3-PRPS tripods

According to the developed principle for the formation of parallel manipulators [15], they are formed by connecting the moving and fixed platforms using closing kinematic chains of the active, passive, and negative types. Figures 1 and 2 illustrate 3D CAD models of the 3-PRRS and 3-PRPS type tripods.

The 3-PRRS type tripod is formed by connecting the moving platform 4 and the fixed platform 0 via three passive PRRS-type closing kinematic chains with zero DOF. Similarly, the 3-PRPS type tripod is formed by connecting the moving platform 2 and the fixed platform 1 via three passive PRPS-type closing kinematic chains with zero DOF. These passive PRRS and PRPS closing kinematic chains do not impose geometric constraints on the motions of moving platforms 4 and 2 therefore, their 6 DOF are preserved. The input links for these tripods are selected as follows: three prismatic joints *A* located on the fixed platforms and three lower revolute joints *B* for the 3-PRRS type tripod, as well as three prismatic joints *C* for the 3-PRPS type tripod.

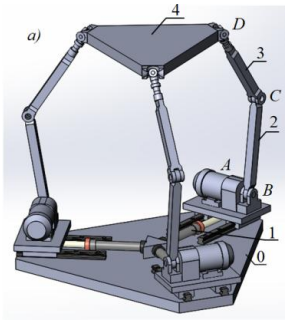


Fig. 1. *3D CAD model of the 3-PRRS type tripod.*

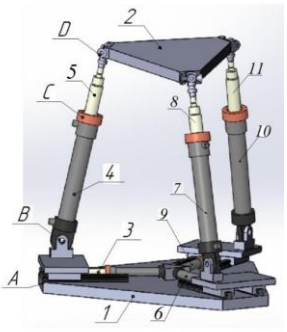


Fig.2. *3D CAD model of the 3-PRPS type tripod.*

To describe the geometry and investigate the kinematics and dynamics of the 3-PRRS and 3-PRPS type tripods, *UVW* and *XYZ* coordinate systems are rigidly attached to each element of all kinematic pairs. The *W* and *Z* axes are aligned with the axes of rotation or translation of the kinematic pair elements, while the *U* and *X* axes are directed along the common perpendiculars between the *W* and *Z* axes of two adjacent kinematic pairs. The transformation matrix $\mathbf{T}_{jk}$ between the coordinate systems $U_jV_jW_j$ and $X_kY_kZ_k$ (Fig. 3) is as follows:

$$\mathbf{T}_{jk} = \mathbf{T}_{jk}(a_{jk},\alpha_{jk},b_{jk},\beta_{jk},c_{jk},\gamma_{jk}) =$$

$$\begin{bmatrix} 1 & 0 & 0 & 0 \\ a_{jk}\cdot \mathrm{c}\gamma_{jk} + & \mathrm{c}\gamma_{jk}\cdot \mathrm{c}\beta_{jk} - & -\mathrm{c}\gamma_{jk}\cdot \mathrm{s}\beta_{jk} - & \\ +b_{jk}\cdot \mathrm{s}\gamma_{jk}\cdot \mathrm{s}\alpha_{jk} & -\mathrm{s}\gamma_{jk}\cdot \mathrm{c}\alpha_{jk}\cdot \mathrm{s}\beta_{jk} & -\mathrm{s}\gamma_{jk}\cdot \mathrm{c}\alpha_{jk}\cdot \mathrm{c}\beta_{jk} & \mathrm{s}\gamma_{jk}\cdot \mathrm{s}\alpha_{jk} \\ a_{jk}\cdot \mathrm{s}\gamma_{jk} - & \mathrm{s}\gamma_{jk}\cdot \mathrm{c}\beta_{jk} + & \mathrm{c}\gamma_{jk}\cdot \mathrm{c}\alpha_{jk}\cdot \mathrm{c}\beta_{jk} - & \\ -b_{jk}\cdot \mathrm{c}\gamma_{jk}\cdot \mathrm{s}\alpha_{jk} & \mathrm{c}\gamma_{jk}\cdot \mathrm{c}\alpha_{jk}\cdot \mathrm{s}\beta_{jk} & -\mathrm{s}\gamma_{jk}\cdot \mathrm{s}\beta_{jk} & -\mathrm{c}\gamma_{jk}\cdot \mathrm{s}\alpha_{jk} \\ c_{jk} + b_{jk}\cdot \mathrm{c}\alpha_{jk} & \mathrm{s}\alpha_{jk}\cdot \mathrm{s}\beta_{jk} & \mathrm{s}\alpha_{jk}\cdot \mathrm{c}\beta_{jk} & \mathrm{c}\alpha_{jk} \end{bmatrix} \quad (1)$$

where a_{jk} is a distance between the W_j and Z_k axes measured in the direction of the common perpendicular t_{jk} between these axes; α_{jk} is an angle between the positive directions of the W_j and Z_k axes measured about the positive direction t_{jk} according to the right-hand rule; b_{jk} is a distance from the direction t_{jk} to the direction of the X_k axis measured along the positive Z_k axis direction; β_{jk} is an angle between the positive directions of the t_{jk} and X_k axis measured according to the right-hand rule; c_{jk} is a

distance from the positive direction of the U_j axis to the direction t_{jk} measured in the positive direction of the W_j axis; γ_{jk} is an angle between the positive directions of the U_j axis and t_{jk} measured according to the right-hand rule.

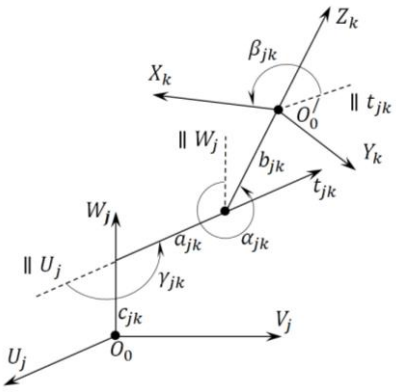


Fig. 3. *Cartesian coordinate systems* $U_jV_jW_j$ *and* $X_kY_kZ_k$.

As shown in Eq. (1), the transformation matrix $\mathbf{T}_{jk}$ has six parameters $a_{jk}, \alpha_{jk}, b_{jk}, \beta_{jk}, c_{jk}, \gamma_{jk}$, in contrast to the Denavit–Hartenberg transformation matrix [4], which consists of four parameters. Consequently, the transformation matrix $\mathbf{T}_{jk}$ provides a more comprehensive characterization of the geometry, kinematics, and dynamics of parallel manipulators, which possess more complex structural designs compared to serial manipulators. Another feature of the transformation matrix $\mathbf{T}_{jk}$ is that it allows for the derivation of both link geometry matrices and kinematic pair matrices. The transformation matrix of the coordinate systems fixed at the ends of binary links is called the matrix of binary link, and it has constant parameters characterizing the geometry of the links. The transformation matrix of the coordinate systems fixed at the two elements of each kinematic pair is called the matrix of kinematic pair, and it has variable parameters characterizing the relative motions of the kinematic pair's elements.

Figs. 4 and 5 illustrate the structural diagrams of a single leg for the 3-PRRS and 3-PRPS tripods with the selected coordinate systems.

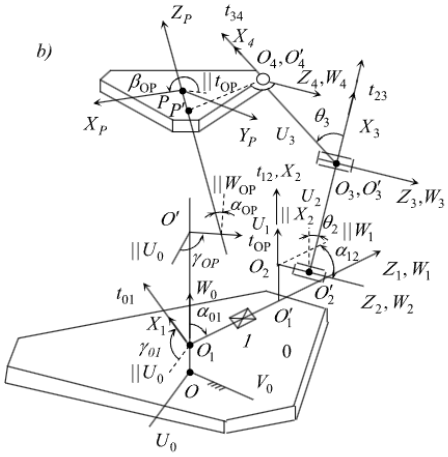


Fig. 4. *Structural diagram of the 3-PRRS type tripod leg.*

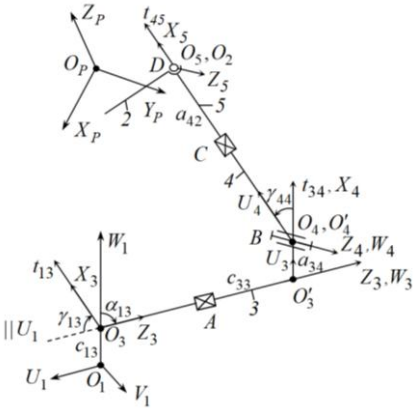


Fig. 5. *Structural diagram of the 3-PRPS type tripod leg.*

As seen from Fig. 4, each leg of the 3-PRRS type tripod has the following constant parameters: $\alpha_{01} = 90^0$, $c_{01} = OO_1$, γ_{01}, $a_{12} = O_1'O_2$, $\alpha_{12} = -90^0$, $c_{22} = O_2O_2'$, $a_{23} = O_2'O_3$, $a_{34} = O_3'O_4$ and the following variable parameters: $c_{11} = O_1O_1' = s_1$, $\gamma_{22} = \theta_2$, $\beta_{33} = \theta_3$, among which s_1 and θ_2 are input parameters, and θ_3 is an output parameter. Then, the link geometry matrices and kinematic pair matrices take the following form:

$$\mathbf{G}_{01} = \mathbf{G}_{01}(0, \alpha_{01}, 0, 0, c_{01}, \gamma_{01}) = \begin{bmatrix} 1 & 0 & 0 & 0 \\ 0 & \mathrm{c}\gamma_{01} & 0 & \mathrm{s}\gamma_{01} \\ 0 & \mathrm{s}\gamma_{01} & 0 & -\mathrm{c}\gamma_{01} \\ c_{01} & 0 & 1 & 0 \end{bmatrix}, \quad (2)$$

$$\mathbf{G}_{12} = \mathbf{G}_{12}(a_{12}, -90^{\mathrm{o}}, 0, 0, 0, 0) = \begin{bmatrix} 1 & 0 & 0 & 0 \\ a_{12} & 1 & 0 & 0 \\ 0 & 0 & 0 & 1 \\ 0 & 0 & -1 & 0 \end{bmatrix}, \quad (3)$$

$$\mathbf{G}_{23} = \mathbf{G}_{23}(a_{23}, 0, 0, 0, 0, 0) = \begin{bmatrix} 1 & 0 & 0 & 0 \\ a_{23} & 1 & 0 & 0 \\ 0 & 0 & 1 & 0 \\ 0 & 0 & 0 & 1 \end{bmatrix}, \quad (4)$$

$$\mathbf{G}_{34} = \mathbf{G}_{34}(a_{34}, 0, 0, 0, 0, 0) = \begin{bmatrix} 1 & 0 & 0 & 0 \\ a_{34} & 1 & 0 & 0 \\ 0 & 0 & 1 & 0 \\ 0 & 0 & 0 & 1 \end{bmatrix}, \quad (5)$$

$$\mathbf{P}_1^{\,P} = \mathbf{P}_1^{\,P}(0, 0, 0, 0, c_{11}, 0) = \begin{bmatrix} 1 & 0 & 0 & 0 \\ 0 & 1 & 0 & 0 \\ 0 & 0 & 1 & 0 \\ s_1 & 0 & 0 & 1 \end{bmatrix}, \quad (6)$$

$$\mathbf{P}_2^{\,R} = \mathbf{P}_2^{\,R}(0, 0, 0, 0, b_{12}, \gamma_{22}) = \begin{bmatrix} 1 & 0 & 0 & 0 \\ 0 & \mathrm{c}\theta_2 & -\mathrm{s}\theta_2 & 0 \\ 0 & \mathrm{s}\theta_2 & \mathrm{c}\theta_2 & 0 \\ b_{12} & 0 & 0 & 1 \end{bmatrix}, \quad (7)$$

$$\mathbf{P}_3^{\,R} = \mathbf{P}_3^{\,R}(0, 0, 0, \beta_{33}, 0, 0) = \begin{bmatrix} 1 & 0 & 0 & 0 \\ 0 & \mathrm{c}\theta_3 & -\mathrm{s}\theta_3 & 0 \\ 0 & \mathrm{s}\theta_3 & \mathrm{c}\theta_3 & 0 \\ 0 & 0 & 0 & 1 \end{bmatrix}, \quad (8)$$

As shown in Fig. 5, each leg of the 3-PRPS type tripod has the following constant parameters: $\alpha_{13}=90^0$, $c_{13}=O_1O_3$, γ_{13}, $a_{34}=O_3^{'}O_4$, a_{34}, $\alpha_{34}=-90^0$ and the following variable parameters: $c_{33}=O_3O_3^{'}=s_3, a_{42}=O_4O_2=s_5, \gamma_{44}=\theta_4$, of which s_3 and s_5 are input parameters, and θ_4 is an output parameter. Then, the link geometry and kinematic pair matrices take the following form:

$$\mathbf{G}_{13}=\begin{bmatrix}1 & 0 & 0 & 0\\ 0 & \cos\gamma_{13} & 0 & \sin\gamma_{13}\\ 0 & \sin\gamma_{13} & 0 & -\cos\gamma_{13}\\ c_{13} & 0 & 1 & 0\end{bmatrix}, \quad (9)$$

$$\mathbf{P}_3^{\,P}=\begin{bmatrix}1 & 0 & 0 & 0\\ 0 & 1 & 0 & 0\\ 0 & 0 & 1 & 0\\ s_3 & 0 & 0 & 1\end{bmatrix}, \quad (10)$$

$$\mathbf{G}_{34}=\begin{bmatrix}1 & 0 & 0 & 0\\ a_{34} & 0 & 0 & -1\\ 0 & 1 & 0 & 0\\ 0 & 0 & -1 & 0\end{bmatrix}, \quad (11)$$

$$\mathbf{P}_4^{\,P}=\begin{bmatrix}1 & 0 & 0 & 0\\ 0 & \cos\theta_4 & -\sin\theta_4 & 0\\ 0 & \sin\theta_4 & \cos\theta_4 & 0\\ 0 & 0 & 0 & 1\end{bmatrix}, \quad (12)$$

$$\mathbf{P}_5^{\,P}=\begin{bmatrix}1 & 0 & 0 & 0\\ 0 & 1 & 0 & 0\\ 0 & 0 & 1 & 0\\ s_5 & 0 & 0 & 1\end{bmatrix}, \quad (13)$$

3. Inverse kinematics of 3-PRRS and 3-PRPS type tripods

In inverse kinematics, the pose (position a orientation) of the coordinate system $PX_pY_pZ_p$, attached to the moving platform, is given. It is necessary to determine the input parameters of the tripods. The solution to the inverse kinematics problem for parallel robots is crucial, as the obtained input parameter values are used to control the robot's motion.

Let us consider the solution to the inverse kinematics problem for the 3-PRRS type tripod. To do this, we determine the coordinates of the spherical joints $O_{4,i}$ of the moving platform in the absolute coordinate system $OU_oV_oW_o$ through the specified coordinates of the $PX_pY_pZ_p$ coordinate system using the following equation:

$$[1, U_{O_{4,i}}, V_{O_{4,i}}, W_{O_{4,i}}]^{\mathrm{T}}=\mathbf{T}_{OP}\mathbf{G}_{P4}[1,0,0,0]^{\mathrm{T}} \quad (14)$$

and through the *ABCD* legs by the equation

$$[1, U_{O_{4,i}}, V_{O_{4,i}}, W_{O_{4,i}}]^{\mathrm{T}}=\mathbf{G}_{01}\mathbf{P}_{1i}^{P}\mathbf{G}_{12}\mathbf{P}_{2i}^{R}\mathbf{G}_{23}\mathbf{P}_{3i}^{R}\mathbf{G}_{34}[1,0,0,0]^{\mathrm{T}}. \quad (15)$$

Expanding Eq. (15) and substituting the values of the spherical joint coordinates from Eq. (14), we obtain:

$$\left.\begin{aligned} U_{O_{4,i}} &= -b_i\mathrm{c}\gamma_i + s_i\mathrm{s}\gamma_i - f_i\mathrm{s}\gamma_i\mathrm{s}\theta_{2,i} - g_i\mathrm{s}\gamma_i\mathrm{s}\theta_{23,i}\\ V_{O_{4,i}} &= -b_i\mathrm{s}\gamma_i - s_i\mathrm{c}\gamma_i + f_i\mathrm{c}\gamma_i\mathrm{s}\theta_{2,i} + g_i\mathrm{c}\gamma_i\mathrm{s}\theta_{23,i}\\ W_{O_{4,i}} &= c_i + a_i + f_i\mathrm{c}\theta_{2,i} + g_i\mathrm{c}\theta_{23,i}\end{aligned}\right\}, \quad (16)$$

where $\theta_{23,i}=\theta_{2,i}+\theta_{3,i}$.

An analysis of the system of Eq. (16) shows that the first two equations are linearly dependent. We transform the first and third equations of system (16) into the following form:

$$A_i\mathrm{s}^2\theta_{2,i}-B_i\,\mathrm{s}\theta_{2,i}+C_i=0, \quad (17)$$

where $A_i, B_i,$ and C_i are known parameters

$$A_i=(s_i-K_i)^2+M_i^2,\ B_i=2(f+g\,\mathrm{c}\theta_{3,i})(s_i-K_i),$$
$$C_i=(f+g\,\mathrm{c}\theta_{3,i})^2-M_i^2,\ K_i=\frac{U_{O_{4,i}}+b\,\mathrm{c}\gamma_i}{\mathrm{s}\gamma_i},\ M_i=W_{O_{4,i}}-c-a. \quad (18)$$

From Eq. (17), and also from the first and third equations of system (16), two possible values of the parameters $\theta_{2,i}$ and $\theta_{3,i}$ can be determined:

$$\theta_{2,i}=\mathrm{s}^{-1}\frac{B_i\pm\sqrt{B_i^2-4A_iC_i}}{2A_i},\ \theta_{2,i}=\pi-\mathrm{s}^{-1}\frac{B_i\pm\sqrt{B_i^2-4A_iC_i}}{2A_i},$$
$$\theta_{3,i}=\pm\mathrm{c}^{-1}\frac{(s_i-K_i)^2+M_i^2-f^2-g^2}{2fg}. \quad (19)$$

which correspond to two assembly configurations of each tripod leg.

Let us consider the solution to the inverse kinematics problem of a 3-PRPS type tripod. We shall determine the coordinates of the spherical joints *D* of the moving platform in the absolute coordinate system $OU_oV_oW_o$ in terms of the given coordinates of the $PX_pY_pZ_p$ coordinate system using the equation:

$$[1, U_D, V_D, W_D]^{\mathrm{T}}=\mathbf{T}_{OP}\mathbf{G}_{PO_5}[1,0,0,0]^{\mathrm{T}}. \quad (20)$$

and via the *OABCD* legs using the equation

$$[1, U_D, V_D, W_D]^{\mathrm{T}}=\mathbf{G}_{13}\mathbf{P}_1^{P}\mathbf{G}_{34}\mathbf{P}_4^{R}\mathbf{P}_5^{P}[1,0,0,0]^{\mathrm{T}}, \quad (21)$$

By expanding Eq. (21) and substituting the values for the coordinates of joints *D* from Eq. (20), we obtain:

$$\left.\begin{aligned} s_3\cdot\mathrm{s}\gamma_{13}-s_5\cdot\mathrm{s}\gamma_{13}\cdot\mathrm{s}\theta_4 &= U_D\\ -s_3\cdot\mathrm{c}\gamma_{13}+s_5\cdot\mathrm{c}\gamma_{13}\cdot\mathrm{s}\theta_4 &= V_D\\ c_{13}+a_{34}+s_5\cdot\mathrm{c}\theta_4 &= W_D\end{aligned}\right\}. \quad (22)$$

An analysis of the system of equations (22) showes that the first two equations are linearly dependent. Therefore, the parameter s_3 can be chosen free.

After transforming the first and the third equations of system (22), we obtain

$$\left.\begin{aligned} s_5\cdot\mathrm{s}\theta_4 &= s_3-F\\ s_5\cdot\mathrm{c}\theta_4 &= K\end{aligned}\right\}, \quad (23)$$

where $F=\frac{U_D}{\mathrm{s}\gamma_{13}}$, $K=W_D-c_{13}-a_{34}$.

From the system of equations (22) we obtain the parameters s_5 and θ_4

$$s_5 = \sqrt{(s_3 - F)^2 + K^2}, \quad (24)$$

$$\theta_4 = \mathrm{c}^{-1}\left(\frac{M \pm \sqrt{2 - M^2}}{2}\right), \quad (25)$$

where $M = \frac{s_3 - F + K}{s_5}$.

4. Conclusions

The article outlines the fundamental concepts of parallel manipulators and their advantages over serial manipulators, such as high load-carrying capacity, high positioning accuracy, and good dynamic characteristics due to the presence of closed kinematic chains. A comparison is conducted between two types of parallel manipulators, hexapods and tripods demonstrating that tripods possess larger workspaces and fewer singular configurations compared to hexapods. Structural synthesis was performed, the geometry was studied, and the inverse kinematics problems were solved for 3-PRRS and 3-PRPS type tripods. These tripods are formed by connecting the moving and fixed platforms via passive closing kinematic chains of the PRRS and PRPS types with zero DOF. To investigate geometry and kinematics, a generalized transformation matrix with six parameters was formulated, serving as the basis for obtaining the geometry matrices of the links and kinematic pairs of the tripods under consideration. Using these transformation matrices, the inverse kinematics problems for the 3-PRRS and 3-PRPS type tripods were solved.

5. Acknowledgment

This work was supported by the Ministry of Science and Higher Education of Kazakhstan (Grant No. AP23488130 «Development and research of a domestic social humanoid robot»).

6. References

[1] Gough, V. E. and Whitehall, S.G. (1962). Universal tyre test machine. Proceedings, Ninth International Technical Congress F.I.S.I.T.A., 117 (Institute of Mechanical Engineers).

[2] Stewart, D. (1965). A platform with six degrees-of-freedom. Proc. Inst. Mech. Engrs., Vol. 180, Part 1, No. 15, pp. 371-386.

[3] Artobolevskiy, I.I. (1988). Theory of mechanisms and machines (in Russian). Moscow, Nauka.

[4] Lung-Wen Tsai. (1999). Robot Analysis. The Mechanics of Serial and Parallel Manipulators. A Wiley – Interscience Publication, New York.

[5] Chablat, D., Wenger, Ph. (1989). Working modes and aspects of fully parallel manipulators. IEEE International Conference on Robotics and Automation, pp. 1964-1969.

[6] Gosselin, E., Angeles J. (1989). The optimum kinematic design of a spherical three degree-of-freedom parallel manipulator. Journal of Mech. Transm. Autom. Des., 111(2), pp. 202-207.

[7] Gosselin, C., St-Pierre, E., and Gagni, M. (1996). On the development of the Agile Eye. IEEE Robotics & Automation Magazine. Vol. 3, pp. 29-37.

[8] Clavel, R. Device for displacing and positioning an element in space. WIPO Patent, W087/03528.

[9] Tsai, L. W., Tahmasebi, F. (1993). Synthesis and analysis of a new class of six degrees-of-freedom parallel manipulators. Journal of Robotics System. Vol. 10, No. 5, pp. 561-580.

[10] Collins, C. L., Long, G. L. (1995) The singularity analysis of an in-parallel hand controller for force-reflected teleoperation. IEEE Transactions on Robotics and Automation. Vol. 11, No. 5, pp. 661-669.

[11] Alizade, R. I., Tagiyev, N. R., Duffy, J. A. (1994). Forward and reverse displacement analysis of a 6-DOF in-parallel manipulator. Mechanism and Machine Theory. Vol. 29, No. 1, pp. 115-124.

[12] Clearly, C., Ubel, M. (1994). Jacobian formulation for a novel 6-DOF parallel manipulator. IEEE International Conference on Robotics and Automation. Vol. 3, pp. 2377-2382.

[13] Baigunchekov, Zh., Ceccarelli, M., Nurakhmetov, B., Myrzageldieva, Zh. Parallel manipulator. Patent 20725 of the Republic of Kazakhstan. 16.02.2009.

[14] Baigunchekov, Zh., Kadyrov Zh. et al. Tripod-Manipulator, Invention Patent No. 36849, Republic of Kazakhstan, 2024.

[15] Baigunchekov, Zh., Laribi, M. A., Carbone, G., Zhumasheva, Zh., Sagitzhanov, B. (2024). Structural-parametric synthesis of path-generating mechanisms and manipulators. Robotics, 13(10), 149.

Low-power induction motor for pumping system applications

Rachev Svilen[1], Yanko Takavidov[2]
Technical University – Gabrovo[1], Republic of Bulgaria
Caproni JSC, Kazanlak[2], Republic of Bulgaria
srachev@tugab.bg

Abstract: *Paper deals with a newly designed low-power three-phase induction electric motor for continuous duty cycle operation with application mainly in pumping system. The main features are presented. The problems and solutions related to the sizing and optimization of the motors during design according to different criteria and conditions are analyzed, with energy efficiency being the main determinant. Numerous graphical results obtained during the design are presented.*

Keywords: *ELECTRIC MACHINES, INDUCTION MOTOR, WATER PUMPS, OPERATING CHARACTERISTICS, PRODUCT DESIGN*

1. Introduction

To set working machines in motion, the main engine is the electric motor and, therefore, the main type of drive is the electric drive.

Currently, there is a widespread orientation towards energy-efficient technical solutions globally in the world and Europe and in this regard the development of this direction in terms of electricity consumption with a view to optimizing electricity costs. The application of an optimal in this regard electric drive, the main component of which is an electric motor, guarantees not only the energy-efficient operation of entire systems, but also low electricity costs for the industry. In other words – the most expensive energy in the industry is the unnecessarily consumed and the optimal electric drive will guarantee not only the energy-efficient operation of a given system, but also low electricity costs [1].

The creation of any mechanical unit is currently directly related to the design of electrical equipment. In this case, one must have a good knowledge of mechanical equipment and technologies, methods of speed regulation, calculation of transient processes of electric drives, and selection of the power of electric motors. The appropriate design of rotating electrical machines is the basis for achieving local and global electrical energy efficiency.

2. Some considerations

Caproni JSC – Kazanlak is a leading manufacturer of hydraulic components and systems for use in mobile and stationary industrial equipment. One of the company's innovations is the development of AC electric motors with the possible application of frequency regulation and vector control to them [2].

Modern electric drive is developing mainly in the following direction – simplification of the transmission mechanism between the electric motor and the working machine. This is achieved mainly by using electric motors that allow regulation of the rotational frequency, which avoids the complication of the transmission mechanisms. In this case, things such as the steady-state torque-speed curve, the dynamic performance required, the inertia of the load, the pattern of operation (continuous or intermittent), etc. are important [3].

Speed control is the forced change in the speed of an electric drive. The term ‘speed control’ should not be confused with the natural change in speed that occurs in an electric drive due to changes in the load on the shaft of a running machine. Speed regulation is achieved by additional action on the driving electric motor or the gear system of the production mechanism. This action can be performed by a person or by a special automatic device. For induction motors, pulse width modulation (PWM) inverters are suitable for control. Voltage source PWM inverters are popular because they are readily applied to different types of motor and load. That's why they are called ‘the industrial work horse’ and are the most widely used drives. Method of torque/speed control can be Field Oriented Control (FOC) or Direct Torque Control (DTC), as well as Simpler Scalar (V/f) variant [3].

In the historical development of drives, mechanical control methods were the first step in the transition from unregulated to regulated drives. Currently, electrical control prevails, which has a number of advantages in terms of technical and economic indicators. In electrical control, the aim should be to ensure that the characteristics across the entire range have high rigidity and that the electric motor has sufficient overload capacity. The electrical method of regulation creates broad opportunities for automation of the regulation process and allows to eliminate mechanical regulating devices and thus to increase the reliability of the operation of the installations and to simplify their design.

By the way, it should be noted that for self-ventilated electric motors, the reduction in speed must correspond to the reduction in permissible losses in them. At low speeds, these electric motors must operate at currents lower than the nominal, and therefore the permissible torque is reduced in proportion to the reduction in speed.

Dynamic loads occurring during starting and stopping of electric drives increase losses in the motor, but since they are short-term compared to the duration of operation in a fixed mode, their influence on the heating of the electric motor is negligible. Therefore, in many cases, under the conditions of heating, it can be assumed for a short time that the torque of the electric motor is much greater than the rated one.

In addition to heating, there are other factors that limit the permissible overload of electric motors – for each there is a limit value of the moment, permissible under the conditions of normal operation of the electric motor, which should not be exceeded even briefly. It is this ratio of the maximum permissible moment to the nominal one that is called the overload capacity of the electric motor.

The peculiarity of the ATM range of AC electric motors (manufactured by Caproni JSC) is that maximum unification of the equipment used has been achieved in the implementation of products in the usual IE1 (Standard Efficiency) and IE2 (High Efficiency) energy class. The already available designs for the various types of products from the basic range are a prerequisite for implementing the IE3 energy class (Premium Efficiency). Electric motors with the ATM designation are available in standard and special designs according to their intended purpose, with the different combinations not changing the connection dimensions of the basic designs. In all products, the body and bearing shields are cast from aluminum alloy. All versions are ventilated except those operating immersed in an oil tank. More special versions are also possible, such as:

- tropical performance;
- with protection degree IP55 or IP56;
- for other supply voltage and frequency;
- for operating modes other than S1;
- with parameters different from those of the basic versions;
- with second output shaft end;
- for operation immersed in hydraulic oil.

The International Electrotechnical Commission (IEC) is an organization based in Geneva that publishes and promotes worldwide mechanical and electrical standards for electric motors, among other documents. IEC uses duty cycle (mode) designations (categories) S1 ... S10 to describe the operating conditions of electric motors – IEC 60034-2-1:2024 [4]. The modes of electric motors, in addition to specifying their operating parameters and duty cycles, also determine the temperature rise (insulation class), frame size (the physical dimensions of the electric motor), housing type, service factor, etc. In typical modes, serial electric motors should operate while the reliable operation of the machine is guaranteed by the manufacturer if the electric motor is operated in the mode specified in its passport at the rated load. Rapid failure is usually due to the fact that the electric motor is selected without taking into account the required rated mode.

It is necessary to clarify that the standards are recommended, i.e. they are not mandatory. A given manufacturer declares that his products comply with relevant standards, but this is for the purpose of seeking and selling his products. However, the ordinances in Bulgaria, as well as the regulations, directives and decisions created by the European Commission, are mandatory for implementation..

Electric motors for applications in pumps, fans, compressors, conveyors, operate in S1 mode (continuous duty cycle). This mode is characterized by operation at a constant load without interruption and with a sufficient duration to reach thermal equilibrium (thermal equilibrium is the state reached when the temperature rise of the machine does not vary by more than 2 degrees on the Kelvin scale per hour) [4].

3. Specifics of the designed electric motor

The induction motor under consideration is designed for operating mode S1 according to IEC, cooled by self-ventilation – code IC01, thermal protection is implemented with a Pt1000 thermistor in the stator winding (equipment upon customer request), and the insulation of the stator winding has a heat resistance class H (180^{o}C). Parameter values and general view of an electric motor ATM are given in Table 1 and Figure 1, respectively.

The design is carried out with specified inner and outer diameters of the blades, with a certain number and dimensions of the stator and rotor channels. The possibilities for varying the independent variables are limited by the conditions for minimum dimensions and mass, as well as technological factors. Regarding the moment of inertia of the rotor - it is known that higher rotor inertias increase energy consumption when changing speed, with more compact dimensions the rotor inertia is smaller [1].

Partial optimization tasks have been solved with a maximum efficiency criterion and constraints on the current density in the stator and rotor windings. These constraints are imposed to achieve permissible winding temperatures. The parameters of the equivalent circuit, the currents in the windings, losses, powers, etc. have been determined. The results obtained allow us to estimate the distribution of magnetic induction in the sections of the magnetic circuit, to determine the magnetic flux through the air gap and the electromagnetic moment.

For the rated speed, the overload capacity of the electric motor is determined by the maximum torque factor. The maximum torque factor is usually greater than 2, where the stator current is more than twice the rated motor current. The air gap has the greatest influence on the value of the magnetizing current of induction motors. In turn, the magnetizing current determines the current and losses in the stator winding and the power factor. The production of induction motors with an optimal air gap depends on the design of the bearing and the level of the manufacturing process.

Table 1: *Parameter values for the considered induction motor*

Parameters	
Description	**Data**
Type	ATM 0.55-1500-L70
Duty cycle	S1
Connection (stator)	Y
Rated power	0.55 kW
Stator terminal phase voltage	230 V
Line-line supply voltage	400 V
Fundamental frequency	50 Hz
Number of pole pairs	4
Airgap	0.25 mm
Shaft diameter	25 mm
Copper diameter	0.63 mm
Synchronous rotational frequency	1500 rpm
Shaft rotational frequency	1427 rpm
Rated slip	0.04493
Rotor moment of inertia	0.0010668 kgm^2
Rated torque	3.68 Nm
Starting torque	1.73 p.u.
Maximum torque	2.68 p.u.
Phase current	1.3368 A
Starting current	4.54 p.u.
Maximum current	3.2 p.u.
Rated efficiency	80.514%
Phase resistance	11.30 Ω
Line-line resistance	22.60 Ω
Referred rotor resistance	10.74 Ω
Stator leakage reactance	7.35 Ω
Referred rotor leakage reactance	25.43 Ω
Magnetizing reactance (saturated)	274 Ω
Airgap flux density (mean)	0.5618 T
Stator copper losses (analytic on load)	60.58 W
Rotor copper losses (analytic on load)	29.15 W
Stray load losses (analytic on load)	17.01 W
Stator iron losses (total, analytic on load)	25.91 W
Rotor iron losses (total, analytic on load)	0.4707 W
Total losses (analytic on load)	133.10 W

The selected design scheme and the precision in machining the stator and rotor packages, bearing shields and shaft create the possibility of achieving a small and uniform air gap in the motors.

The machine winding and laying of the sections, the channel filling factor and the quality of the impregnation of the stator winding largely determine the heat dissipation and the temperature state of the winding. The resistance of the winding, the losses in it and the efficiency depend on the temperature.

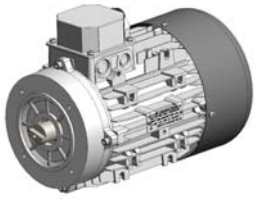


Fig. 1 *General view of an electric motor ATM.*

The considered induction motor can be used to drive pumps designed for household use at home and garden, for fixed installation and pumping water from wells and other passive waters. Such pumps are designed to handle clean, clear or moderately contaminated water with solid particles at the declared maximum volume and are suitable for the following applications [5]:

- irrigation and watering of lawns, beds and vegetable gardens;
- the pumping of water reservoirs and ponds;
- for water-drainage from wells, tanks and rainwater tanks;
- the pump is suitable for pumping clean water, rain water and chlorinated water (water pools).

Figure 2 presents an example diagram for using a pump driven by an induction motor [5].

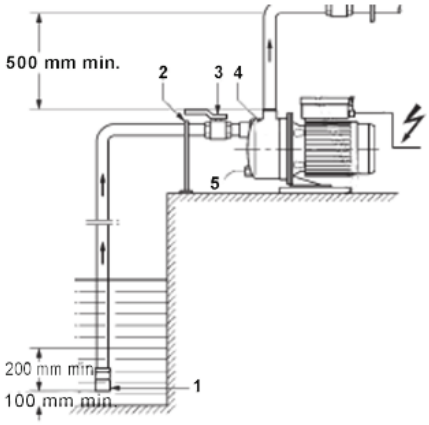


Fig. 2 *General diagram of a pump with an induction motor (depicted elements: 1- suction with filter and check valve; 2 – suction pipe support; 3 – suction pipe slide valve; 4 – water filling plug (bleeding valve); 5 – pump water drain plug).*

4. Results obtained

Below in Fig. 3 ÷ Fig. 12 are presented in graphical form the results for the designed induction electric motor. An appropriate software toolkit for electrical machines has been used – Ansys® Motor-CAD [6].

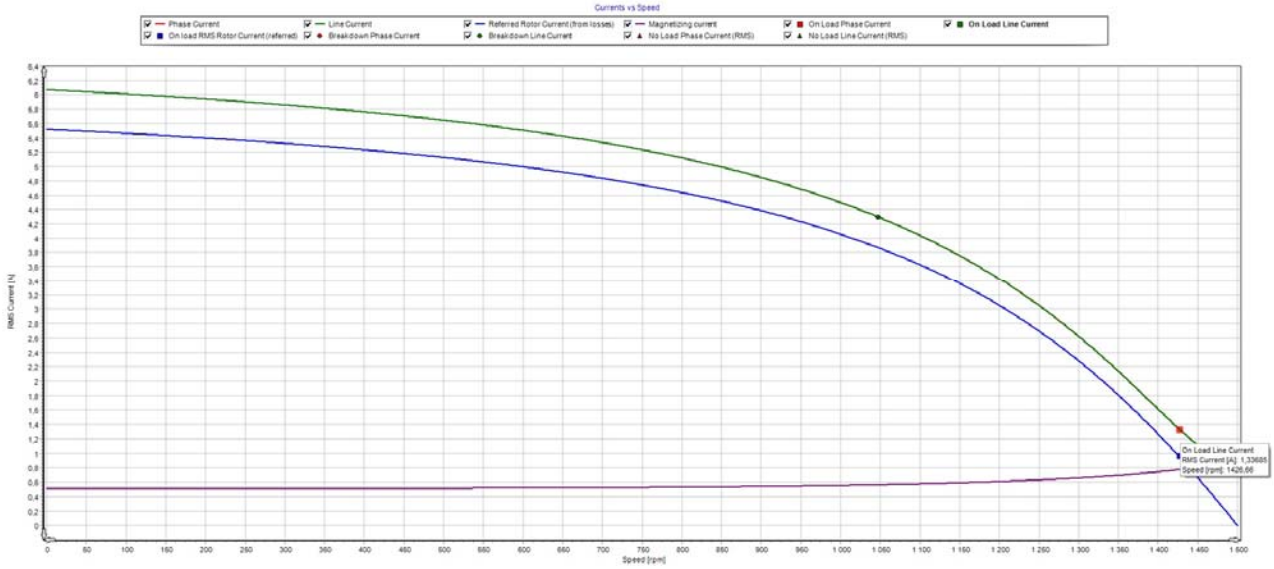


Fig. 3 *Currents vs speed characteristics*
(green colored – line current, blue colored – referred rotor current, purple colored – magnetizing current).

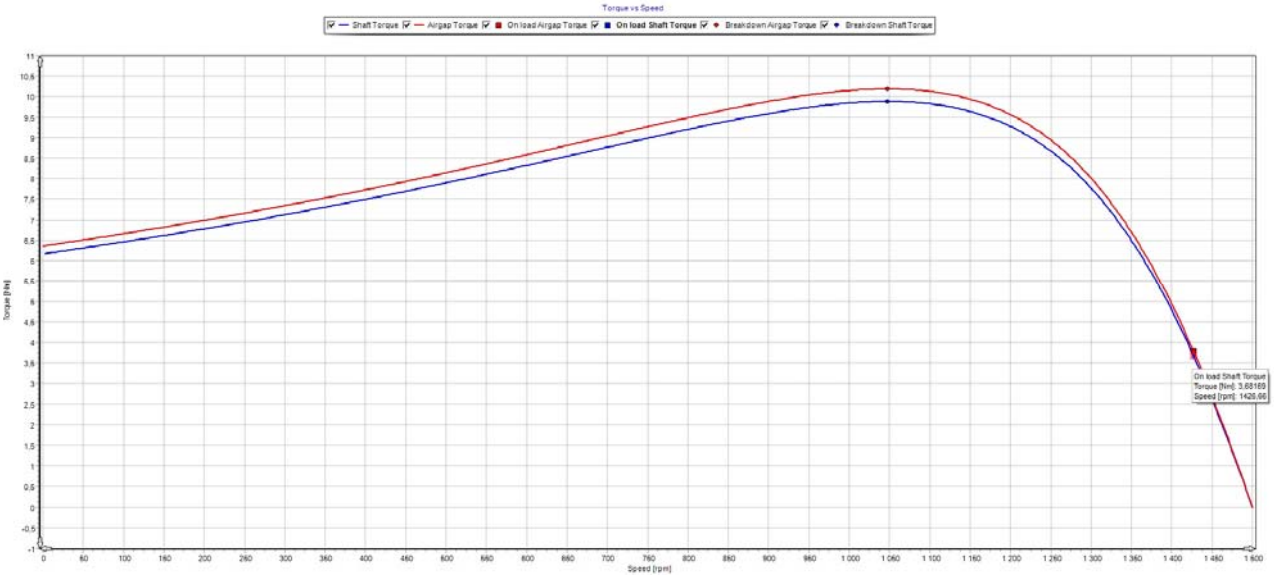


Fig. 4 *Torque vs speed characteristics*
(red colored – on load airgap torque, blue colored – on load shaft torque).

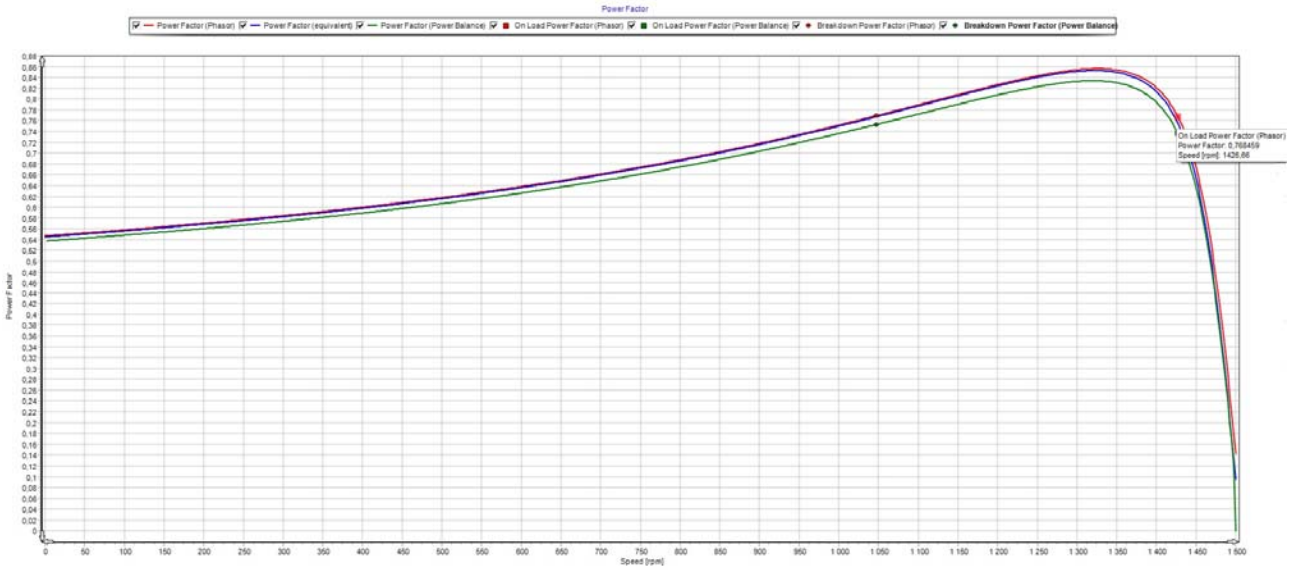


Fig. 5 *Power factor vs speed characteristics.*

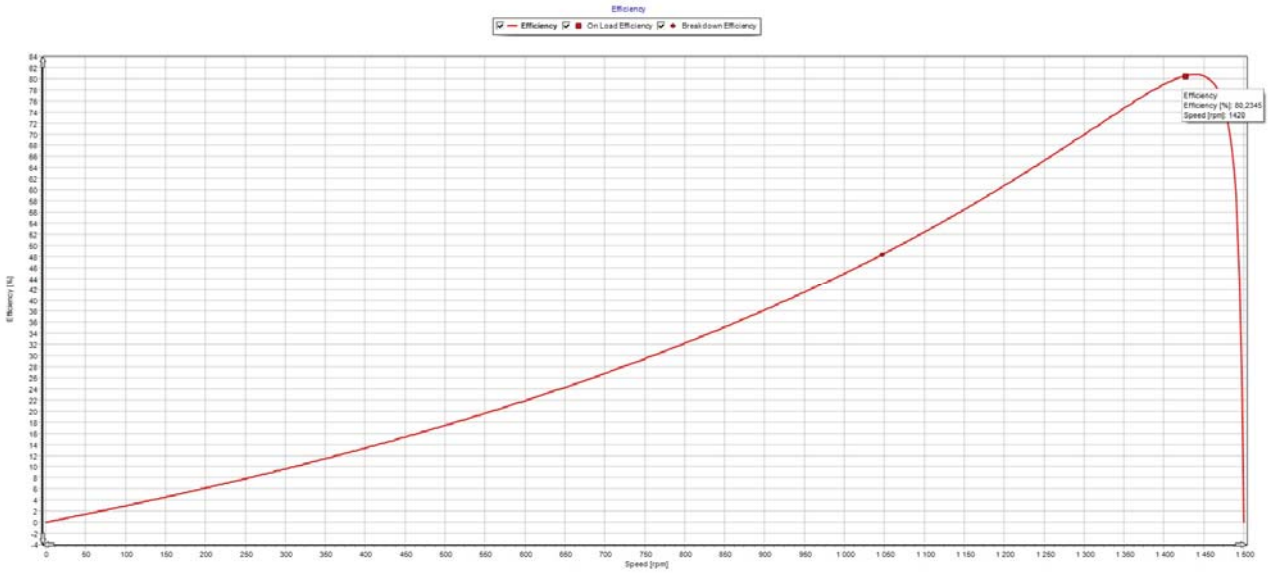


Fig. 6 *Efficiency vs speed characteristic.*

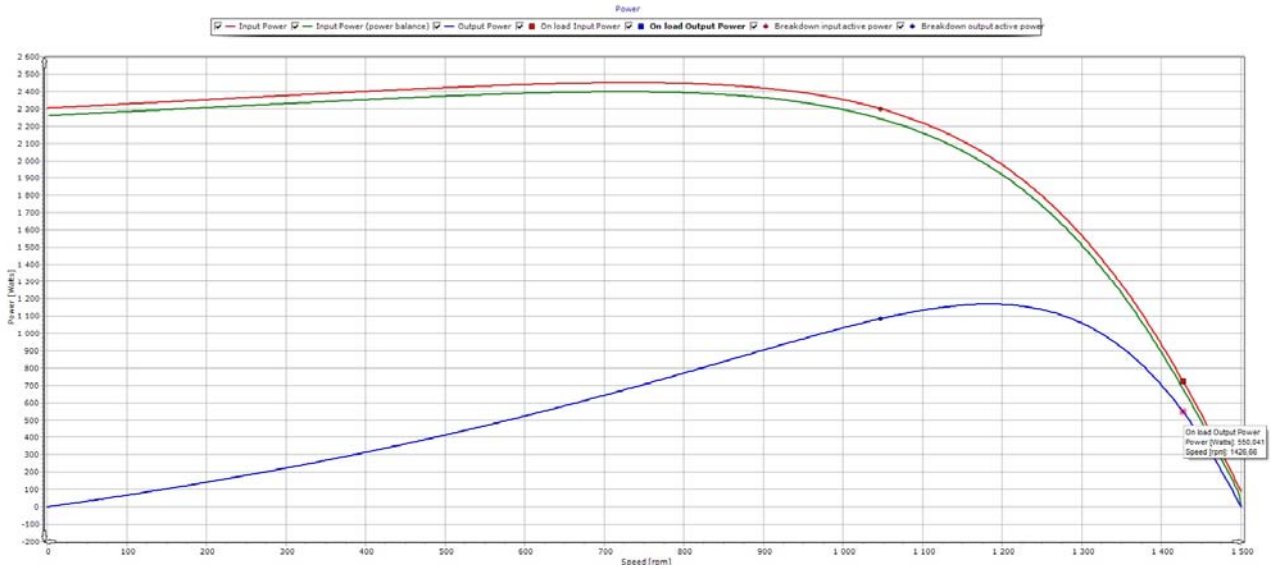


Fig. 7 *Power vs speed characteristics*
(red colored – input power consumed, green colored – input power consumed, power balance, blue colored – output power).

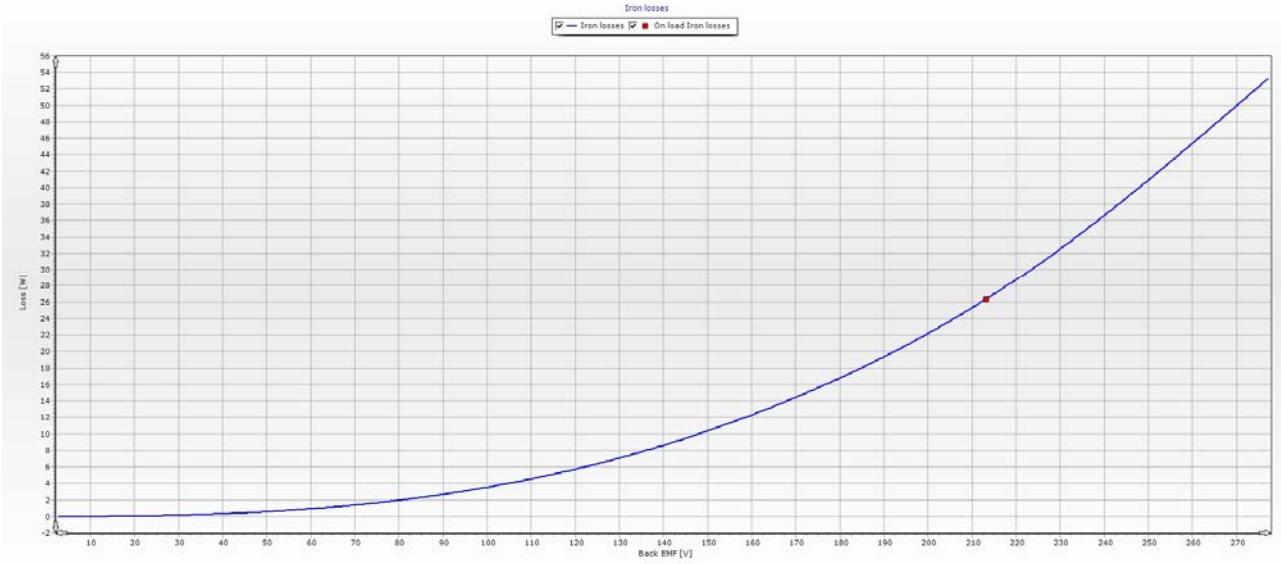


Fig. 8 *Iron losses vs back e.m.f.*

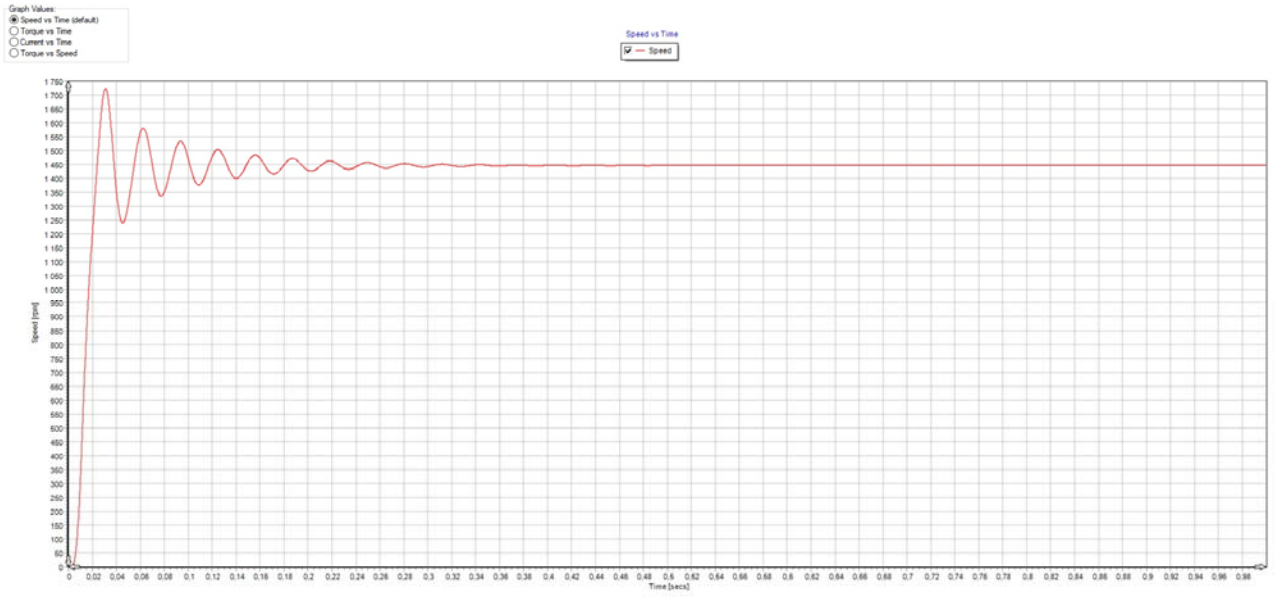


Fig. 9 *Speed vs time characteristic.*



Fig. 10 *Torque vs time characteristic.*

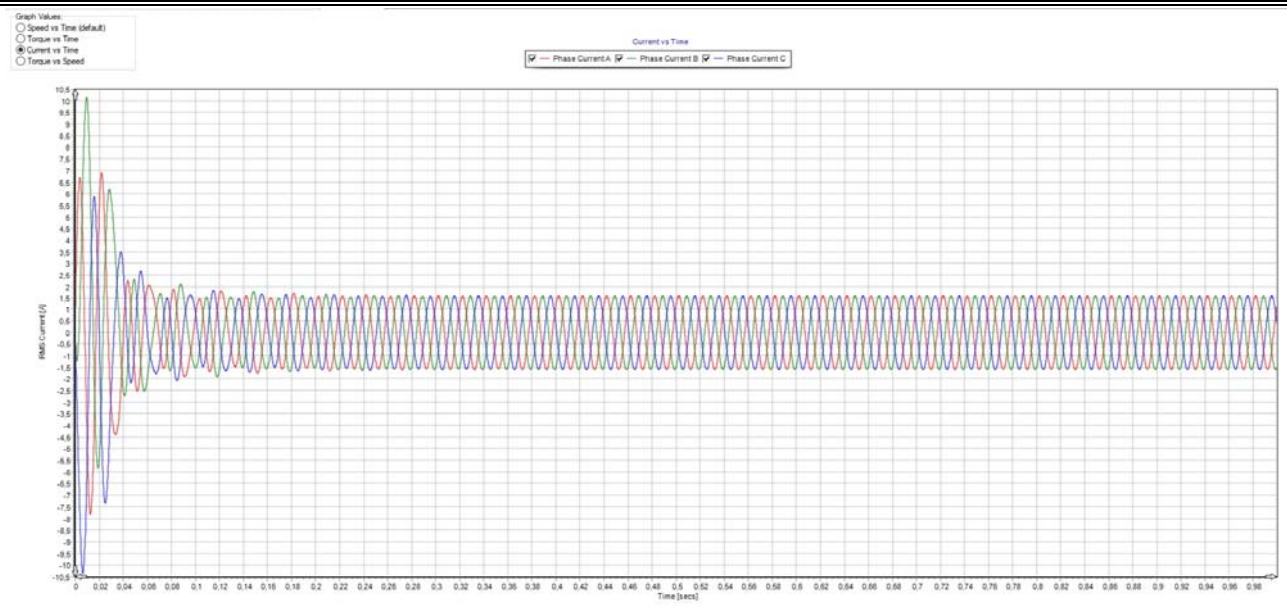


Fig. 11 *Currents vs time characteristics*
(red colored – phase current A, green colored – phase current C, blue colored – phase current C).

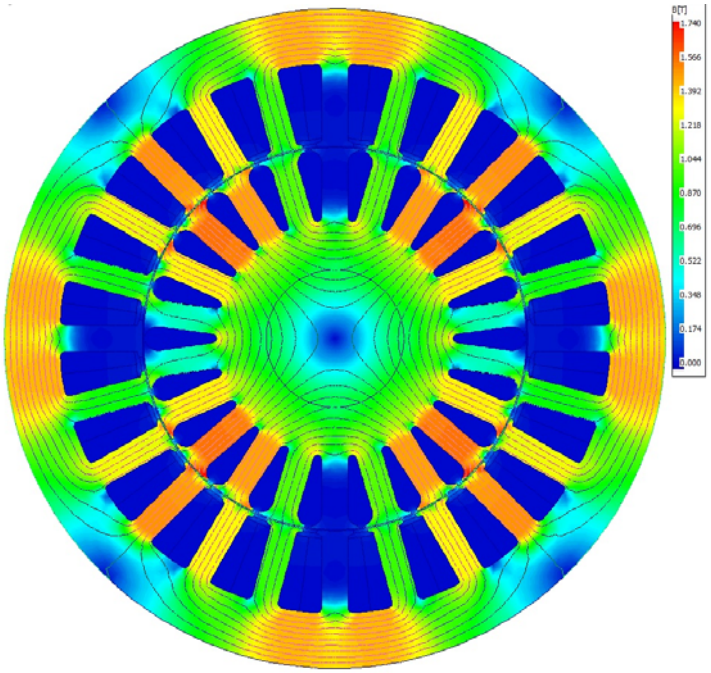


Fig. 12 *Flux density [T].*

5. Conclusions

Based on the research carried out, the following summary notes are formed. Models for different degrees of loading have been created. It should be noted that the experimental results are of great value, since as a result of their analysis it can be established how correctly the electric motor is designed, to clarify the reserves for improvement and possible shortcomings. This is actually planned as future work - testing with different loads on the shaft of the motor under consideration.

The selection of an electric drive should not end with considering only the possibility of obtaining certain mechanical characteristics. It is also necessary to evaluate the dynamic qualities, economic indicators, reliability and ease of maintenance.

6. Acknowledgments

The implementation of this paper is thanks to the support from the Project BG16RFPR002-1.014-0005 Competence Center 'Intelligent Mechatronic, Eco- and Energy-Saving Systems and Technologies' financed by the Operational Program 'Science and Education for Intelligent Growth' of the European Regional Development Fund.

9. References

1. https://www.tllmedia.bg/
2. https://caproni.bg/
3. A. Hughes, B. Drury, Electric Motors and Drives. Fundamentals, Types, and Applications. Fourth Edition, Elsevier (2013) pp. 349-351. ISBN: 978-0-08-098332-5
4. https://iec.ch/
5. www.raider.bg
6. https://www.ansys.com/

On the Geometric Role of the Distribution Parameter in Conic Spatial Rack Drives

Emilia Abadjieva
Institute of Mechanics - Bulgarian Academy of Science, Sofia, Bulgaria
abadjieva@gmail.com

Abstract: *This paper presents a study of some geometric characteristics of conic spatial rack drives with linear helicoids. Three variants of the conic configuration are considered — with convolute, involute, and Archimedean helicoids — and their action surface properties are analyzed in relation to the distribution parameter. The role of the distribution parameter in determining the geometry of the action surface and the position of each variant in the design parameter space is discussed.*

Keywords*: RACK DRIVES, SLIDING VELOCITY, ANALYTICAL CONDITIONS, DISTRIBUTION PARAMETER*

1. Introduction

The transformation of rotational motion into rectilinear translation, and vice versa, represents a fundamental kinematic function in a wide range of mechanical systems — from industrial machinery and robotics to precision actuators and mechatronic devices. Spatial rack mechanisms occupy a special place among such devices: unlike conventional plane rack-and-pinion systems, they operate with non-orthogonal axis configurations, introduces additional geometric freedom in the design process. This freedom enables more compact drive layouts, customized force transmission paths, and better adaptation to the spatial constraints typical of modern robotic and mechatronic applications [1 -4].

The theoretical foundations for spatial gear mechanisms are established by Olivier [5] through formulation of generation principles, and later they are systematized by Litvin and Fuentes [6]. The geometry of helical surfaces and hyperboloid gear mechanisms has been studied extensively by Litvin [6], Minkov [4], and Abadjiev [2], providing the theoretical foundation for spatial rack drive analysis. Early studies on spatial conic rack configurations are presented by Trahanov and Ilinski [8], who treat a specialized conic rack enabling variable velocity ratio transformation, and by Watanabe and Maki [9], who analyze a Wildhaber-Novikov rack mechanism from a contact stress perspective. Systematic geometric synthesis methodologies for spatial rack drives with linear helicoids are developed in [1, 2, 7], establishing action surface equations and mesh region characterization for conic, cylindrical, and face configurations.

The present paper examines the role of the distribution parameter in the classification of conic linear helicoid variants and shows its connection to the geometry of the action surface and the position of each variant in the geometric parameter space.

2. Kinematic Scheme and Sliding Velocity Vector

2.1 Kinematic Configuration

The spatial rack mechanism is considered as a three-link system in which link $i=1$ rotates with angular velocity ω_1 (value of the angular velocity vector $\overline{\omega}_1$) around a fixed axis $1-1$, while link $i=2$ performs rectilinear translation with velocity (value of the translation velocity vector $\overline{V}_2$) (see Fig. 1).

The motions transformation of type ($R \leftrightarrow T$) and vice versa is realized through high kinematic joints ($\Sigma_1 : \Sigma_2$) which elements Σ_1 and Σ_2 at any moment have a conjugate instantaneous contact points P (the points of tangential contact P can belong to the conjugate instantaneous contact line). The motions transformation is characterized by the following conditions [1]:

$$\omega_1 = constant,\ V_2 = constant,$$
$$\delta_r = \angle(\overline{\omega}_1, \overline{V}_2) = \pi - \Sigma_r = constant, \qquad (1)$$
$$j_{12} = \frac{\omega_1}{V_2} = \frac{1}{j_{21}} = constant,$$

where with δ_r it is a crossed angle between the motion transformation vectors and with Σ_r it is noted an angle between the motion directions of the rack drive; j_{12}, j_{21} - velocity ratio of motion transformation of type $R \leftrightarrow T$.

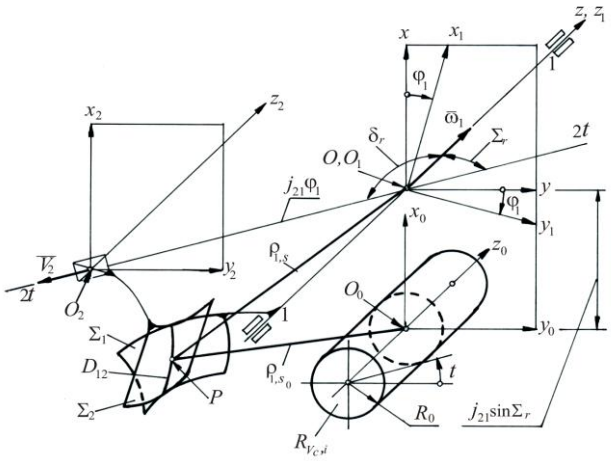


Fig 1. Kinematic configuration of spatial rack mechanism, where $S(O,x,y,z)$ is fixed coordinate system; the coordinate system $S_1(O_1,x_1,y_1,z_1)$ and $S_2(O_2,x_2,y_2,z_2)$ are connected to the movable links $i=1$ and $i=2$ correspondingly

For the rack mechanism in every moment of motion transformation, more than one high kinematic joints ($\Sigma_1 : \Sigma_2$) takes part in the process of transformation. When rotation with angular velocity $\overline{\omega}_1$ is applied to the link $i=1$, the second motion link $i=2$ obtains a translation velocity $\overline{V}_2$. According to (1) the condition $V_2 = j_{21}\omega_1$ is accomplished for the value of $\overline{V}_2$. Hence, the joints ($\Sigma_1 : \Sigma_2$) shown in Fig. 1 are kinematicaly conjugated, and the rack mechanism, respectively.

From the kinematic configuration shown in Fig. 1, link $i=1$ obtains rotational velocity at any contact point P, while link $i=2$ realizes translational velocity as defined in (1). The sliding velocity at P is the difference between the two velocity components [1]:

$$\overline{V}_{12} = \overline{V}_1 - \overline{V}_2 = \overline{V}_{r,2} - \overline{V}_{r,1}. \qquad (2)$$

where $\overline{V}_{12}$ is relative (sliding) velocity vector of the contact point P; $\overline{V}_i$ - transference velocity vector of P, joined to surface Σ_i; $\overline{V}_{r,i}$ - relative velocity vector of point P, when P moves on the surface Σ_i. For the kinematic conjugation of the high kinematic joints ($\Sigma_1 : \Sigma_2$), the sliding velocities displacement $\overline{V}_{12}$ at the common contact points P of the geometrical elements Σ_1 and Σ_2 is of a great importance.

2.2 Sliding Velocity Vector and Scalar Field Analysis

According to the condition of transformation (1) and the kinematic configuration shown in Fig. 1, for the function (2), written in the coordinate system $S(O,x,y,z)$, it is obtained [1]:

$$\overline{V}_{12} = \overline{V}_{12}(x,y,z) = \overline{V}_1 - \overline{V}_2 = \overline{\omega}_1 \times \overline{\rho}_{1,s} - \overline{V}_2. \quad (3)$$

By taking into account (1) and (3) in the fixed coordinate system $S(O,x,y,z)$ and symbols shown in Fig. 1[1] it is obtained:

$$\begin{aligned} &\overline{V}_{12} = \overline{V}_{12}(x,y,z) = V_{12,x}\overline{i} + V_{12,y}\overline{j} + V_{12,z}\overline{k}, \\ &V_{12,x} = -y,\ V_{12,y} = x + j_{21}sin\Sigma_r,\ V_{12,z} = j_{21}cos\Sigma_r, \end{aligned} \quad (4)$$

where coordinates of $\overline{V}_{12}$ in the coordinate system S are $V_{12,x}$, $V_{12,y}$, $V_{12,z}$ and $\overline{i}$, $\overline{j}$, $\overline{k}$ are unit vectors of the axes of the coordinate system $S(O,x,y,z)$.

In equation (4) without disturbing the community of arguments is accepted $\omega_1 = 1$ rad/s and therefore $V_2 = j_{21}$ m/s. The scalar magnitude of the relative velocity vector $\overline{V}_{12}$ (4) of the conjugate tooth surfaces Σ_1 and Σ_2 in their common contact points P defines a scalar vector field [1]:

$$V_{12} = V_{12}(x,y,z) = \sqrt{V_{12,x}^2 + V_{12,y}^2 + V_{12,z}^2}, \quad (5)$$

The family of surfaces satisfying:

$$V_{12}(x,y,z) = V_c,\ V_c = constant, \quad (6)$$

constitutes the surfaces of level of the scalar field (5) they define it geometrically. Their canonical type is determined in the coordinate system $S_0(O_0,x_0,y_0,z_0)$. From (4), (5) and (6) it follows [1]:

$$\begin{aligned} &x_0^2 + y_0^2 = R_0^2,\ z_0 = H,\ H \in (-\infty,+\infty), \\ &x_0 = x + j_{21}\sin\Sigma_r,\ y_0 = y,\ z_0 = z, \\ &R_0 = \sqrt{V_c^2 - (j_{21}\cos\Sigma_r)^2}. \end{aligned} \quad (7)$$

Equation (7) shows that the surfaces of level represent a family of coaxial cylinders — named *kinematic cylinders of level* [1] — with family parameter V_c whose axis coincides with the axis O_0z_0 of the coordinate system $S_0(O_0,x_0,y_0,z_0)$. The surfaces of level will exist if:

$$V_c \geq j_{21}\cos\Sigma_r. \quad (8)$$

When equality holds in (8), the cylinder transforms into the axis O_0z_0 — the zero kinematic cylinder of level — which is the locus of points of minimum sliding velocity.

Substituting the transformation (7) into the components of (4), the sliding velocity vector in $S_0(O_0,x_0,y_0,z_0)$ takes the form:

$$V_{12,x_0} = -y_0,\ V_{12,y_0} = x_0,\ V_{12,z_0} = j_{21}\cos\Sigma_r. \quad (9)$$

From equation system (9) for the sliding velocity in $S_0(O_0,x_0,y_0,z_0)$ follows:

$$V_{12,s_0} = \sqrt{x_0^2 + y_0^2 + (j_{21}\cos\Sigma_r)^2}. \quad (10)$$

In every point of the axis O_0z_0, the sliding velocity vector $\overline{V}_{12}$ obtains its minimum value:

$$V_{12,\min} = V_{12,z_0} = p_{z_0} = j_{21}\cos\Sigma_r \quad (11)$$

3. Conic Linear Helicoids and Distribution Parameter

The kinematic analysis establishes the spatial distribution of the sliding velocity field and identifies the geometric locus corresponding to minimum relative sliding. However, the actual sliding conditions in a spatial rack mechanism additionally depend on the geometry of the contacting tooth surfaces. In conic rack drives, these active surfaces are generated as linear helicoids whose geometric structure determines both the orientation of the contact lines and consequently the geometry of the action surface within the kinematic field [1]. Therefore, the following analysis focuses on the geometric characteristics of conic linear helicoids and, in particular, on the role of the distribution parameter in relation to the sliding conditions established above.

3.1 Generation of Conic Helicoids and Active Tooth Surfaces- Parametric Representation

The helicoids and especially the linear helicoids are widely used as active tooth surfaces of spatial gears with crossed axes, in both working meshing conditions and instrumental meshing conditions. Such choice of the active tooth surfaces for these gears is determined by the technological manufacturing, especially when their synthesis is performed in accordance with the second Oliver's principle [3, 7].

Fig. 2 shows the generation of right-handed conic convolute helicoids $\Sigma_1^{(j)}$ $(j = 1,\ 2)$ determined by different geometrical characteristics of the helical teeth (treads) of the particular gear mechanism. The process of helical surfaces generation is considered in fixed coordinate system $S_p^{(j)}(O_p^{(j)},x_p^{(j)},y_p^{(j)},z_p^{(j)})$ and it is as follows. The generatrix $L^{(j)}$ does not cross the axis $O_p^{(j)}z_p^{(j)}$ which coincides with the geometric axis of the gear. $L^{(j)}$ and $O_p^{(j)}z_p^{(j)}$ conclude an angle $0{,}5\pi < \xi^{(j)} < \pi$. The line $L^{(j)}$ belongs to plane $T^{(j)}$, which is tangential to the directed circled cylinder $C^{(j)}$. The generation of the $\Sigma_1^{(j)}$ by the line $L^{(j)}$ is realized by two generatrix motions: axial helical motion along the longitudinal axis $O_p^{(j)}z_p^{(j)}$ with parameter $p_s^{(j)} = const.$; crossed helical motion in the plane $T^{(j)}$, perpendicular to the axis $O_p^{(j)}z_p^{(j)}$ with parameter $p_t^{(j)} = const.$ Here it should be noted that $\Sigma_1^{(1)}$ is the conic convolute helical surface that is turned to the positive direction of the axis $O_p^{(j)}z_p^{(j)}$, and $\Sigma_1^{(2)}$ is the helicoid, turned along the negative direction of the $O_p^{(2)}z_p^{(2)}$.

The vector equation of the conic convolute helical surface $\Sigma_1^{(1)}$, in accordance with Fig. 2, has the form [1]:

$$\overline{\rho}_1^{(j)} = \overline{r}_0^{(j)} + \overline{s}^{(j)} + \overline{t}^{(j)} + \overline{u}^{(j)}, \quad (12)$$

where $\overline{\rho}_1^{(j)}$ is a radius-vector of point $N^{(j)}$ that belongs to the conic convolute helicoid $\Sigma_1^{(j)}$; $\overline{r}_0^{(j)}$ - radius-vector of the directed cylinder $C^{(j)}$; $\vartheta^{(j)}$, $u^{(j)}$ - coordinates of the helical surface $\Sigma_1^{(j)}$; $s^{(j)} = p_s^{(j)}\vartheta^{(j)}$ - axial motion of the generatrix $L^{(j)}$; $t^{(j)} = p_t^{(j)}\vartheta^{(j)}$ - crossed displacement (tangential to the directed cylinder $C^{(j)}$) of the generatrix line $L^{(j)}$.

If (12) is written in coordinate system $S_p^{(j)}$, then:

$$\begin{aligned} &x_p^{(j)} = r_0^{(j)}cos\vartheta^{(j)} \pm (u^{(j)}sin\xi^{(j)} - p_t^{(j)}\vartheta^{(j)})sin\vartheta^{(j)}, \\ &y_p^{(j)} = r_0^{(j)}sin\vartheta^{(j)} \mp (u^{(j)}sin\xi^{(j)} - p_t^{(j)}\vartheta^{(j)})cos\vartheta^{(j)}, \\ &z_p^{(j)} = p_s^{(j)}\vartheta^{(j)} \pm u^{(j)}cos\xi^{(j)}; \end{aligned} \quad (13)$$

For the equation systems (13) the upper signs and $j = 1$ refer to the $\Sigma_1^{(1)}$, and the lower and $j = 2$ refer to the $\Sigma_1^{(2)}$.

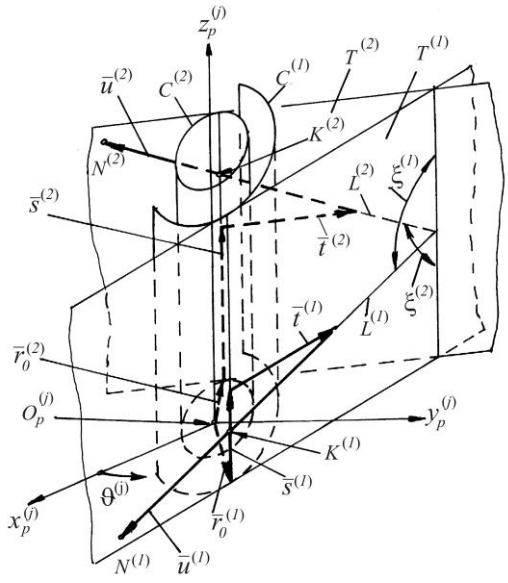


Fig. 2. Conic convolute helicoids generation

After a substitution in (13)

$$R_0^{(j)} = u^{(j)} - \frac{p_t^{(j)}\vartheta^{(j)}}{sin\xi^{(j)}} \text{ and } p^{(j)} = p_s^{(j)} \pm p_t^{(j)}cot\xi^{(j)}, \quad (14)$$

it is obtained

$$\begin{aligned} x_p^{(j)} &= r_0^{(j)}cos\vartheta^{(j)} \pm R_0^{(j)}sin\xi^{(j)}sin\vartheta^{(j)}, \\ y_p^{(j)} &= r_0^{(j)}sin\vartheta^{(j)} \mp R_0^{(j)}sin\xi^{(j)}cos\vartheta^{(j)}, \\ z_p^{(j)} &= p^{(j)}\vartheta^{(j)} \pm R_0^{(j)}cos\xi^{(j)}; \end{aligned} \quad (15)$$

Equations (15) represents the conic convolute helical surface $\Sigma_1^{(j)}$ as a cylindrical one with helical parameter $p^{(j)} = const$ and coordinates $\vartheta^{(j)}$ and $R_0^{(j)}$.

Conic involute helical surfaces generation. It is known [10] that each developable surface is cylindrical one, conic one or locus of the tangential lines to an arbitrary curve and vice versa - each cylindrical, conic or surface representing the locus of tangential lines to a curve is a developable surface.

The specific for each developable surface is, that the parameter of distribution is equal to zero, i.e.

$$h^{(j)} = p^{(j)} + r_0^{(j)}cot\xi^{(j)} = 0, \quad \text{or} \quad \cot\xi^{(j)} = -\frac{p^{(j)}}{r_0^{(j)}}. \quad (16)$$

Following the condition (16), the equation (15) describes the conic involute helicoid as:

$$\begin{aligned} x_p^{(j)} &= r_0^{(j)}cos\vartheta^{(j)} \pm R_0^{(j)}cos\lambda_0^{(j)}sin\vartheta^{(j)}, \\ y_p^{(j)} &= r_0^{(j)}sin\vartheta^{(j)} \mp R_0^{(j)}cos\lambda_0^{(j)}cos\vartheta^{(j)}, \\ z_p^{(j)} &= p^{(j)}\vartheta^{(j)} \mp R_0^{(j)}sin\lambda_0^{(j)}, \end{aligned} \quad (17)$$

where $R_0^{(j)} = u^{(j)} - \frac{p_t^{(j)}\vartheta^{(j)}}{cos\lambda_0^{(j)}}$, $p^{(j)} = p_s^{(j)} \mp p_t^{(j)}tan\lambda_0^{(j)}$ and $\lambda_0^{(j)} = \xi^{(j)} - \pi/2$ is spiral angle [11] for the directed helical line on the cylinder $C^{(j)}$. For this case the cylinder $C^{(j)}$ is named basic cylinder.

Conic Archimedean helical surfaces generation. The conic Archimedean helicoid is generated when the generatrix $L^{(j)}$ (see Fig. 2) crosses the axis $O_p^{(j)}z_p^{(j)}$, i.e. when $r_0^{(j)} = 0$.

Then from (13) it is obtained:

$$\begin{aligned} x_p^{(j)} &= \pm(u^{(j)}sin\xi^{(j)} - p_t^{(j)}\vartheta^{(j)})sin\vartheta^{(j)}, \\ y_p^{(j)} &= \mp(u^{(j)}sin\xi^{(j)} - p_t^{(j)}\vartheta^{(j)})cos\vartheta^{(j)}, \\ z_p^{(j)} &= p_s^{(j)}\vartheta^{(j)} \pm u^{(j)}cos\xi^{(j)}. \end{aligned} \quad (18)$$

The curvilinear coordinate $\vartheta^{(j)}$ in (18) represents the angle on which the normal vector $\bar{r}_0^{(j)}$ rotates to the axial plane (determined by the $L^{(j)}$ and $O_p^{(j)}z_p^{(j)}$). If it is noted with $\vartheta_a^{(j)} = \vartheta^{(j)} + \pi/2$, the angle, that the plane ($L^{(j)}, O_p^{(j)}z_p^{(j)}$) concludes with the plane ($O_p^{(j)}x_p^{(j)}z_p^{(j)}$), then the equation systems (18) turn into:

$$\begin{aligned} x_p^{(j)} &= \mp[u^{(j)}sin\xi^{(j)} - p_t^{(j)}(\vartheta_a^{(j)} - \pi/2)]cos\vartheta_a^{(j)}, \\ y_p^{(j)} &= \mp[u^{(j)}sin\xi^{(j)} - p_t^{(j)}(\vartheta_a^{(j)} - \pi/2)]sin\vartheta_a^{(j)}, \\ z_p^{(j)} &= p_s^{(j)}(\vartheta_a^{(j)} - \pi/2) \pm u^{(j)}cos\xi^{(j)}. \end{aligned} \quad (19)$$

4. Action Surface Geometry

The action surface, considered as a locus of the lines of the tooth contact in the fixed space, defines conjugate tooth surfaces of the second movable link – tooth rack.

The offered here study is realized with shown in Fig. 3 symbols.

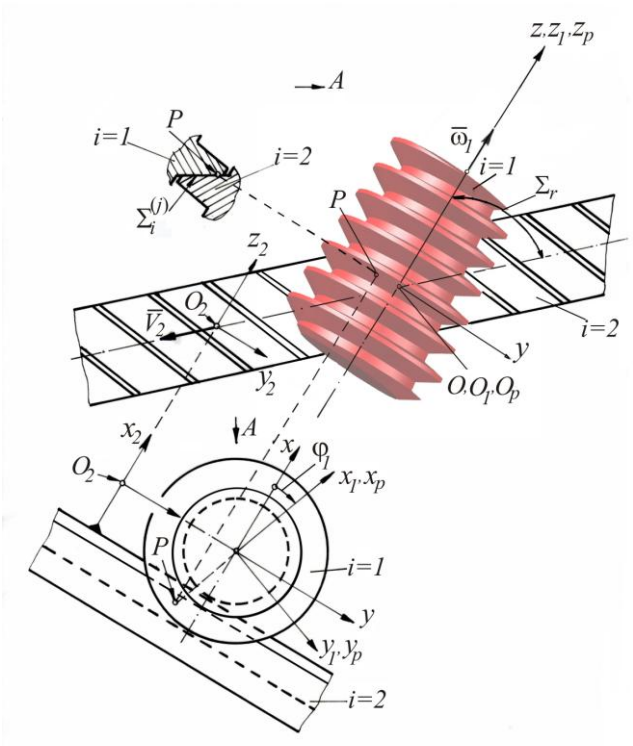


Fig. 3. Geometric-kinematic scheme of spatial rack drive having rotating linear conic helicoids

Conic convolute rack mechanism. The equations (15) of the linear helicoid $\Sigma_1^{(j)}$ are shown as:

$$\begin{aligned} x_p^{(j)} &= r_0^{(j)}cos\vartheta^{(j)} \pm U^{(j)}sin\vartheta^{(j)}, \\ y_p^{(j)} &= r_0^{(j)}sin\vartheta^{(j)} \mp U^{(j)}cos\vartheta^{(j)}, \\ z_p^{(j)} &= p^{(j)}\vartheta^{(j)} \pm U^{(j)}cot\xi^{(j)}, \end{aligned} \quad (20)$$

where $U^{(j)} = R_0^{(j)}sin\xi^{(j)} = u^{(j)}sin\xi^{(j)} - p_t^{(j)}\vartheta^{(j)}$, $p^{(j)} = p_s^{(j)} \pm p_t^{(j)}cot\xi^{(j)}$.

The set of equations (20) describes the conic convolute helicoid as a cylindrical one with helical parameter $p^{(j)}$.

The normal vector in an arbitrary point of $\Sigma_1^{(j)}$ is described by equations system:

$$\begin{aligned} n_{1,x_p}^{(j)} &= \mp h^{(j)} sin\xi^{(j)} cos\vartheta^{(j)} - U^{(j)} cos\xi^{(j)} sin\vartheta^{(j)}, \\ n_{1,y_p}^{(j)} &= \mp h^{(j)} sin\xi^{(j)} sin\vartheta^{(j)} + U^{(j)} cos\xi^{(j)} cos\vartheta^{(j)}, \\ n_{1,z_p}^{(j)} &= U^{(j)} sin\xi^{(j)}. \end{aligned} \quad (21)$$

It is known [1, 12] that conic helicoids $\Sigma^{(j)}$ are cylindrical helical surfaces with constant helical parameter $p^{(j)} = const.$

Hence, for these surfaces is valid the equation of meshing [1, 12]:

$$\tan\Delta = \frac{n_{1,y}}{n_{1,z}} = \frac{p + j_{21} cos\delta_r}{j_{21} sin\delta_r} = constant. \quad (22)$$

Then the action surface of the conic convolute helicoid is described by using the equations (20) and (21) (written in the fixed coordinate system S) and the analytical type (22) of meshing equation (see Fig. 4), i.e.

$$\begin{aligned} x^{(j)} &= r_0^{(j)} cos\theta^{(j)} \pm U^{(j)} sin\theta^{(j)}, \\ y^{(j)} &= r_0^{(j)} sin\theta^{(j)} \mp U^{(j)} cos\theta^{(j)}, \\ z^{(j)} &= p^{(j)} \vartheta^{(j)} \pm U^{(j)} cot\xi^{(j)}, \\ \frac{\mp h^{(j)} sin\xi^{(j)} \sin\theta^{(j)} + U^{(j)} cos\xi^{(j)} cos\theta^{(j)}}{U^{(j)} sin\xi^{(j)}} &= \frac{p^{(j)} - j_{21} cos\Sigma_r}{j_{21} sin\Sigma_r}, \end{aligned} \quad (23)$$

where $\theta^{(j)} = \vartheta^{(j)} + \varphi_1$, $U^{(j)} = u^{(j)} sin\xi^{(j)} - p_t^{(j)} \vartheta^{(j)} \neq 0$, $p^{(j)} = p_s^{(j)} \pm p_t^{(j)} cot\xi^{(j)}$, $h^{(j)} = p^{(j)} + r_0^{(j)} cot\xi^{(j)}$.

The tooth surfaces $\Sigma_2^{(j)}$ ($j = 1,\ 2$) of the tooth rack $i = 2$, conjugated with $\Sigma_1^{(j)}$, are obtained from (23), after it is written in the fixed coordinate system S_2, firmly connected with link $i = 2$:

$$\begin{aligned} x_2^{(j)} &= r_0^{(j)} cos\theta^{(j)} \pm U^{(j)} sin\theta^{(j)}, \\ y_2^{(j)} &= r_0^{(j)} sin\theta^{(j)} \mp U^{(j)} cos\theta^{(j)} + j_{21}\varphi_1 sin\Sigma_r, \\ z_2^{(j)} &= p^{(j)} \vartheta^{(j)} \pm U^{(j)} cot\xi^{(j)} + j_{21}\varphi_1 cos\Sigma_r, \\ \frac{\mp h^{(j)} sin\theta^{(j)} + U^{(j)} cot\xi^{(j)} cos\theta^{(j)}}{U^{(j)}} &= \frac{p^{(j)} - j_{21} cos\Sigma_r}{j_{21} sin\Sigma_r}. \end{aligned} \quad (24)$$

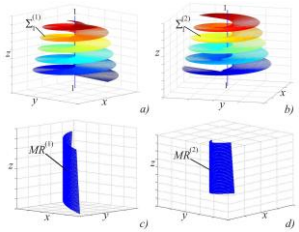


Fig. 4. *Spatial conic convolute mechanism with velocity ratio* $j_{21} = 2{,}29$*; number of the teeth* $z_1 = 1$*: a) conic convolute worm* $\Sigma_1^{(1)} \Rightarrow \xi^{(1)} = 98^\circ$, *b)* $\Sigma_1^{(2)} \Rightarrow \xi^{(2)} = 120^\circ$, *c) region of mesh* $MR^{(1)}$*; d)* $MR^{(2)}$

Conic Archimedean rack mechanism. The analytical representation of the action surface of the conic Archimedean rack drive (see Fig. 5) is obtained from the (23) after a substitution $r_0^{(j)} = 0$, whence $h^{(j)} = p^{(j)}$, i.e.

$$\begin{aligned} x^{(j)} &= \pm U^{(j)} sin\theta^{(j)}, \\ y^{(j)} &= \mp U^{(j)} cos\theta^{(j)}, \\ z^{(j)} &= p^{(j)} \vartheta^{(j)} \pm U^{(j)} cot\xi^{(j)}, \\ \frac{\pm p^{(j)} sin\theta^{(j)} + U^{(j)} cot\xi^{(j)} cos\theta^{(j)}}{U^{(j)}} &= \frac{p^{(j)} - j_{21} cos\Sigma_r}{j_{21} sin\Sigma_r}. \end{aligned} \quad (25)$$

Active tooth surfaces $\Sigma_2^{(j)}$ ($j = 1,\ 2$) of the tooth rack of the Archimedean rack drive are obtained from the system (25):

$$\begin{aligned} x_2^{(j)} &= \pm U^{(j)} sin\theta^{(j)}, \\ y_2^{(j)} &= \mp U^{(j)} cos\theta^{(j)} + j_{21}\varphi_1 sin\Sigma_r, \\ z_2^{(j)} &= p^{(j)} \vartheta^{(j)} \pm U^{(j)} cot\xi^{(j)} + j_{21}\varphi_1 cos\Sigma_r, \\ \frac{\mp p^{(j)} sin\theta^{(j)} + U^{(j)} cot\xi^{(j)} cos\theta^{(j)}}{U^{(j)}} &= \frac{p^{(j)} - j_{21} cos\Sigma_r}{j_{21} sin\Sigma_r}. \end{aligned} \quad (26)$$

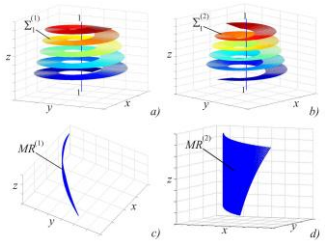


Fig. 5. Spatial conic Archimedean drive with velocity ratio $j_{21} = 2{,}29$; number of the teeth $z_1 = 1$: a) conic Archimedean right-handed worm $\Sigma_1^{(1)} \Rightarrow \xi^{(1)} = 98^\circ$; b) conic Archimedean right-handed worm $\Sigma_1^{(2)} \Rightarrow \xi^{(2)} = 120^\circ$, c) mesh region $MR^{(1)}$; d) mesh region $MR^{(2)}$

Conic involute rack mechanism. From equations systems (23) after substituting $h^{(j)} = 0$, it is obtained the analytical form of action surfaces (see Fig. 6):

$$\begin{aligned} x^{(j)} &= r_0^{(j)} cos\theta^{(j)} \pm U^{(j)} sin\theta^{(j)}, \\ y^{(j)} &= r_0^{(j)} sin\theta^{(j)} \mp U^{(j)} cos\theta^{(j)}, \\ z^{(j)} &= p^{(j)} \vartheta^{(j)} \pm U^{(j)} cot\xi^{(j)}, \\ cot\xi^{(j)} cos\theta^{(j)} &= \frac{p^{(j)} - j_{21} cos\Sigma_r}{j_{21} sin\Sigma_r}. \end{aligned} \quad (27)$$

Bellow (27) is written in the fixed coordinate system, connected with the link $i = 2$. Hence, the active tooth surfaces $\Sigma_2^{(j)}$ ($j = 1,\ 2$) of the spatial involute conic rack drive are:

$$\begin{aligned} x_2^{(j)} &= r_0^{(j)} cos\theta^{(j)} \pm U^{(j)} sin\theta^{(j)}, \\ y_2^{(j)} &= r_0^{(j)} sin\theta^{(j)} \mp U^{(j)} cos\theta^{(j)} + j_{21}\varphi_1 sin\Sigma_r, \\ z_2^{(j)} &= p^{(j)} \vartheta^{(j)} \pm U^{(j)} cot\xi^{(j)} + j_{21}\varphi_1 cos\Sigma_r, \\ cot\xi^{(j)} cos\theta^{(j)} &= \frac{p^{(j)} - j_{21} cos\Sigma_r}{j_{21} sin\Sigma_r}. \end{aligned} \quad (28)$$

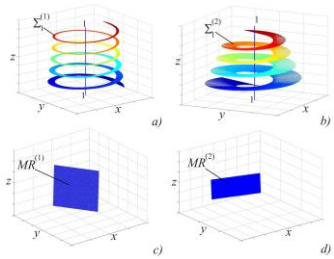


Fig. 6. Spatial conic involute mechanism with velocity ratio $j_{21} = 2{,}29$; number of the teeth $z_1 = 1$: a) conic involute right-handed worm $\Sigma_1^{(1)} \Rightarrow \xi^{(1)} = 98^\circ$,b) conic involute right-handed worm $\Sigma_1^{(2)} \Rightarrow \xi^{(2)} = 120^\circ$; c) mesh region $MR^{(1)}$; d) mesh region $MR^{(2)}$

5. Helicoid types and distribution parameter

The distribution parameter $h^{(j)}$ establishes a geometric relationship between the angle inclination $\xi^{(j)}$ and the directed cylinder radius $r_0^{(j)}$ which uniquely determines the types of conic helicoid. For conic helicoids, $h^{(j)}$ is defined as [1]:

$$h^{(j)} = p^{(j)} + r_0^{(j)} cot\xi^{(j)} \quad (29)$$

where $p^{(j)}$ is the helical parameter, $r_0^{(j)}$ is the radius of the cylinder radius, and $\xi^{(j)} \in (90^\circ, 180^\circ)$ is the angle between the generatrix $L^{(j)}$ and the longitudinal axis of the helicoid. When dimensionless geometric ratio $\rho = r_0^{(j)} / p_t^{(j)}$, is introduced, the three variants occupy distinct regions in the (ξ, ρ) parameter space:

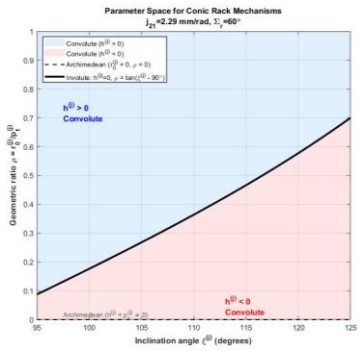


Fig. 7. Parameter space $(\xi^{(j)}, \rho)$ for conic rack drive ($j_{21} = 2{,}29$ mm/rad, $\Sigma_r = 60^\circ$). Black curve: involute curve $h^{(j)} = 0$, ; blue region: convolute $h^{(j)} > 0$; pink region: convolute $h^{(j)} < 0$; dashed line: Archimedean $\rho = 0$.

- *Conic involute helicoid* ($h^{(j)} = 0$): the condition $h^{(j)} = 0$ gives $r_0^{(j)} \cot\xi^{(j)} = -p^{(j)}$, which for the resultant helical parameter $p^{(j)} = p_s^{(j)} \pm p_t^{(j)} \cot\xi^{(j)}$ obtains the curve $\rho = \tan(\xi^{(j)} - 90^\circ)$. This is the black curve in Fig. 7. For this configuration the action surface is of plane type.

- *Conic convolute helicoid* ($h^{(j)} \neq 0$, $r_0^{(j)} > 0$): lies above $h^{(j)} > 0$) or below ($h^{(j)} < 0$) the involute curve. The action surface is convolute.

- *Conic Archimedean helicoid* ($r_0^{(j)} = 0$, $h^{(j)} = p_s^{(j)} \neq 0$): lies on the boundary $\rho = 0$, shown as the dashed line in Fig. 7. The action surface is Archimedean type.

The involute curve thus separates the parameter space into regions of positive and negative $h^{(j)}$. For a given inclination angle $\xi^{(j)}$, the type of conic helicoid is uniquely determined by the ratio ρ: a scientist or designer can take from Fig. 7 which configuration corresponds to their geometric parameters and what action surface geometry to expect. Thus, the distribution parameter connects the geometry of the active tooth surfaces to the sliding conditions of the mechanism — the type of action surface geometry, determined by $h^{(j)}$, defines the contact line orientation and consequently the conditions under which relative sliding between the tooth surfaces is realized.

6. Conclusion

The paper presents a study of the geometric characteristics of conic spatial rack drives with linear helicoids. The kinematic analysis establishes the sliding velocity field and its theoretical minimum, which depends only on the kinematic parameters of the mechanism. The three variants of conic linear helicoids — convolute, involute, and Archimedean — are characterized by the distribution parameter, which determines the geometry of their action surface. The design parameter space, defined by the inclination angle $\xi^{(j)}$ and the geometric ratio $\rho = r_0^{(j)} / p_t^{(j)}$, provides a unified geometric framework in which the position of each variant is uniquely determined by $h^{(j)}$. The involute configuration is located on a well-defined curve that separates the convolute regions, while the Archimedean configuration lies on the boundary $\rho = 0$. This classification allows a designer to identify directly, from the geometric parameters of the mechanism, which helicoid type is realized and what action surface geometry to expect — without additional computation.

6. References

1. Abadjieva, E., 2010. Mathematical Models of the Kinematic Processes in Spatial Rack Mechanisms and their Application. Ph.D. Thesis, Institute of Mechanics, Bulgarian Academy of Sciences, Sofia (in Bulgarian).
2. Abadjiev, V., 2007. Gearing Theory and Technical Applications of Hyperboloid Mechanisms. D.Sc. Thesis, Institute of Mechanics, Bulgarian Academy of Sciences, Sofia (in Bulgarian).
3. Abadjiev, V., Abadjieva, E., 2021. Conic linear helicoids: Part 2. Applications in the synthesis and design of spatial motions transformers. Mechanisms and Machine Science, Vol. 101, Springer, Cham, pp. 361–387.
4. Minkov, K., 1986. Mechanical and Mathematical Modeling of Hyperbolic Gears. Sc. D. Thesis, Sofia (in Bulgarian).
5. Olivier, T., 1842. Théorie Géométrique des Engrenages. Bachelier, Paris.
6. F. Litvin, 1994, Geometry and Applied Theory, PTR Prentice Hall, A Paramount Communication Company, Englewood Cliffs, New Jersey 07632, p. 724.
7. Abadjieva, E., Abadjiev, V., 2008. On the kinematic theory of spatial rack drives. Comptes Rendus de l'Académie Bulgare des Sciences, 61(12), 1525–1534.
8. Trahanov, K.T., Ilinski, V.N., 1973. Rack-conic drive with inconstant velocity ratio. In: Theory of Gears in Machines, Nauka, Moscow, pp. 49–56 (in Russian).
9. Watanabe, M., Maki, M., 2006. A study on new type WN rack and pinion. Proc. 2nd Int. Conf. Power Transmissions, Novi Sad, pp. 27–32.
10. Rashevsky, P. 1956, Course of Differential Geometry. Ed. State Publishing House of Technical and Theoretical Literature, Moscow 420 p.
11. BDS 8540-84, 1985. Gear sets. Common terms. Definitions and symbols. Institute of Standardization, Sofia.
12. Kovatchev, G., Abadjiev, V. 1990, On the Synthesis of Spatial Rack Mechanisms. Proc. 6-th National Congress of Theor. and Appl. Mech., Varna, 1, pp. 35-38, (in Russian).

A Study of Hybrid Adhesive-Mechanical Joints Between Metals and Composites Formed Using Thermal Drilling Technology

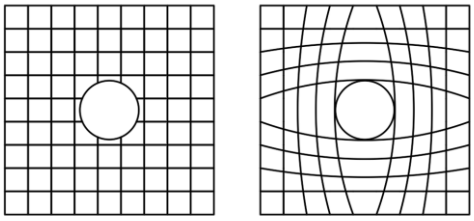
Anna Guzanová*, Dagmar Draganovská
Technical University of Košice, Faculty of Mechanical Engineering, Department of Technology, Materials and Computer Supported Production, Mäsiarska 74, Košice, Slovakia
anna.guzanova@tuke.sk

Abstract: *This article presents a study of the possibility of creating adhesive-mechanical bonds between aluminum and a thermoplastic matrix composite. In detail, the influence of drilling process parameters on the shape of the bushing and the formation of joints with fiber-reinforced composites during direct drilling using various tool speeds and feeds is examined. Finally, the load-bearing capacity of the formed joints is presented.*
Keywords*: COMPOSITE-METAL JOINING, THERMAL DRILLING, HYBRID ADHESION-MECHANICAL JOINT, LOAD-BEARING CAPACITY, ADHESION PROMOTER*

1. Introduction

In today's engineering industry, particularly in the automotive and aerospace sectors, there is a growing need to join dissimilar materials in order to reduce the weight of structures while maintaining their load-bearing capacity and safety. Joining thin-walled components made of aluminum alloys and composites is relatively complex because these materials have different physical and mechanical properties. It is precisely the complexity of joining these materials that requires the use of advanced technologies that employ multiple joining principles simultaneously, such as the application of pressure, heat, and mechanical interlocking of materials [1-3]. In the joining of thin-walled materials, the geometry of the mechanical joint plays a particularly important role, as it significantly influences its load-bearing capacity [4-7]. By appropriately modifying the shape and dimensions of the joint, it is possible to increase its load-bearing capacity without the need to add additional fasteners, which also helps maintain low weight and reduce manufacturing costs.

The aim of the experimental work was to investigate the possibilities of creating hybrid adhesive-mechanical joints between fiber-reinforced composites with a thermoplastic matrix and glass and carbon reinforcement and aluminum alloy sheets using thermal drilling technology without the use of fasteners. The adhesive joint is formed by pressing the heated composite with the thermoplastic matrix and the sheet metal across the entire overlap area. At the same time, the joint is secured by a metal bushing, which is created by drilling through the overlapped pair with a thermal drill bit, such that, thanks to the heated thermoplastic matrix, the reinforcing fibers in the vicinity of the forming bushing deflect without breaking. This prevents any weakening of the composite part's load-bearing capacity at the joint, Fig. 1.



a) fiber breakage (conventional drilling), b) fiber deflection (friction drilling)
Fig.1 *The effect of hole-making technology on the failure of composite fiber reinforcement*

To improve adhesion between the composite and the aluminum sheet, an organosilicate agent with organomodified silica nanoparticles was used in the study; this agent is applied to the steel surface using the sol-gel method, where it forms a colorless, transparent gel layer. After dehydration, a three-dimensional network of silicate compounds linked by siloxane bonds is formed. The organosilicate molecule has three key parts:

- a molecular core of aryl or alkyl origin ((CH_2)n, where n = 0, 1, or 3)
- a molecular end group containing an organic functional group (amino, vinyl, alkyl, etc.) that enables bonding to a specific organic monomer or polymer molecule via functional group interaction
- the other end of the molecule consists of an alkoxysilane group (Si(OR)n), where n = 3, which can bond to inorganic materials (metals, minerals, etc.).

By applying this preparation, we expect the formation of a strong bond between the metal substrate and the thermoplastic composite matrix via chemical bonds, which could result in increased adhesion of the joint.

2. Materials and Methods

EN AW-6082 T6 (AlSi1MgMn) aluminum alloy, a precipitation-hardened silumin, was used to form the joints in the form of 2 mm thick sheet metal.
Two types of composites were used: TEPEX Dynalite 102-RG600(3)/47% and Tepex® Dynalite 202-C 200(7)/52%, both with a thickness of 1.55 mm. The matrix is PA6 thermoplastic with a melting point of 220°C; the bidirectional reinforcement is carbon or glass roving fabric (Twill 2/2), Tab. 1.

Tab. 1 *Mechanical properties of materials used*

Mechanical properties	EN AW-6082 T6	PA6-GF	PA6-CF
Re [MPa]	299	-	-
Rm [MPa]	345	340	487
A_{80} [%]	16	1.8	0.87

A Flowdrill Long tool with a diameter of 5.3 mm was used for thermal drilling. The shape and dimensions of the test specimens were derived from the tool diameter in accordance with STN EN ISO 12996 and are shown in Fig. 2.

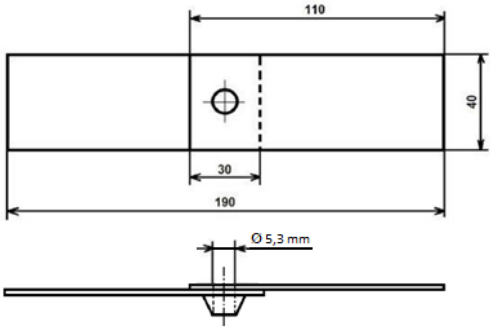


Fig. 2 *Shape and dimensions of test specimens and the sigle-lap joint for the Flowdrill Long tool, Ø 5.3 mm*

The surface of the aluminum sheet was degreased with an alkaline degreaser, followed by rinsing, immersion in a solution of an organosilicate compound in demineralized water, and then air-dried.

The materials to be joined were placed in a clamping fixture, where the composite was also heated; after reaching the melting temperature of the PA6 matrix (>220°C, approx. 240°C), friction drilling was performed to join the two materials. The joint was then rotated, and a flange was created using the same tool to close the joint, Fig. 3. During thermal drilling, the effect of tool speed and feed rate on the formation of the bushing was also tested separately in aluminum sheet metal, as well as in interaction with the composite. The tested tool speeds were 2400 and 4800 min^{-1}, and the feed was manual, slow (S, approx. 60 mm·min^{-1}) and fast (F, approx. 240 mm·min^{-1}).

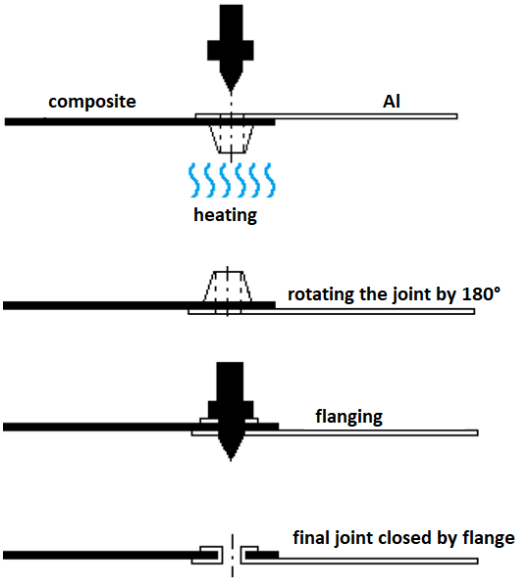


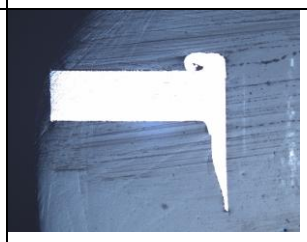
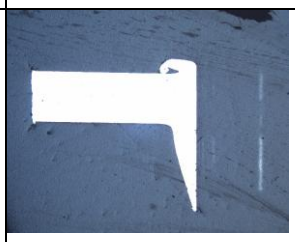
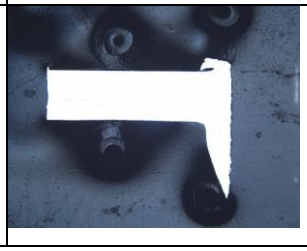
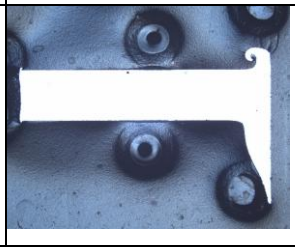
Fig. 3 *Procedure for creating joints*

The joints were then tested for load-bearing capacity using a tensile-shear test with a loading rate of 10 mm·min^{-1} in accordance with STN EN ISO 12996.

3. Results

Metallographic sections through the bushing, created by thermal drilling of an aluminum sheet at two tool speeds and feed rates, are shown in Tab. 2.

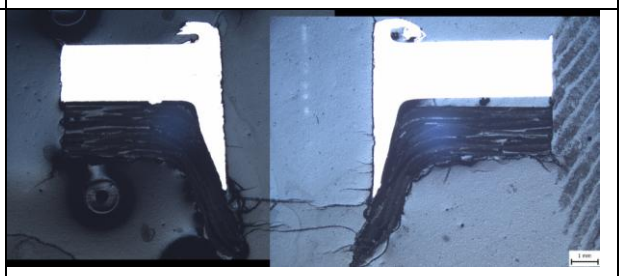
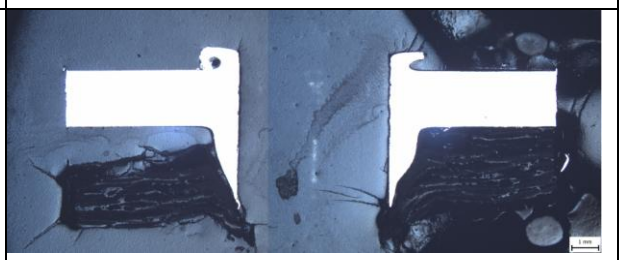
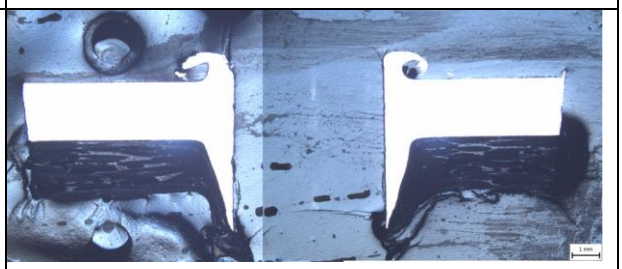
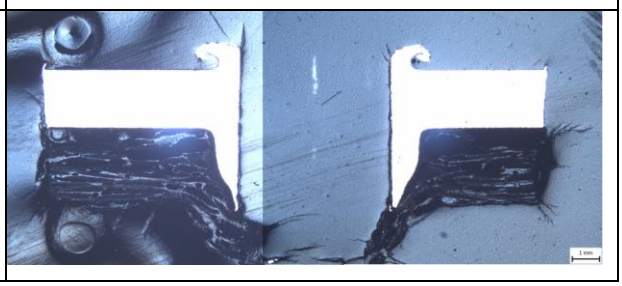
Tab. 2 *Metallographic sections through the bushing created under various process parameters*

	2400	4800
S		
F		

Tab. 2 shows the effect of process parameters on the shape of the bushing. The ideal bushing should be long enough to pass through a composite plate with a thickness of 1.55 mm and should have a shape that tapers smoothly. The greatest thickness of the bushing is just below the level of the sheet metal. It is precisely this area that should ensure sufficient joint strength and should be the point of failure of the bushing under tensile shear test.

Subsequently, direct joints were created under the given process parameters. Their cross-sections are shown in Tab. 3.

Tab. 3 *Metallographic cross-sections of Al-PA6CF joints created under various process parameters by direct drilling*

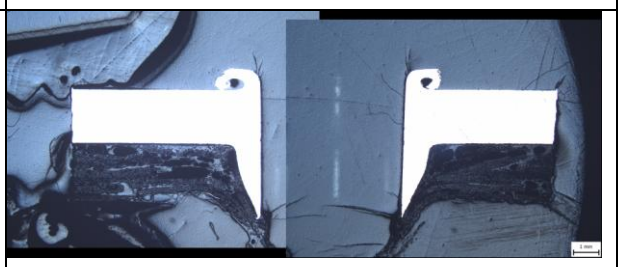
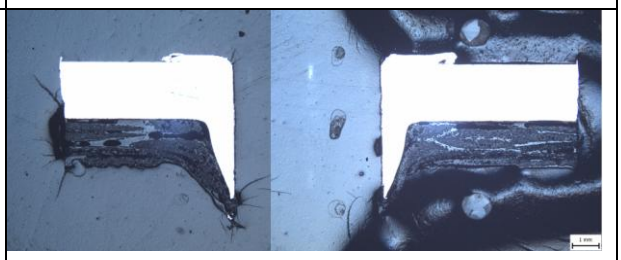
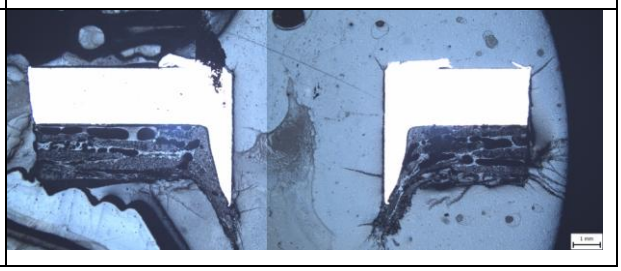
	Al-PA6CF
2400 S	
2400 F	
4800 S	
4800 F	

Tab. 3 shows changes in the shape of the bushing under various process parameters. The most suitable shape is observed at 2400S and 4800S. A slower feed rate creates better conditions for forming a bushing with the desired shape. From previous research, we know that for non-ferrous metals, it is more appropriate to select higher speeds, which is also recommended by the manufacturer of thermal drilling tools. Delamination of the composite around the bushing is also visible, which may be related to insufficient heating. However, this problem is mitigated by flanging the joints. The same cuts were made for Al-PA6GF joints, Tab. 4.

When drilling aluminum sheet on a composite panel, the influence of process parameters is less noticeable because the glass-fiber composite consists of only three layers of prepregs (unlike CF, which has seven layers for the same thickness), the fibers are thicker, the mat strands are more robust, and the fibers as a whole offer less resistance to tool penetration during thermal drilling. For

the subsequent creation of joints intended for load-bearing capacity testing, a tool speed of 4800 rpm and a slow feed rate (approx. 60 mm/min) were used.

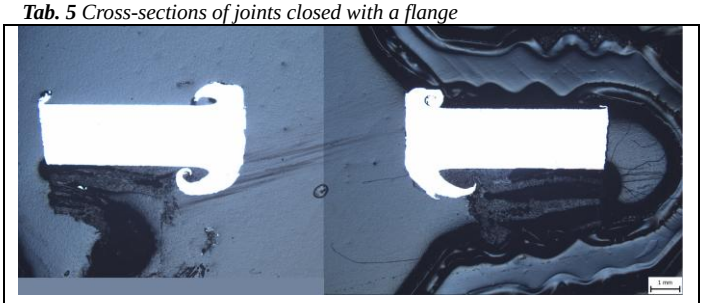
Tab. 4 *Metallographic cross-sections of Al-PA6GF joints created under various process parameters by direct drilling*

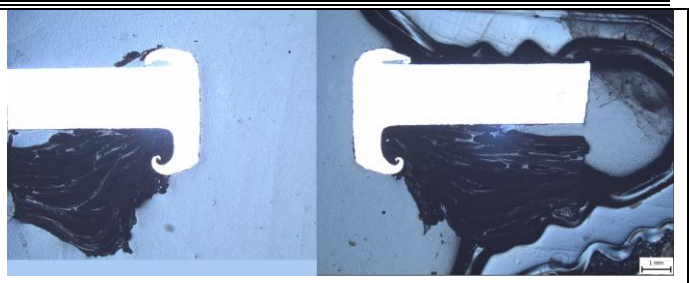
	Al-PA6GF
2400 S	
2400 F	
4800 S	
4800 F	

Cross-sections of joints created under these process parameters and closed with a flange are shown in Tab. 5.

Tab. 5 (Al-PA6GF) also shows potential defects resulting from manual feeding, namely excessive flattening of the bushing during flanging. CNC control of the process is, of course, possible, but it is very difficult to integrate the heating unit into a CNC-controlled process.

Tab. 5 *Cross-sections of joints closed with a flange*


Al-PA6GF


Al-PA6CF

A properly executed flange closes the layers of composite fibers and prevents their delamination, Fig. 4.

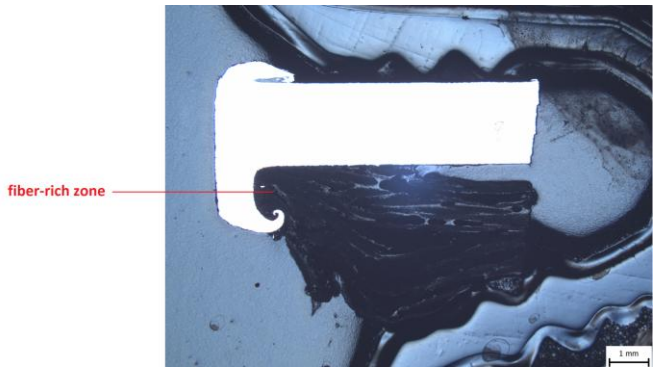
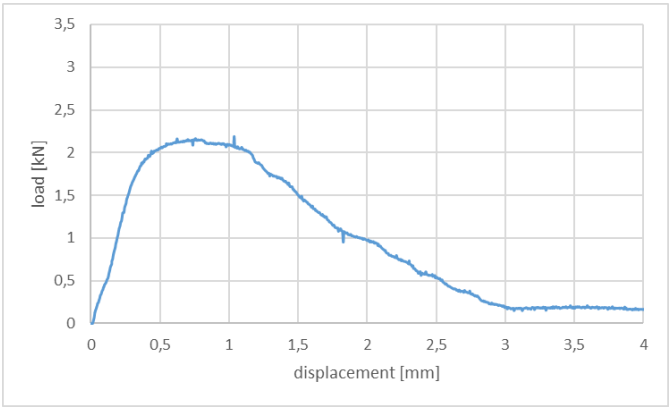


Fig. 4 *Proper hem finishing*

Figures 5 and 6 show the load-displacement curves obtained during joint load-bearing capacity testing, as well as the failure patterns.



a) load-displacement curve of Al-PA6CF joint



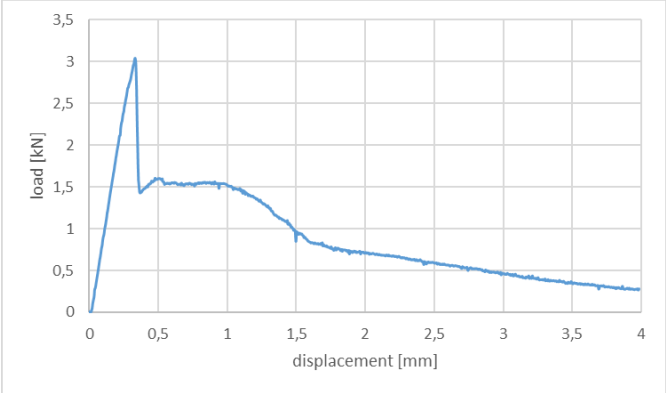
b) failure mode of Al-PA6CF joint

Fig. 5 *Load-bearing capacity testing and failure mode of the Al-PA6CF joint*

Fig. 5 clearly shows that the tensile loading of the Al-PA6CF joint exhibits a behavior typical of the progressive shear failure of the bushing. The maximum load-bearing capacity of the joint,

which consists solely of mechanical interlocking, is 2.1 kN. Failure occurs over a distance of approximately 2 mm, which would ideally correspond to the gradual shearing of the bushing—an aluminum alloy ring. However, observation of the joint failure surface shows that the bushing was only deformed when the joint was stressed; no shearing occurred. The composite slid along the outer conical surface of the bushing, causing it to move away from the sheet metal and finally pull out.

The loading history of the AlOS-PA6GF joint, Fig. 6, is different; it exhibits the characteristics of a hybrid adhesive-mechanical joint.



a) load-displacement curve of AlOS-PA6GF joint



b) failure mode of AlOS-PA6GF joint

Fig. 6 *Load-bearing capacity testing and failure mode of the Al-PA6GF joint*

The load-displacement curve shows two distinct regions: first, a peak is observed, corresponding to the transfer of forces through the adhesive bond between the two materials via the PA6 thermoplastic matrix across the entire overlap area. The adhesive bond fails at a load of 3 kN, and subsequently, the connection between the two materials is maintained only by the bushing, which gradually deforms, just as was described for the Al-PA6CF joint.

The measured data indicate that the organosilicate layer has a positive effect on the adhesive bond between the materials; however, there must be sufficient polymer matrix on the composite side, which, after melting, would contribute to the formation of the adhesive bond. According to the results, the glass fiber composite has more matrix available than the carbon fiber composite. Therefore, a hybrid bond does not form in the carbon fibre composite.

However, deformation of the bushing is not an ideal mode of joint failure; it does not guarantee that the mechanical properties of the Al sheet are fully utilized. Maximum utilization would occur if the failure took place immediately below the level of the sheet, at the point where the bushing is thickest, where there is the most material ensuring load-bearing capacity. To achieve this, it is necessary to eliminate the tangential component of the force during loading, which causes the composite to slip out of the bushing. We will address this issue in future research.

Conclusion

Based on the experimental results, it can be concluded that thermal drilling technology is an effective method for creating hybrid adhesive-mechanical bonds between aluminum alloys and thermoplastic composites without the need for additional fasteners. The study confirmed that the process parameters, specifically higher rotational speed (4800 min^{-1}) and slow feed rate (60 $mm.min^{-1}$), ensure optimal formation of the aluminum sleeve and flange, which seals the composite layers and prevents their delamination. The use of an organosilicate primer demonstrated a positive effect on adhesion, which was particularly evident in the glass-fiber composite (PA6-GF), where the joint achieved a load-bearing capacity of 3 kN due to a combination of adhesive and mechanical principles. In contrast, for carbon-fiber composites (PA6-CF), the load-bearing capacity was lower (2.1 kN), and the joint was purely mechanical in nature due to the lack of a polymer matrix to form an adhesive bond. The primary failure mechanism remains deformation and pull-out of the sleeve, which opens the door for further research aimed at optimizing the joint geometry and eliminating the forces causing the composite to slip.

Acknowledgement: *This work was supported by The Ministry of Education, Research, Development and Youth of the Slovak Republic under Grant VEGA 1/0229/23: Research on the applicability of thermal drilling technology for the creation of multi-material joints in the automotive industry.*

References

[1]. XIN, Z. – LIU, L. – CHEN, T. – WU, L. – CHEN, K. – KONG, L. – WANG, M.: Laser surface treatment to enhance the adhesive bonding between steel and CFRP: Effect of laser spot overlapping and pulse fluence. In: Optics & Laser Technology 22, 59 (2023), 1-12, 10.1016/j.optlastec.2022.109002.

[2]. LAMBIASE, F. – KO, D.: Two-steps clinching of aluminum and Carbon Fiber Reinforced Polymer sheets. In: Composite Structures 17, 164 (2017), 180-188, https://doi.org/10.1016/j.compstruct.2016.12.072.

[3]. GUZANOVÁ, A. – JANOŠKO, E. – VELIGOTSKYI, N.: Optimization of joining parameters of thin-walled materials by flowdrill technology. In: MACHINES. TECHNOLOGIES. MATERIALS 22, 5 (2022), 176-178, ISSN 1313-0226.

[4]. GUZANOVÁ, A. – JANOŠKO, E.: Application of flow-drill technology for joining metal materials. In: INNOVATIONS 21, 3 (2021), 108-111, ISSN 2603-3763.

[5]. SEIDLITZ, H. – ULKE-WINTER, L. – KROLL, L.: New Joining Technology for Optimized Metal/Composite Assemblies. In: Journal of Engineering 14, 1-11, http://dx.doi.org/10.1155/2014/958501.

[6]. TROSCHITZ, J. - FÜßEL, R. – KUPFER, R. – GUDE, M.: Damage Analysis of Thermoplastic Composites with Embedded Metal Inserts Using In Situ Computed Tomography. In: Journal of Composites Science 22, 6 (2022), 1-9, https://doi.org/10.3390/jcs6100287.

[7]. GROGER, B. et al.: Computed tomography inverstigation of the material structure in clinch joints in aluminium fibre-reinforced thermoplastic sheets. In: Production Engineering 22, 16 (2022), 203-212, https://doi.org/10.1007/s11740-021-01091-x.

Automatic quality control of blanked parts based on segmentation of shear and fracture zones using a convolutional neural network

Vyacheslav Tamila, Vladimir Klubovich, Yury Kastsiuchenka, Hanna Mantsivoda.
Belarusian National Technical University, Belarus
kastsiuchenka@bntu.by

Abstract: *A method for automatic quality control of blanked parts based on the ratio of the plastic deformation (shear) zone to the brittle fracture (rupture) zone on the cut surface is presented. Unlike known approaches that require strictly controlled shooting conditions, the proposed convolutional AI model (R-CNN) demonstrates robustness to a wide range of illumination: variations in brightness and light incidence angle reduce segmentation accuracy by no more than 3%. This is achieved through the use of local texture features that are invariant to brightness scale. The system takes into account the material grade — reference ratios of the zones are defined for each steel grade. Experiments were carried out on samples of three grades (AISI 1010, S235JR, AISI 1066). The classification accuracy of acceptable and defective parts was 98% relative to expert assessment.*
KEYWORDS*: SHEET METAL STAMPING, BLANKING, QUALITY CONTROL, CUT SURFACE, PLASTIC DEFORMATION ZONE, FRACTURE ZONE, BURR, MACHINE VISION, CONVOLUTIONAL NEURAL NETWORK*

1. Introduction

Sheet metal stamping occupies one of the leading positions among metal forming technologies due to its high productivity, low material consumption, and the ability to produce complex-shaped parts in a short time. The blanking operation is used to separate a sheet workpiece along a closed contour and is the basis for manufacturing many products — from car body elements to precision instrument components.

The quality of blanked parts is primarily determined by the condition of the cut surface. When stamping with clearances not exceeding 5–10% of the sheet thickness, characteristic zones are formed on the edge: the rollover (indentation zone), the smooth shiny zone of plastic shear, the rough zone of brittle fracture, and the burr on the lower face [1].

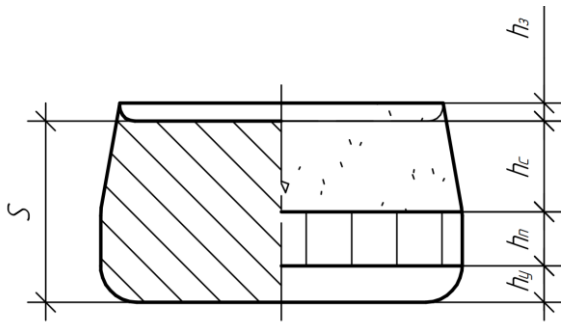


Fig. *1. Scheme of the separation zone on a blanked part*
S – thickness; h_y – rollover zone; h_n – plastic deformation zone; h_c – fracture zone; $h_з$ – burr.

The ratio between the plastic deformation zone and the fracture zone is a sensitive diagnostic parameter reflecting the clearance between punch and die, the degree of tool wear, and the plastic properties of the workpiece material. Therefore, quality control of blanked parts is a mandatory stage of the production process [2].

The first and most common method is visual and instrumental inspection. The inspector examines the edge of the part and measures the burr height with a feeler gauge or microscope. This method is simple and does not require expensive equipment, but it is subjective, labor-intensive, and practically unsuitable for 100% inspection on automatic lines with a cycle time of 1–2 seconds.

The second method is destructive testing involving the preparation of micro-sections. The sample is cut, ground, etched, and examined under a microscope. This allows accurate measurement of all cut zones, but the method is time-consuming, unsuitable for inspecting every part, and requires highly qualified personnel. Its domain is selective batch inspection or process qualification during die setup.

The third method is non-contact laser inspection. Laser triangulation sensors and optical profilometers allow constructing a 3D model of the edge with micron accuracy. Disadvantages include high cost, complex setup, and, most importantly, low productivity. Processing a single profile takes seconds, which becomes a "bottleneck" on an automatic line with a cycle time of 0.5–1 second.

The fourth method is machine vision systems with machine learning algorithms. A camera captures an image of the edge, and algorithms detect the presence of defects. This method is productive (up to 10–20 parts per second) and relatively cheap. However, existing implementations impose strict requirements on shooting conditions: illumination, part position, and orientation must be tightly controlled. In real production, this is difficult to achieve — lamps age, flare and shadows from neighboring equipment appear, and the part surface may be contaminated with lubricant. As a result, the high accuracy of algorithms achieved in the laboratory degrades on the production line.

Thus, modern methods for quality control of blanked parts are either insufficiently productive, or subjective, or too sensitive to external conditions. There is a need for a method that is simultaneously fast, objective, and robust to variations in shooting conditions [3].

In this work, propose an approach based on a convolutional artificial intelligence model for automatic segmentation of plastic deformation and fracture zones on the cut surface of parts obtained by sheet metal blanking operations. The key feature of the method is robustness to a wide range of illumination conditions, achieved by training the neural network on local texture features rather than on absolute brightness values. Additionally, the system takes into account the mechanical characteristics of the material, allowing different reference zone ratios to be used for ductile and brittle steels. The paper describes the experimental methodology, neural network architecture, obtained results, and their comparison with expert assessment.

2. Preparation of the experiment

2.1. Materials and Methods

For the experiment, a simple-action blanking die was designed and manufactured, allowing round blanks with a diameter of 30 mm to be cut from sheet metal with a thickness of 1.5 mm. The round shape was chosen due to the absence of corner stress concentration zones, which simplifies the analysis of the cut surface.

Sheets of three steel grades were used as the material: AISI 1010, S235JR, AISI 1066, which differ significantly in their shear strength (σ_s). This made it possible to evaluate the influence of the plastic properties of the material on the shear-to-fracture zone ratio.

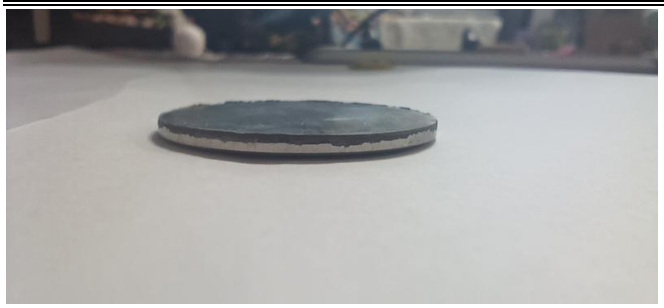


Fig. 2. *Blanked part*

2.2. Sample Formation

At the initial stage, the die was equipped with sharply sharpened punch and die with a radial clearance of 10% of the sheet thickness (0.15 mm). This clearance provides a high-quality cut with minimal burr and clear deformation and fracture zones. The obtained blanks were used as reference (acceptable) parts.

To artificially create defects, the punch was replaced with a tool of smaller diameter, which increased the clearance. The clearance was sequentially increased in steps of 1% of the sheet thickness. The maximum investigated clearance was 20% (0.30 mm), leading to a pronounced burr and predominance of the fracture zone over the shear zone. For each clearance value (from 10% to 20%), at least 20 blanks were manufactured.

3. Image Acquisition

The blanks were photographed using an ESP32-CAM board (OV2640 camera, 2 MP). The key condition was the simulation of real production conditions:

- Shooting was performed under various lighting conditions (daylight, overhead workshop lighting, local illumination, darkened conditions) — the "as is" principle, without professional light sources.
- The images were not subjected to any retouching, color correction, or sharpening.



Fig. 3. *Parts photographed at different angles*

Shooting was carried out at different angles with a deviation of −30° to +30° relative to the normal, simulating variations in part position. The total dataset size was 220 images. For each image, an expert performed manual annotation of the shear and fracture zones for training and validation of the neural network.

4. Neural Network Model Training

After image acquisition and dataset formation, data preparation for training was performed. Manual annotation of images was carried out using specialized software. At the first stage, the cut surface region was outlined — thus defining the region of interest (ROI), which allowed training the model to focus specifically on the edge of the part, ignoring the background and end surfaces.

At the second stage, within the selected cut zone, pixel-wise segmentation of two types of areas was performed: the plastic deformation zone (smooth shiny area) and the fracture zone (rough matte area).

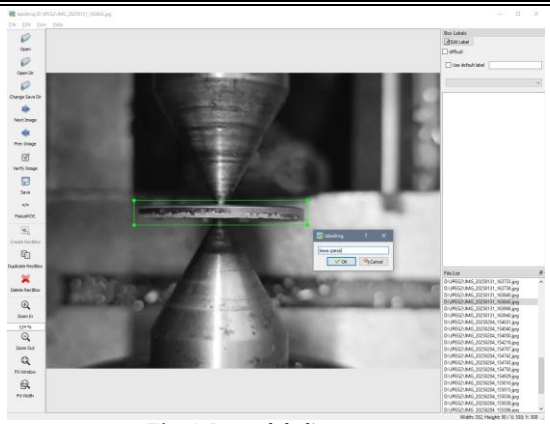


Fig. 4*. Image labeling process*

The annotated images formed the training dataset. The artificial intelligence model was implemented in Python using the TensorFlow framework. Training was conducted for 12 epochs. The final accuracy of the model on the validation set was 94.25%. The loss value during training decreased to 2.12%, indicating stable convergence and the absence of obvious overfitting.

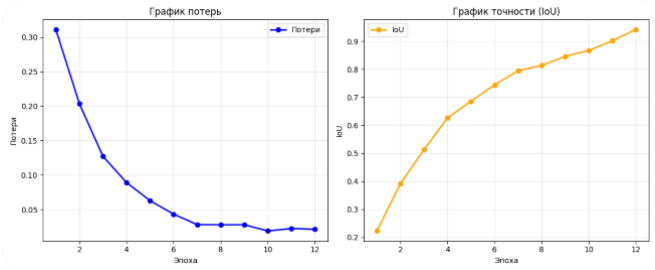


Fig. 5*. AI model accuracy metrics vs. training epochs*

Upon completion of training, the model is capable of automatically segmenting the shear and fracture zones on new images obtained under various lighting conditions without additional tuning.

5. Experimental Validation Results

At the final stage, the trained model was evaluated on a test set that was not used during training. The test set consisted of 100 images of cut surfaces obtained from different material grades (AISI 1010, S235JR, AISI 1066). Half of the images corresponded to blanks manufactured with increased clearance (11–20%), which exhibited pronounced burrs of various heights. The other half corresponded to reference blanks (clearance 10%) with a high-quality cut and no burr.



Fig. 6*. Example of model operation in cut zone detection*

The experiments confirmed that the trained model correctly recognizes the plastic deformation and fracture zones and also detects defects in the form of burrs. The decision on the presence of a defect was made automatically based on the deviation of the measured zone ratio from the reference value specified individually for each material grade.

On the test set, burr defects were detected in 98% of cases. This result confirms the high efficiency of the proposed approach and its suitability for automatic quality control of blanked parts under conditions close to real production.

6. References

1. Kastsiuchenka, Yu. A., & Tamila, V. A. (2024). *Investigation and optimization of surface separation quality indicators in sheet metal stamping operations*. In V. G. Zalessky (Ed.), Modern methods and technologies for creating and processing materials: collection of scientific papers. Book 2 (pp. 270–277). Minsk: FTI NAS of Belarus. (in Russian)

2. Tamila, V. A., Kastsiuchenka, Yu. A., Kulinich, I. L., et al. (2025). *Influence of technological clearance on the quality of separation surface during blanking and piercing, and burr minimization*. In V. K. Sheleg (Ed.), Mechanical Engineering: republican interdepartmental collection of scientific papers. Issue 36 (pp. 125–132). Minsk: BNTU. (in Russian)

3. Kastsiuchenka, Yu. A., Tamila, V. A., & Mantsivoda, A. L. (2025). *Influence of technological clearance on the quality of separation surface during blanking and piercing, increasing tool durability and controlling sheet stamping processes using AI*. In V. G. Zalessky (Ed.), Modern methods and technologies for creating and processing materials: collection of scientific papers. Book 1 (pp. 312–320). Minsk: FTI NAS of Belarus. (in Russian)

Thermal and acoustic insulation studies of composite lime and lime-cement plasters based on foam glass granules and thermally treated rice husks

Yonka Ivanova [1,2,*], Todor Partalin[3], Lyuben Lakov[4]
Sofia University St Kl.|Ohridski, Faculty of Physics, Sofia, Bulgaria[1]
Institute of Mechanics-Bulgarian Academy of Science,
Sofia, Bulgaria[2]
Sofia University St Kl.|Ohridski, Faculty of Mathematics and Informatics, Sofia, Bulgaria[3]
Independent Researcher[4]
yonivan@phys.uni-sofia.bg

Abstract: *This paper presents the results of studies on the thermophysical and sound-insulating properties of new composite materials intended for interior and exterior plasters in construction. The materials were developed on the basis of foam glass granules and thermally treated rice husks using a specialized methodology. The guarded hot plate method was used to investigate the thermal insulation properties of the composite plasters. Tests for determining the acoustic insulation characteristics were carried out under laboratory conditions using the two-chamber method. The results show that the newly developed composite plasters exhibit better thermal and acoustic insulation properties than the standard plaster compositions traditionally used in construction.*
Keywords*: COMPOSITE PLASTERS, FOAM GLASS GRANULES, RICE HUSKS, THERMAL CONDUCTIVITY COEFFICIENT, SOUND INSULATION COEFFICIENT*

1. Introduction

The optimization of the thermal and acoustic insulation properties of construction materials is of key importance for improving energy efficiency and comfort in buildings. Traditional plasters often suffer from limited insulating properties and insufficient resistance to external influences. In this context, new composite plasters based on foam glass granules and thermally treated rice husks represent an innovative solution combining environmentally friendly characteristics with improved physical and mechanical properties.

A number of researchers have investigated the possibilities for the application of composite materials based on foam glass granules [1,2,3]. In Bulgaria, a production facility for their production has been developed and put into operation [4].

Rice is one of the leading cereal crops worldwide and generates significant amounts of agricultural waste. The final product obtained from thermally treated rice husks, containing amorphous silicon dioxide, finds application not only in the ceramic industry [4], but also in other industrial fields, including plasters, due to its high reactivity.

The present study aims to present the results of experimental investigations on the thermophysical and sound-insulating properties of interior and exterior composite lime and lime-cement plasters incorporating these innovative additives. The tests were carried out using methods compliant with international standards, and the results were compared with data for traditional materials.

2. Experimental Part

2.1. Materials

The subject of the investigation consists of dried plaster-type samples with dimensions of (0.3 × 0.3) m and different thicknesses, composed of lime and lime-cement composite materials intended for interior and exterior applications.

The samples were obtained by adding foam glass granules and thermally treated rice husks, which replace part of the quartz sand in the plasters and improve a number of physicochemical properties. The foam glass granules had particle sizes below 3 mm and a bulk density of approximately 130 kg/m³.

Following the thermal treatment of the rice husks, ash containing amorphous silicon dioxide was obtained. The role of the active amorphous silicon dioxide is associated with a “cementing” effect, contributing to the strengthening and improvement of the plaster properties. In the investigated samples, rice husks thermally treated at 650 °C and ground into powder with a sedimentation size below 10 μm were used.

The inert fraction in the white dry lime interior plasters consisted of sand : foam glass granules : thermally treated rice husks in a volume ratio of 1 : 1.5 : 0.5. For the gray exterior plasters containing cement, the ratio was 1 : 1.5 : 0.4, while the volume fraction of cement was 0.1.

Table 1 presents the main characteristics of the samples, while Figure 1 shows the plaster plates.



a) *b)*

Fig.1. *Appearance of plaster samples: a) lime interior plasters; b) lime-cement exterior plasters.*

Table 1: *Material characteristics of composite plasters*

N	Code	Dimensions, m	Density, кg/m^3
	Composite lime interior plaster		
1	B-13-Int	0.3 x 0.3 x 0.013	675
2	B-20-Int	0.3 x 0.3 x 0.02	910
3	B-30-Int	0.3 x 0.3 x 0.03	1295
	Composite lime-cement exterior plaster		
4	S-13-Ext	0.3 x 0.3 x 0.013	671
5	S-20-Ext	0.3 x 0.3 x 0.02	859
6	S-30-Ext	0.3 x 0.3 x 0.03	1278

2.2. Methodology for Determining the Thermal Conductivity Coefficient of the Plasters

The investigation of the thermal insulation properties of the composite materials was carried out using a steady-state temperature method, in which the temperature gradient remains constant over time. The measurements were based on the passage of heat flow through parallel layers, taking into account the temperature difference between the two opposite sides of a sample of known thickness.

For the measurements, the Guarded Hot Plate method was used, employing a plate of reference material with a known thermal conductivity coefficient [6].

The tests were conducted in a thermal chamber with dimensions of 0.7 m × 0.7 m, insulated with mineral wool and aluminum foil. The square plates were placed horizontally inside the chamber, tightly fitted and without gaps, with the heater positioned on the lower side. A schematic representation of the experimental setup for determining the thermal conductivity coefficient of the plasters is shown in Figure 2.

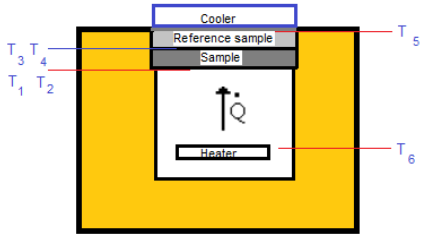


Fig.2. *Scheme of the experimental setup – thermal chamber*

The heat flow passing through the tested sample was assumed to be equal to that passing through the reference plate, which allowed the unknown thermal conductivity to be calculated through the ratio between temperature differences and layer thicknesses.

$$\dot{Q}_x = \dot{Q}_R \quad (1)$$

$$\lambda_x \Delta T_x \frac{A_x}{d_x} = \lambda_R \Delta T_R \frac{A_R}{d_R} \quad (2)$$

Where the subscript x denotes the tested plate, while the subscript R denotes the reference plate.

The area of the sample (A_x) was equal to the area of the reference plate (A_R).

The thicknesses of the sample plate and the reference specimen are denoted by d_x and d_R, respectively.

Eight thermocouples connected to an eight-channel temperature recorder with computer data acquisition capability were used for temperature measurements. Two thermocouples were positioned on the heated side of the sample and two on the opposite, non-heated side. A cooler was placed on the reference plate to ensure a controlled temperature difference.

The thermal conductivity coefficient λ_x of the investigated samples was calculated according to the following equation:

$$\lambda_x = \lambda_R \frac{T_{34} - T_5}{T_{12} - T_{34}} \frac{d_x}{d_R} \quad (3)$$

Where:
λ_R is the thermal conductivity of the reference plate (λ_R=0.036 W/mK),
T_{12} is the average temperature on the heated side of the sample,
T_{34} is the average temperature on the non-heated side of the sample,
T_5 is the temperature of the outer surface of the reference plate,
d_x и d_R are the thicknesses of the investigated sample and the reference plate..

The test specimens were placed in the thermal chamber and subjected to heating until a steady-state condition was reached, which required approximately 2 hours. The measurements then continued for an additional 5 hours to achieve higher accuracy.

2.3. Methodology for Acoustic Investigations

The sound insulation properties of the composite plasters were determined in accordance with the international standards EN ISO 10140-1, EN ISO 10140-2, EN ISO 10140-5, and EN ISO 717-1.

For this purpose, the two-chamber method was applied, in which the tested sample was placed between two chambers. The measurements were performed using specialized equipment consisting of two acoustically isolated rooms: a reverberation chamber with dimensions 700 × 600 × 600 mm and a receiving ("anechoic") chamber with dimensions 700 × 600 × 500 mm [5].

The reverberation chamber was constructed from multilayer materials such as gypsum board, particle board, mineral wool, and glass, and contained two broadband loudspeakers generating white noise in the frequency range 20–20000 Hz.

The receiving chamber was insulated with two layers of polyurethane foam and pyramid-type sound-absorbing foam, minimizing external noise. The equipment used for the acoustic investigations is described in greater detail in [5].

Sound pressure measurements were carried out using ECM999 microphones positioned in both chambers and processed using a dual-channel Real Time Acoustic Analyzer VT RTA-168 and MultiInstrument 3.9 Professional software.

By emitting white noise and recording the sound pressure before and after the sample, the difference in sound levels was determined and used to calculate the sound insulation coefficient R according to the equation:

$$R = L_{p1} - L_{p2} + 10(S/A) \quad (4)$$

Where:
L_{p1} is the average sound pressure level in the source room, dB,
L_{p2} is the average sound pressure level in the receiving room, dB,
S is the surface area of the tested partition sample, equal to the area of the test opening, m²,
A is the sound absorption of the receiving room, m².

The measurements were repeated four times, and the average values were taken to represent the acoustic characteristics of the plasters.

3. Results and Discussion

Thermal Insulation Properties

Figures 3 and 4 present the temperature variations over time during the experimental measurements of thermal conductivity for the white interior lime plaster and the gray exterior lime-cement plaster with different thicknesses (13 and 30 mm).

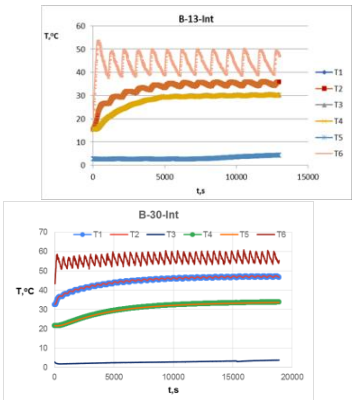


Fig.3*. Temperature changes during the testing of the interior lime plasters with thicknesses of 13 and 30 mm*

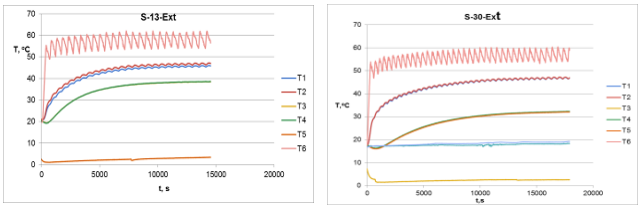


Fig.4. *Temperature changes during the testing of the external lime-cement plasters with thicknesses of 13 and 30 mm.*

The measured temperatures T_1 and T_2 were recorded on the heated side of the plates, while T_3 and T_4 represent the values measured on the non-heated side. T_5 and T_6 correspond to the temperatures measured on the reference plate and the heater, respectively.

The calculated thermal conductivity coefficients for the investigated samples, presented in Table 2, range from 0.067 to 0.08 W/mK. These values are significantly lower than the typical values reported in the literature for standard cement plasters, which vary between 0.9 and 1.4 W/mK.

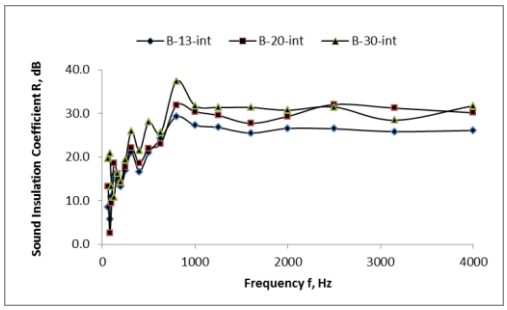
Table 2: *Thermal conductivity coefficients of composite plasters*

No	Code	Thermal conductivity λ_x. W/(m.K)	Uncertainty
1	B-13-Int	0.080	0.000503
2	B-20-Int	0.079	0.001115
3	B-30-Int	0.08	0.001097
4	S-13-Ext	0.069	0.039853
5	S-20-Ext	0.076	0.00158
6	S-30-Ext	0.067	0.001464

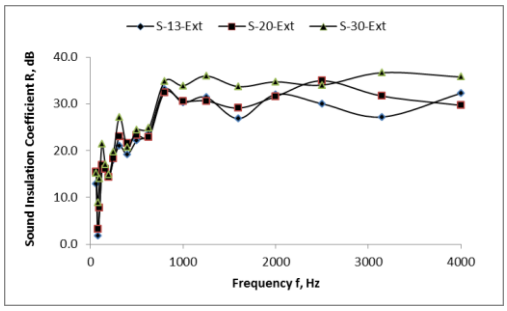
The low thermal conductivity coefficients indicate the high thermal insulation potential of the composite plasters, surpassing traditional materials in terms of energy efficiency.

Sound Insulation Properties

The results of the acoustic measurements presented in Fig. 5 show the variation of the sound insulation coefficients R as a function of frequency up to 4 kHz for the interior and exterior plasters, respectively.



a)



b)

Fig.5. *Sound insulation coefficients of the composite plasters a) lime interior plasters; b) lime-cement exterior plasters.*

According to the EN ISO 717 standard, the weighted sound reduction index Rw for airborne noise was calculated for each sample and is presented in Table 3.

Table 3. *Weighted Sound Reduction Index Rw*

No	Code	Weighted Sound Reduction Index Rw, dB
1	B-13-Int	26
2	B-20-Int	26
3	B-30-Int	26
4	S-13-Ext	28
5	S-20-Ext	28
6	S-30-Ext	28

The obtained indices confirm that the developed composite plasters provide good acoustic protection, while the exterior lime-cement plasters exhibit slightly higher sound insulation values.

This is due to the use of cement and their denser structure, which contributes to more effective attenuation of sound waves. The achieved values are competitive with those of traditional materials and demonstrate the applicability of the composite plasters in buildings with increased sound insulation requirements.

4. Conclusion

The present paper reports the results of investigations on the thermophysical and sound-insulating properties of newly developed composite lime and lime-cement plasters incorporating foam glass granules and thermally treated rice husks as innovative additives.

The conducted investigations demonstrate that the newly developed composite plasters possess significantly better thermal and acoustic insulation properties compared to standard cement plasters. In addition, the acoustic tests show improved sound insulation performance of the new materials, with weighted sound reduction index Rw values reaching up to 28 dB for the exterior plasters.

These results demonstrate the potential of the investigated composite plasters for application in construction aimed at improving energy efficiency and acoustic comfort.

3. References

1. L. Lakov, et al. *Machines. Technologies. Materials*, 15, (2021).
2. Kr.Toncheva, et al., *J. Chem. Technol. Metall.*, 58.4 (2023).
3. I. Jasińska, R. Dachowski, M.Jaworska-Wędzińska. Materials, 14 (2021).
4. L. Lakov, K. Marinova, Ts. Stanimirova, *Rev. Bulg. Geol. Soc.*, 86, 2 (2025).
5. L. Lakov, et al., J. Chem. Technol. Metall.,59 (2024).
6. M. Flori, V. Puțan, L. Vîlceanu. IOP Mater. Sci. Eng., 163 (2017).

New technology for producing a screw reinforcement profile from bar scrap of ferrous metals

Pavel Tsyba[1], Valery Chigirinsky[1], Sergey Kuzmin[1], Maxim Bogachev[1], Sergey Lezhnev[1], Evgeniy Panin[2]

[1]Rudny Industrial Institute, Rudny, Kazakhstan
[2] Karaganda Industrial University, Temirtau, Kazakhstan

Abstract: *This work is devoted to the development and research of a new technology for processing bar scrap from 40X steel to obtain high-quality finished metal products in the form of a screw reinforcement profile. The developed technology included two stages. At the first stage, the round-section bar scrap is formed on a radial-shear rolling mill to obtain conventional bars of the desired diameter and create initial conditions for the formation of an ultrafine grained gradient structure in the resulting screw profile. The second stage is the direct production of a screw profile with a gradient ultrafine-grained structure on a combined installation. Metallographic studies have shown that after the implementation of the second stage of obtaining a screw reinforcement profile, a gradient structure is observed in 40X steel, with equiaxed grains, the size of which lies within 1.2-1.4 μm in the peripheral region and to a greater extent with elongated, directional-oriented grains in the central region of the resulting reinforcement.*

Keywords: *RADIAL-SHEAR ROLLING, COMBINED INSTALLATION, BAR SCRAP, RECYCLING, SCREW REINFORCEMENT PROFILE, MICROSTRUCTURE.*

1. Introduction

T At the moment, almost 2 billion tons of steel are produced in the world, which is used for the manufacture of various metal products used in various industries. At the same time, it must be recognized that metallurgy is most often a "dirty" industry, since in this case there is quite a lot of environmental pollution. Therefore, metallurgical companies have been facing the task of "greening" metallurgy for more than a decade. And currently there are achievements in this direction. At the same time, the metal products turn into waste, which have served their service life (scrap), which also needs to be disposed of. One of the simplest and most frequently used methods of recycling ferrous scrap and alloys, as well as non-ferrous ones, is its remelting and further reuse.

If we talk about ferrous scrap metal, then in some countries of the world another method of its processing has long been put into practice, namely, recycling of some metal products that have served their service life by various methods of hot pressure treatment to obtain a finished commercial product. In our opinion, this method of processing ferrous scrap and alloys can be attributed to "green" technologies, as it allows to make a small contribution to improving the environmental situation in the world.

At the moment, in many countries of the world, a number of different technological processes have been developed for the processing of some metal products that have served their service life using hot pressure treatment into a ready-made commercial product. The founder of this direction of processing metal products that have served their service life by hot pressure treatment is the American scientist E.E. Slick, who at the beginning of the last century developed a technology for processing railway rails by hot rolling in calibers in order to obtain flange profiles [1]. But then the technology he proposed was not widely used in practice. It was only at the end of the 20th century that the world scientific community and manufacturers of metal products became interested in this direction. Here are just some works [2-5] devoted to the development and study of technologies for processing railway rails by hot rolling to produce various finished metal products. For example, one of these technologies, namely the technology of rolling railway rails into construction fittings, has found application at a metal rolling plant in Tula (Russia).

In addition to rolling railway rails into various finished metal products, technologies for recycling non-dimensional pipe segments are also being developed to produce marketable products in the form of a thin ribbon. Thus, in [6-8], two options for processing pipe segments into a cold–state tape were considered: the first option is flattening – rolling – separation, and the second option is flattening – separation - rolling. According to both proposed options, a high-quality thin steel strip with a length of 1.5 m was obtained.

The authors of the work [9] proposed a technology for using man-made waste from metallurgical production of non-ferrous trimming of copper pipes made by pressing to obtain a composite tape of the copper-steel-copper system. This technology includes the following stages of deformation: the draft of a pipe segment between the strikers, inside which a steel plate is placed; subsequent longitudinal rolling of the resulting billet.

Another promising way of recycling some metal products that have served their service life is their rolling on radial-shear rolling mills [10]. But most often this method is applicable only for recycling cylindrical metal products, for example, pumping rods [11] and used railway axles [12], as well as bar scrap of ferrous metals and alloys [13], including in the form of fittings [14]. In all cases, this method is based on the principle of hot radial shear rolling of a used so-called bar to a smaller diameter and subsequent use of the resulting bar of a smaller cross-section for its intended purpose. It should be noted that radial-shear rolling makes it possible to obtain long-length products from various materials with a gradient ultrafine-grained structure [15] and in addition, this method is the most technologically advanced and easy to implement compared to many other methods of metal forming, which realize severe plastic deformation.

As already noted above, radial-shear rolling makes it possible to process bar scrap of ferrous metals to obtain a marketable product in the form of bars for various purposes. In the future, these rods can be used, among other things, to produce various high-quality metal products, for example, hardware products or a coupling screw for formwork, but this will require the use of additional technological solutions.

Developing the direction of recycling of bar scrap using radial-shear rolling, a new technological process for processing bar scrap metal was proposed, combining radial-shear rolling and pressing through a screw matrix (Fig. 1). This technology will make it possible to obtain a high-quality commercial product from round-cross-section bar scrap in the form of a screw reinforcement profile with a gradient ultrafine-grained structure and with a given level of mechanical properties.

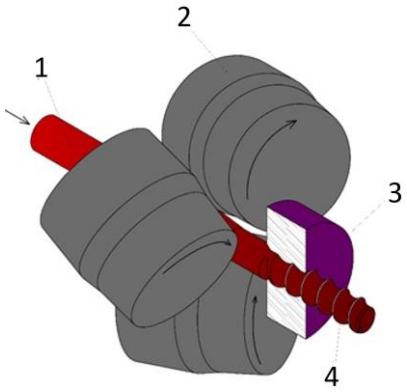


Fig. 1. *Combined method for obtaining a screw reinforcement profile from bar scrap of ferrous metals: 1 – bar scrap; 2– rolling rolls; 3 – screw matrix; 4 – screw profile*

Earlier in [16-17], using computer modeling in the DEFORM software, it have been already proved the possibility of implementing this combined process and determined the most rational geometric and technological parameters for its implementation. The purpose of this work is to confirm in practice the possibility of obtaining a screw profile with a gradient ultrafine-grained structure during the implementation of a new combined method shown in Fig. 1.

2. Materials and Methods

A laboratory combined installation for the production of a reinforcing profile was assembled on the basis of the radial shear rolling mill RSR 10-30 (Fig. 2a), on which a screw matrix was installed (Fig. 2b) with a maximum diameter of the working screw channel of 20 mm. Bar scrap, namely studs (GOST 9066-75, type-A1), was used as the initial blanks for the physical experiment with size of M36 x 150 mm made of 40X steel, which have served their service life. Before deformation, these studs were subjected to homogenizing annealing.

The proposed technology for recycling bar scrap in the form of studs includes two stages. At the first stage, the pins with a diameter of 36 mm, previously subjected to homogenizing annealing, were heated to a temperature of 1150 ± 10 °C and kept at this temperature. Further, these studs were deformed on the RSR 10-30 radial-shear rolling mill according to the reversible scheme [13] to a diameter of 24 mm, that is, 4 passes were carried out according to the scheme ∅36→∅33→∅30→∅27→∅24 mm.

Before the implementation of the second stage, the rods with a diameter of 24 mm obtained at the first stage were heated to a temperature of 1000 ± 10 °C. The second stage of the stud recycling technology was implemented on a combined installation assembled at the RSR 10-30 radial-shear rolling mill (Fig. 2c). The deformation process of preheated rods on the assembled combined installation was as follows: first, the rod was rolled in the working cage of the RSR 10-30 mill with an absolute compression in diameter of 5 mm, at the outlet of which it entered the screw matrix and due to the pushing force created by the rolls, and pushed through the screw channel. As a result, a screw profile was obtained on the deformed bars (Fig. 2d).

a)



b)



c)



d)



Fig. 2. *Radial-shear rolling mill RSR 10-30 and the installation assembled on it to produce a reinforcing screw profile: a - mill RSR 10-30; b – screw matrix; c - working cage of the mill and the installed screw matrix; d - resulting screw profile*

3. Results and discussion

Metallographic studies of the resulting screw reinforcement profile, as well as those obtained on the SVP 14-40 radial-shear rolling mill, were carried out using a Quanta 200i 3D scanning electron microscope. The microstructure was studied in the center and on the periphery of the section of the obtained rods with a diameter of 24 mm and a screw profile. The results of metallographic studies are shown in Fig. 3.

An analysis of the microstructure evolution showed that the initial structure of the studs subjected to homogenizing annealing has a typical coarse-grained ferrite-pearlite structure with an average grain size lying in the range of 45-60 μm. The microstructure of the peripheral region of a 24 mm diameter bar obtained by radial-shear rolling has a predominantly equiaxed ultrafine-grained character with an average grain size in the range of 1.6-1.8 μm (Fig. 3a). Structural striation is observed in the central zone of these bars, i.e. grains elongated in the direction of rolling are observed with dimensions lying in the range of 6-10.5x1.1-17 μm (Fig. 3b). That is, a gradient structure was obtained in a 40X steel bar after radial shear rolling, as expected.

Analysis of the microstructure of 40X steel after the implementation of the second stage of deformation, i.e. after obtaining a screw profile, showed that by installing a screw matrix on a radial-shear rolling mill, we not only obtain a screw reinforcement profile, but also additionally modify the previously obtained gradient structure of 40X steel. At the same time, in the central and peripheral regions of the resulting screw reinforcement profile, the grain size has further decreased. In the peripheral region, the grain size decreased to an average size of 1.2-1.4 μm (Fig. 3c). In the central region of the resulting screw profile, grains elongated in the direction of rolling are also observed to a greater extent, due to the preliminary deformation of the initial studs according to the standard reversible radial-shear rolling scheme, but due to additional twisting of the rod and back pressure arising from the side of the screw matrix, a partial change in the structure previously obtained at the first stage occurred. In particular, in the central zone, a partial restructuring of the existing striped texture began to occur: most of the grains in this area also remained elongated, but their disorientation in directions appeared, and equiaxed grains were also observed in this area (Fig. 3d).

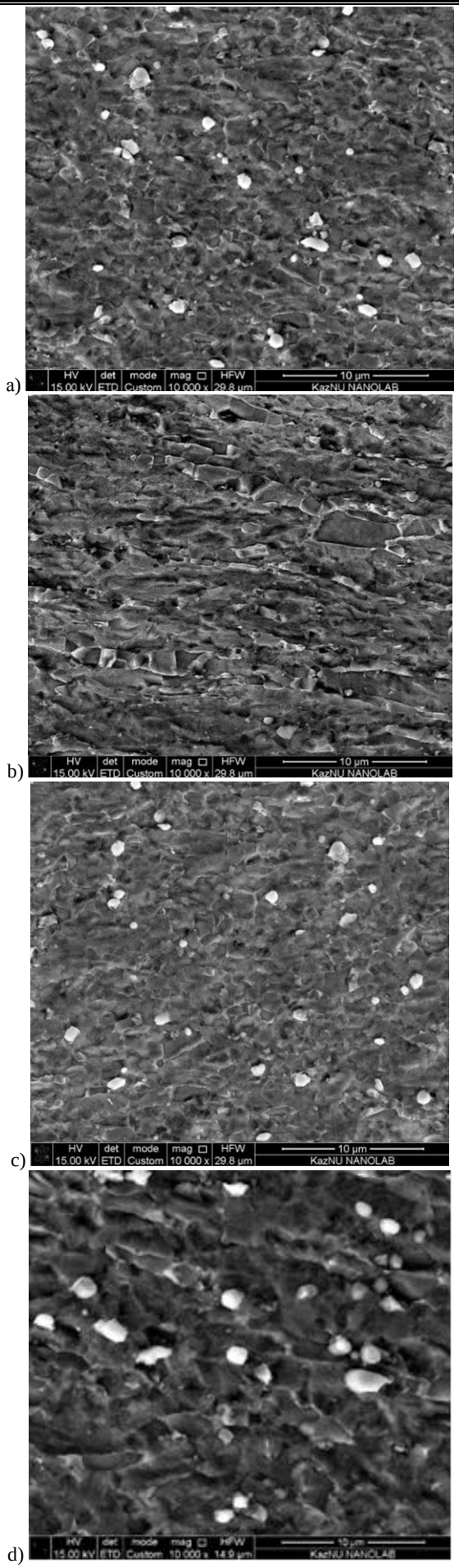


Fig. 3. *Microstructure of 40X steel: a, b – periphery (a) and center (b) of the bar after radial-shear rolling to a diameter of 24 mm; c, d - periphery (c) and center (d) of the resulting screw reinforcement profile*

Conclusion

The conducted research has proved in practice that the proposed combined technological process for obtaining a screw profile is feasible. This process can be used for recycling bar scrap of ferrous metals to obtain a finished commercial product in the form of a screw profile and, accordingly, it can be attributed to "green" technologies.

This research was funded by the Science Committee of the Ministry of Science and Higher Education of the Republic of Kazakhstan (Grant no. AP19678682 and AP14869135).

References

1. E.E. Slick, U.S. Patent 1,086,789. (1914).
2. V.K. Smirnov, V.A. Shilov and A.M. Mikhailenko: Steel Vol. 2 (1995), P. 46-48.
3. B.D. McGahhey, US Patent 4,982,591. (1991).
4. Y.B. Bakhtinov: Prod. Roll. Prod. Vol. 7 (2000), P. 2-4.
5. S.I. Badyuk and A.I. Leshchenko: Process. Mater. Press. Vol. 4 (2010), P. 162-167.
6. Yu.N. Loginov and G.V. Shimov, Method for processing non-dimensional pipe segments, RU Patent 2786705, 2022.
7. G.V. Shimov, Yu.N. Loginov and N.I. Bushueva: Chernye Metally Vol. 9 (2023), P. 29-33.
8. N.I. Bushueva, G.V. Shimov and Yu.N. Loginov: Proceedings of the International Scientific Conference "Modern materials, advanced production technologies and equipment for them", St. Petersburg, 2023, P. 87-88.
9. N.I. Bushueva: Proceedings of the international scientific and practical conference "Promising engineering technologies", St. Petersburg, 2024, P. 422-425.
10. S.P. Galkin, RU Patent 2,293,619. (2007).
11. S.P. Galkin and B.A. Romantsev: Eng. Pract. Vol. 9 (2014), P. 58-61.
12. V.V. Grevtseva and S.P. Galkin: Proceedings of the 72nd Days of science of students of Nust Misis, Moscow, 2017, P. 297.
13. S. Lezhnev, A. Naizabekov, E. Panin, I. Volokitina and D. Kuis: Metalurgija Vol. 60 (2021), P. 339-342.
14. S.N. Lezhnev, A.B. Naizabekov, I.E. Volokitina, E.A. Panin and E.I. Kuldeyev: Complex Use of Mineral Resources Vol. 1 (2021), P. 46-52.
15. S.P. Galkin, Y.V. Gamin, A.S. Aleshchenko and B.A. Romantsev: Chernye Metally Vol. 12 (2021), P. 51-58.
16. Lezhnev, A. Naizabekov, E. Panin, A. Tolkushkin, D. Kuis, A. Kasperovich and R. Yordanova: Modelling and Simulation in Engineering Vol. 2023 (2023), 7348592.
17. Lezhnev, E. Panin, A. Tolkushkin, D. Kuis and A. Kasperovich: Journal of Chemical Technology and Metallurgy Vol. 58 (2023), P. 955-960.

Monitoring the production process in production organization

Miroslav Prístavka[1*], Hristo Beloev[2], Karol Durczak[3], Mitko Nikolov[2], Krzysztof Kapela [4]
Slovak University of Agriculture in Nitra, Slovakia[1]
Angel Kanchev University of Ruse, Ruse, Bulgaria[2],
Poznan University of Life Sciences, Poznan, Poland[3]
University of Siedlce, Poland[4]
miroslav.pristavka@uniag.sk

Abstract: The article deals with the assessment of the suitability of the manufacturing process and the analysis of the gear runout. The measurements were carried out using the 3D measuring device Wenzel WGT 280. The Palstat CAQ software was used to evaluate the process, while control charts for individual values and the sliding range were applied. The average value of the process reached 0.1460 and the sliding range was 0.00409. The suitability of the process was assessed using the Cp and Cpk indices with a required value ≥ 1.33, while the calculated values were 1.47 and 1.34. The results confirm that the monitored process is suitable. Subsequently, a comparison of the runout before and after heat treatment - nitriding was performed. The specified tolerance limits (0 μm to 0.0320 μm) were not exceeded, which confirmed the satisfactory state of the process even after the treatment.
Keywords*: QUALITY, PRODUCTION PROCESS, CONTROL DIAGRAMS*

1. Introduction

The approach to managing an organization is no longer just a competitive advantage, but also one of the conditions for certification. The competitive environment leads organizations to deal with their processes and look for opportunities to improve them. [12] The power of the customer has increased the importance of marketing specialists who study the market and look for new forms of competition. Price is no longer the only decisive factor. It is precisely due to the influence of the competitive environment that the problem of insufficient adaptability of companies with a traditional organizational structure has become apparent. Process organizations with effectively functioning quality management are able to respond quickly to changes and maintain or improve their position in the market. [1] However, not only the ability to respond quickly to changes, but also the willingness to accept change as an everyday part of the organization's life is a key factor in success. [4] Just as product development time is constantly shortening and it is necessary to constantly seek new improvements and innovations, an organization must, if it wants to be successful, take this attitude not only to its products, but also to its processes. Appropriately selected monitoring and measurement of processes will reveal weaknesses in the organization, which are also opportunities for process improvement. [11] The quality system is primarily about continuous improvement of everything that happens in the organization and therefore affects practically all company processes. Improvement is a de facto necessity for organizations operating on the market. [7] Whoever stops improving will be overcome by the competition. Quality management and improvement are therefore a key and natural part of the normal management of successful organizations. [6]

We focused on the gear manufacturing process and the measurement of gear runout on the Wenzel WGT 280 3D measuring stand. [3] We will evaluate the suitability of the manufacturing process using the Palstat CAQ software. Control is used in cases where it is not possible to create logical subgroups. [2] Finally, we will compare the gear runout before and after heat treatment - nitriding at an external supplier, how large the deformations were there and whether the prescribed tolerance value was observed.

There are various suitable methods for this type of quality improvement in organizations, and it is up to them which method to use in improving quality in their conditions. [10]

Nowadays, product quality is constantly improving, so it is more than necessary for organizations to place high emphasis on quality management and monitoring. It is imperative to ensure that the products are of the highest quality. This is what the competitiveness of the organization and its survival in the constantly changing market are built on. [5] The introduction of statistical methods is an important tool for organizations to control the state of processes, which helps to correct and improve the final products. Therefore, in my diploma thesis, I decided to focus on the use of statistical methods in production processes. [8]

In the article, we focused on evaluating the capability of a selected production process using the Palstat CAQ software. Using the control diagram for individual values and sliding range and using capability indices, we determined whether the production process is capable. Finally, we compared the measured values of runout before and after heat treatment. [14]

2. Materials and Methods

Different types of gearing can be seen in mechanical engineering, automotive, aviation and other industries. The wide application of gears in mechanical engineering and in everyday use has led to the emergence of a large number of methods for producing gears. The production method and the technology used are chosen based on the requirements for gear accuracy.

In a manufacturing organization that produces gears, we selected 50 consecutively manufactured wheels per shift and focused on gear runout. The measurement was carried out on a Wenzel WGT 280 machine. From the measured values, we will determine the process capability and the sliding range in the Palstat CAQ software.

Subsequently, we will focus on comparing the gear runout Fr. We compare the measured values after production with the values measured after heat treatment (nitriding). The measurement will be carried out on the same Wenzel WGT 280 measuring machine at the input inspection. We will compare the differences between the measured values and make the average change in the runout Fr of the gears. The component is made of ETG 88 – 44SMn28(1.0762) material with a diameter of 100 mm. This steel grade generally shows relatively good machinability on machine tools. Gear milling (Fig. 2) on a Liebherr LC 180 milling machine (Fig. 1) using the rolling method.



Fig. 1 *Liebherr LC 180 milling cutter*

Hobbing is the most common method of gear production. This method uses hobbing cutters, which are cylindrical shaped cutters that represent a worm that meshes with machined gear. The spiral of the worm is interrupted around the circumference by milled grooves that create the front surfaces of the tooth edges.



Fig. 2 Part after milling

Performing an input inspection of gear deformation on a Wenzel WGT 280 machine.

The Wenzel WGT280 (Fig. 3) is a 3D measuring device designed for gear measurement. It offers a higher measurement speed and therefore more efficient inspection from small to large wheels. The software developed for this device provides optimal 4-axis inspection and high measurement performance. The measuring device is equipped with modular software packages.



***Fig. 3** 3D measuring machine Wenzel WGT 280*

The monitored gear runout parameter (Tab. 1) Fr has a tolerance value from 0 μm to 0.0320 μm.

Palstat CAQ Software Palstat CAQ and the modules it consists of are computer software used to support quality management. Palstat CAQ information software fully covers the requirements of ISO 9001, ISO/TS 16949 and also the requirements of VDA (Čablová 2013). The software was created based on the optimization and increase of the performance of the quality management system. Its main task is the regulation of variable quality characteristics with normal distribution. Production process control and statistical analysis follow each other and stabilize the production process in three steps:

- determine the instability of the production process,
- bring the production process from an unstable to a stable state,
- try to maintain the process in a stable state

Quality monitoring:

- Supplier evaluation – monitoring their performance,
- Monitoring, measurement of production processes – SPC – statistical process control,
- Monitoring, measurement of parts / products, dimensional control and functional tests,
- Incoming inspection – parts and products,
- SQC – production control,
- Inter-operational inspections of parts / products,
- Output inspection – parts and products.

Tab.

Mating gear: BM1-6 / Center distance a = 35,00 mm		
Description	**Symbol**	**Finish hobbing**
		B06-R2-6-FT
Tip diameter [mm]	d_a	63,03-0,02
Root diameter [mm]	d_f	59,77
Module [mm]	m_n	0,65
No. of teeth	z	84
Theoretical profile shift factor (zero backlash)	x	+0,05832
Pressure angle [°]	α	20°
Helix angle [°]	β	27° R
Tooth length [mm]	b	9,00
Chordial dimension over two teeth		
Chordial dimension over two teeth min [mm]	W_k min	24,9935
Chordial dimension over two teeth max [mm]	W_k max	25,0171
No. of teeth for span measurement	Z meß	13
Diametral dimension over balls		
Diametral dimension over balls min [mm]	Mdk min	62,6276
Diametral dimension over balls max [mm]	Mdk max	62,6945
Ball diameter [mm]	Ø Dm	1,10
Tip chamfer [mm]	h_k	0 ... 0,10
Tip relief [µm]	c_a	5 ± 2
Mesh distance [mm]	g_a	2,5829
Crowning [µm]	c_g	8 ± 2
DIN Quality		8
Gas nitrocarburisation depth [mm]	Nht	0,25 ... 0,40
Compound layer thickness [µm]	VS	9 ... 12
Oxidisation layer thickness [µm]	OS	1 ... 1,50
Surface hardness [HV]		650+50
Radial size of addendum reduction	h_R	0,455
Machining allowance [mm]	q	-

1

3. Results

Gears are among the most important machine components. As more and more high-speed and high-performance machines are used, which must have high efficiency and quiet operation, ever greater demands are placed on gears for accuracy. The demands placed on gears depend on the conditions and purpose of their use. Gears have different shapes and therefore it is necessary to use different types of measurements of individual quantities.

In terms of correct engagement and torque transmission, the gears that mesh together must meet the following conditions:

- Accuracy and correctness of the tooth thickness,
- Accuracy and correctness of the tooth shape and tooth surface quality
- Minimum runout.

A sample of 50 gears selected by us is measured on a Wenzel WGT280 3D measuring machine (Fig. 4). The basis for accurate measurement is the cleanliness of the machine and degreased, deburred gears (Fig. 5). The measured gears were stored at the measuring center for 24 hours at a temperature of 21ºC to prevent the occurrence of factors affecting the measurement results.

Calibration of the measuring device consists of two parts:

- calibration of the diameter of the measuring contact,
- calibration of the axis of the device.

Starting the measurement program – the measuring probe finds a reference point and centers itself. The evaluation is determined on 4 teeth at 90º apart and evaluates the side and profile of the tooth from the measured values. It then measures the spacing of each tooth and evaluates the tooth runout based on the measured values.

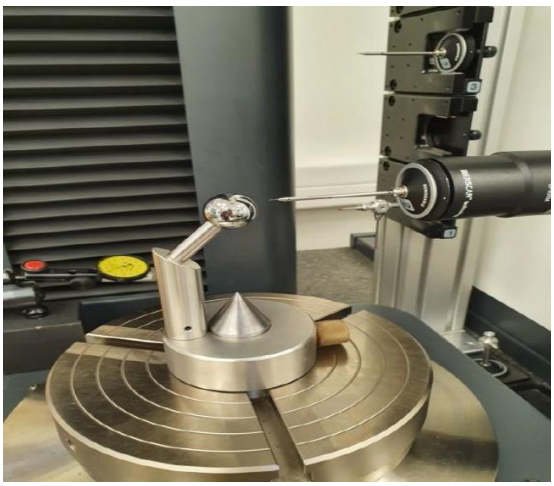


***Fig. 4** Calibrating the measuring probe*

Mounting the measured gear into the fixture.

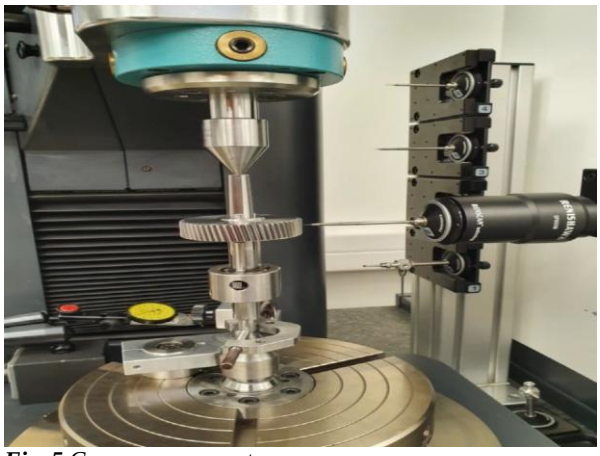


Fig. 5 *Gear measurement*

Tab. 2 Measurement report

Profile and Lead Inspection (1/2)

BG06-R4-1/BAU2500710/Finish Hobbing		BG06-R4-1	#20
Remark:		Unit of measure: mm	
Operator: T. Kluciar			
Order-No.: 10847453			
z: 58	an: 20°0'0"	Db: 55.2426	x: 0.365734
mn: 1	ß: 10°0'0" L	D0: 58.8947	b: 15

Diameter: 1.250 mm; 20 µm; 500 : 1; Low pass 4; V: 10.0mm/s

DIN 3961/62	Q	[...]	x	#44	#30	#15	#1	Tooth	#1	#15	#30	#44	x	[...]	Q
	3	0.0/16.0	2.3	2.4	2.9	2.9	1.1	Fα	2.8	1.4	2.1	2.1	2.1	0.0/16.0	3
!=8	4	0.0/12.0	1.8	1.7	1.6	2.9	0.9	ffα	2.8	1.1	1.3	1.6	1.7	0.0/12.0	4
=4	4	-10.0/10.0	-0.0	1.8	-2.5	0.1	0.5	fHα	0.1	0.9	1.1	-1.9	0.1	-10.0/10.0	3
		6.0/10.0	6.3	7.4	4.9	4.7	8.1	Caa	7.4	10.2	9.3	8.0	8.7	6.0/10.0	

Top: 2.500 mm; 4 : 1; 20 µm; 500 : 1; Cß: 80->80%; Lß: 80->100%; Low pass 4; V: 10.0mm/s

Q	[...]	x	#44	#30	#15	#1	Tooth	#1	#15	#30	#44	x	[...]	Q
	0.0/9.0	4.7	6.7	5.6	2.7	3.9	Fß	2.7	2.8	1.7	2.7	2.5	0.0/9.0	
	0.0/5.5	2.7	3.4	3.4	1.9	2.2	ffß	2.3	1.9	1.5	1.4	1.8	0.0/5.5	
	-6.0/0.0	-3.4	-6.0	-3.7	-1.2	-2.5	fHß	0.4	1.2	0.2	-2.4	-0.1	-3.0/3.0	
	6.0/10.0	7.6	7.7	7.3	7.2	8.1	Cß	8.2	9.1	8.4	8.3	8.5	6.0/10.0	

The actual curves of the profiles are translated by theoretical curves and are projected into straight lines (Tab. 2). These curves should ideally be symmetrical. If they are not symmetrical, this is due to the angular deviation of the profile. In reality, care must be taken to ensure that their dispersion is as small and one-sided as possible.

Pitch and Runout Test (2/2)

BG06-R4-1/BAU2500710/Finish Hobbing		BG06-R4-1	#20
Remark:		Unit of measure: mm	
Operator: T. Kluciar			
Order-No.: 10847453			
z: 58	an: 20°0'0"	Db: 55.2426	x: 0.365734
mn: 1	ß: 10°0'0" L	D0: 58.8947	b: 15

	Standard		!=Q	=Q	[...]	Actual	Min.	Max.
fp	20 µm							
DIN 3961/62	fp	8	4	14.0		3.0	#13	#40
DIN 3961/62	fu	8	4	18.0		4.3		#13
	fum					1.8		
fp	20 µm							
DIN 3961/62	fp	8	6	14.0		5.1	#55	#56
DIN 3961/62	fu	8	7	18.0		9.6		#56
	fum					4.0		
Fp	20 µm							
DIN 3961/62	Fp	8	4	50.0		13.9	#31	#4
DIN 3961/62	Fpz/8	8	4	32.0		6.7	#12	#19
Fp	20 µm							
DIN 3961/62	Fp	8	6	50.0		18.9	#24	#50
DIN 3961/62	Fpz/8	8	5	32.0		9.1	#35	#42
Fr	20 µm							
DIN 3961/62	Fr	8	6	32.0		15.0	#46	#17

Task	Actual	Min.	Max.	Nominal	U.tol	L.tol	Dev
Span measurement(n= 8)	23.2036	23.1980	23.2091	23.2214	0.0000	-0.0235	-0.0178
Dim. over two balls(D= 1.750, Z= 7.500)	61.9690	61.9656	61.9739	62.0150	0.0000	-0.0450	-0.0451

Task	Actual	Min.	Max.	Nominal	U.tol	L.tol	Dev
Diameter: Tip circle (Z)= 7.500 (4P)	62.0414	62.0400	62.0427	62.0600	0.0200	-0.0200	-0.0186
Diameter: Root circle (Z)= 7.500 (4P)	57.1660	57.1657	57.1662	57.2900	0.1500	-0.1500	-0.1240

Results from Palstat CAQ software

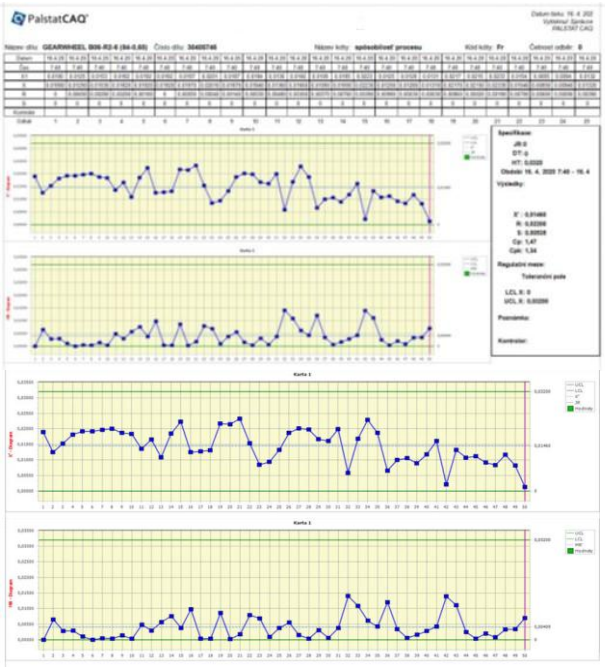


Fig. 6

Product quality depends on a properly set and statistically managed process. Certified organizations strive to create the most suitable conditions for managing their process, which includes all quality tools and methods.

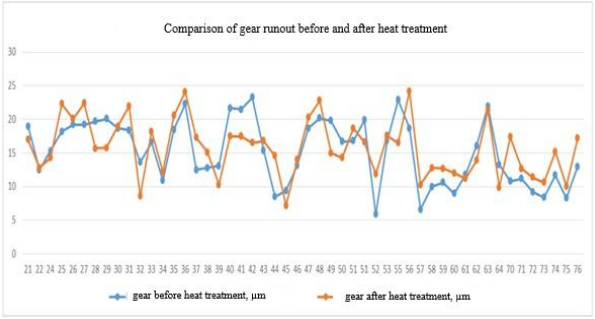


Fig. 7 *Comparison of gear runout before and after heat treatment*

The table we created shows the differences in the measured values of gear runout before and after heat treatment (Fig. 6). All values are in the given tolerance field from 0 µm to 0.0320 µm. When comparing, we can notice that not all values increased (Fig. 7), but in some cases we got below the basic value, which results in surface deformation during heat treatment in our case of nitriding.

In the presented article, we investigated the capability of the production process. We evaluated the control charts for individual values, sliding range and process capability indices. They showed us that the process is in a capable state. By introducing control charts to other production processes, the organization can reduce the number of non-conforming products to a minimum. By applying them and with the help of the developed methodology, they can identify definable causes, eliminate them from the process and minimize time and economic losses. Process capability verifications can be applied to almost any process, improving an organization's competitiveness.

4. Conclusion

A perfectly designed quality monitoring in the production process must be understood and controlled by employees, whose task is to know the goals and quality policy. Meeting these goals should be their priority in order to meet the demanding requirements of all customers. An organization that wants to progress should pay great attention to improving quality and proactively seek opportunities for its improvement. And that is why it is a never-ending process that includes not only employees, but also all activities and departments.

Measuring instruments have a leading position in the field of quality. It is very important that the values measured by the relevant devices correspond to reality even after a certain period of use of the measuring instrument. It is advisable for organizations to use adequate measuring instruments, appropriate measurement and monitoring methods, and also to use the necessary documentation. This consists of operational procedures that precisely indicate and standardize how it is necessary to proceed in the individual steps when performing a measuring operation.

Any deviation or inaccuracy from the required values can be detected by measuring products. Whether the product is satisfactory can then be determined according to the tolerances given. If it is not, it is necessary to suspend production and take the necessary measures so that customer satisfaction is not jeopardized.

In the article, we focused on the measurements of gears and their tooth runout. The runout of the tooth flanks results in uneven gearing, uneven engagement, noise and vibration of the system. Therefore, together with the quality requirements, zero or as little runout as possible is most appropriate. This deviation is caused by improper clamping of the workpiece during gearing or machine instability.

Acknowledgement

This paper was created with financial support of the grant project Kega no. 012SPU-4/2025" Implementation of modern methods in the Smart Farm 4.0 concept for sharing data in teaching for agricultural and forestry sciences"

References

[1] GRYNA FRANK, M. – CHUA RICHARD CH. – DE FEO JOSEPH, A. 2007. Juran quality planning and analysis for enterprise quality. Boston: Mc Grw Hill. 2007. 774 s. OCLC 911062606

[2] HRUBEC, J., 2001. Riadenie kvality. 1. vydanie. Nitra : SPU, 2001. 203 s. ISBN 80-7137-849-6

[3] HRUBEC, J. – CSERVENÁKOVÁ, J., 2016. Inžinierstvo kvality produkcie. 1. vydanie. Nitra : SPU, 2016. 180 s. ISBN 978-80-552-1536-5.

[4] HRUBEC, J – VIRČÍKOVÁ, E. a kol., 2009. Integrovaný manažérsky systém. 1. vydanie. Nitra : SPU, 2009. 543 s. ISBN 978-80-552-0231-0.

[5] KLUČIAR, T., 2020. Sledovanie výrobného procesu vo výrobnej organizácii, diplomová práca, SPU v Nitre.

[6] KORENKO, M. – PRÍSTAVKA, M. – DRLIČKA, R. 2015. Manažérstvo kvality procesov, 1. prepracované vydanie, SPU Nitra : 2015. 144 s. ISBN 98780-552-1316-3

[7] MATEIDES, A. a kol., 2006. Manažérstvo kvality. Bratislava: EPOS, 2006. 751 s.

ISBN 80-8057-656-4

[8] NENADÁL J., a kol. 2008. Moderní managment jakosti – principy, postupy, metody. Praha: Managment Press, 2008. 377 s. ISBN 978-80-7261-186-7

[9] PLURA, J. 2001. Plánování a neustálé zlepšování jakosti. 1.vydanie. Praha: Computer Press, 2001. 244 s. ISBN 80-7226-543-1

[10] POWELL, Th., 1995. Total quality management as competitive advantage [cit.2019-10-05]. Vol.16 URL < https://doi.org/10.1002/smj.4250160105>

[11] PRÍSTAVKA, M. – HRUBEC, J. 2013. Riadenie kvality vo výrobnej organizácii. 1.vydanie Nitra: SPU, 2013. 130 s. ISBN 978-80-552-1007-0

[12] RUSSEL, R.S. – TAYLOR, B.W. 2006. Operations management. Wiley. 2006. 836 s. ISBN 8126508817

[13] TEREK, M. – HRNČIAROVÁ, Ľ., 2004. Štatistické riadenie kvality. Ekonomická univerzita Bratislava, 2004. Edícia ekonómia, ISBN 80-89047-97-1

[14] VEBER, J. a kol., 2006. Mnagement kvality, enviromentu a bezpečnosti práce. Legislativa, metody, sys-temy, prax. Praha: Nakladatelství Management Press, s.r.o, 2006, 1. vydanie, 360 s. ISBN 80-7261-146-1

Features of modeling complex twist deformation for obtaining multilayer metal cord structures

Vyacheslav Tomilo[1], Yury Bobarikin[2], Yury Martyanov[2]
Physical and Technical Institute of the National Academy of Sciences of Belarus, Minsk, Belarus[1]
Sukhoi State Technical University of Gomel, Gomel, Belarus[2]
[1] E-mail: stamila@rambler.ru, [2] E-mail: bobarikin@outlook.com, you_rock935@outlook.com;

Abstract: *Features of modeling multilayer metal cord structures are shown. Data on the parameters of the numerical model of metal cord twisting and stretching are given. The dependences of the magnitude of stresses during the destruction of metal cord on the diameter of wires for various metal cord structures are determined. It is shown that symmetrical steel cord structures are less susceptible to a decrease in aggregate strength. The difference between the breaking forces of a multilayer symmetric metal cord with a core is about 10%. It is shown that with an increase in the wire diameter, there is no significant increase in the fracture stresses.*
Keywords*:* STEEL CORD, MODELING, PROPERTIES, STRESSES

1. Introduction

The metal cord is a twisted product in the form of a three-dimensional spiral. In the process of twisting the metal cord, the wire is subjected to torsional and bending stresses. This, combined with the stress-strain state of the wire during drawing and twisting, as well as the level of internal residual stresses that occur in the wire after drawing, makes it impossible to predict changes in the properties of the wire and cord using known computational methods. For the correct calculation of the metal cord twist, an accurate forecast of the level of internal residual stresses that occur during drawing is required.

Uneven distribution of residual stresses in the wire after drawing, as well as a high value of residual stresses after twisting the metal cord, can worsen the properties of the metal cord.

The development of an adequate computer model for twisting metal cord from thin wire, assessing the level of residual stresses in the metal cord, is a promising area of study of metal cord from thin wire. The simulation itself allows you to save time and material resources necessary for laboratory tests. However, in order to use the numerical model correctly, it is necessary to check its adequacy and, if necessary, introduce correction factors.

The main method of studying the magnitude of residual stresses is the method of numerical modeling. Using this method, based on the finite element method, allows us to obtain a general picture of the stresses and deformations of the wire in the straightening device with high calculation accuracy. The main requirements in numerical modeling are the correct construction of the model in terms of geometry, the choice of initial and boundary conditions, as well as the choice of the optimal type of finite element grid. The accuracy and duration of calculations, as well as the adequacy of the constructed model, will depend on the selected type of final element and its geometric shape.

Numerical modeling, unlike analytical methods, shows with sufficient accuracy the picture of stresses and deformations not only in the elastic, but also in the plastic deformation zone. This is the main advantage over analytical calculations.

Verification of the results of numerical modeling is carried out by comparing the results of analytical calculations with the simulation results.

Verifying the adequacy of a computer model is a complex complex task. To verify the adequacy or bring the model to an adequate one, it is necessary to use a direct check of the desired values. This means that it is necessary to match the value of the same parameter obtained in a different way to a certain value of the output parameter of the model. The difference in values is unavoidable and is an error. The errors are estimated using relative values. If the difference between the value obtained in the model and the value obtained by another method is significant, then it is necessary to enter a correlation coefficient or dependence to be able to translate the model values. The difference in the values of the output parameters of the model is due to simplifications and idealization of some parameters of the model.

After twisting, the stress-strain equivalent state of the metal cord is nonequilibrium. The equilibrium stress-strain state of the metal cord means that the level of internal residual stresses is equal to or close to zero. At this level of residual internal stresses, relaxation will be minimal. This means that the finished metal cord will have high technological properties.

In the process of twisting a metal cord, tensile, torsional and bending stresses and deformations act on the wire. The equivalent deformation is the reduced deformation to assess the total deformation effect on the wire when winding in a rope machine. Areas of large wire deformations are provided along the twisting path compared to other areas of the cable car. In such zones, the stages of twisting wires into a metal cord are carried out, the deformation of individual wires can be carried out in different directions. However, in absolute terms, the total equivalent deformation always increases. The diameter of the metal cord, the aggregate strength, and the strength of adhesion to rubber depend on the wires and their location in the metal cord.

The non-twisting of the metal cord is ensured by additional twisting of the strand in the torsion device to achieve deformation of the wires in the plastic region. After additional twisting, the pitch of the metal cord increases slightly and then unwinds in the opposite direction in the area of elastic deformations. The amount of additional twisting of the metal cord is created by the rotational speed of the torsion device.

In multilayer symmetrical structures of metal cord with a core, there is a feature associated with the pattern of contact interaction. From the point of view of modeling, it is necessary to take into account the initial stress level in the wires, as well as the contact interaction between the wires.

The main property of multilayer metal cord is its aggregate strength. This property shows how much the actual strength of the metal cord corresponds to the theoretical strength. Due to the complex twisted structure, the metal cord does not collapse simultaneously during stretching, but gradually: first one wire collapses, then the next, etc. Ideally, all the wires of the metal cord should be destroyed at the same time. However, this is not happening. Modeling the process of twisting and stretching the metal cord will allow us to determine the dependencies and understand the mechanism of behavior of wires in the metal cord structure during stretching and fracture.

The finite element method and numerical modeling were used to study twisting and fracture.Numerical models of twisting of multilayer metal cord structures based on five wires are constructed: 1+4x0. 25HT; 1+4x0. 30HT; 1+4x0. 35HT. Numerical models take into account the contact interaction of wires in the structure. The wire material model takes into account the features of plastic deformation during twisting, mechanical properties of thin wire, taking into account the processes of fine drawing, and also contains a Johnson-Cook damage model[1].

The simulation was performed with the following parameters:

The total number of grid elements is 370 thousand elements on average.

The type of finite element grid is tetrahedral.

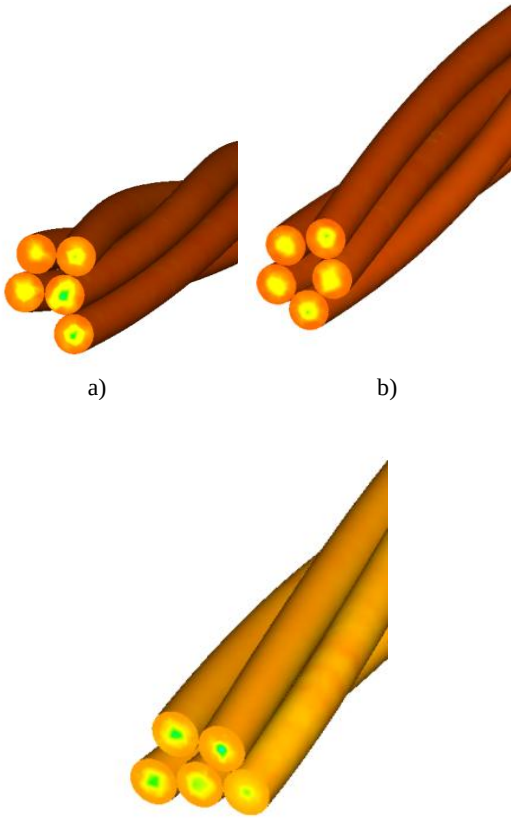
The tension of the wires when twisting is 40 N.

The rotor speed is 3000 rpm.

The twist pitch is 15 mm.

Material-Steel 80.

The parameters of the twist are close to the current parameters of the twist in the actual production of metal cord. Twisting of wires is made on two steps of a metal cord. The results of twisting are shown in Figure 1.



a) b)

c)

Fig. 1 Results of twisting metal cords:
a) 1+4x0. 25HT; b) 1+4x0. 30HT; c) 1+4x0. 35HT

According to the results of modeling the twist, it can be seen that a larger wire diameter allows for smaller wire displacements in the metal cord structure during the twist due to the greater rigidity of the wire rod. However, even though the wires are displaced, the structure remains tight when twisted. At the length corresponding to about 35% of the twist pitch, there is a transition from a symmetrical section to an unbalanced one, which shifts the center of gravity of the section by an average of 28%. This can affect the distribution of the mass of the metal cord in the rubber web during its reinforcement, as well as the processes of twisting the metal cord itself. With such an unbalanced arrangement of wires, an excessive tension force will be exerted on the core.

A model is constructed to simulate the stretching of a metal cord to complete rupture of the entire metal cord structure. The destruction of the material obeys the classical laws of plastic flow of the material. The results of modeling the breakage of metal cord are shown in Figure 2.

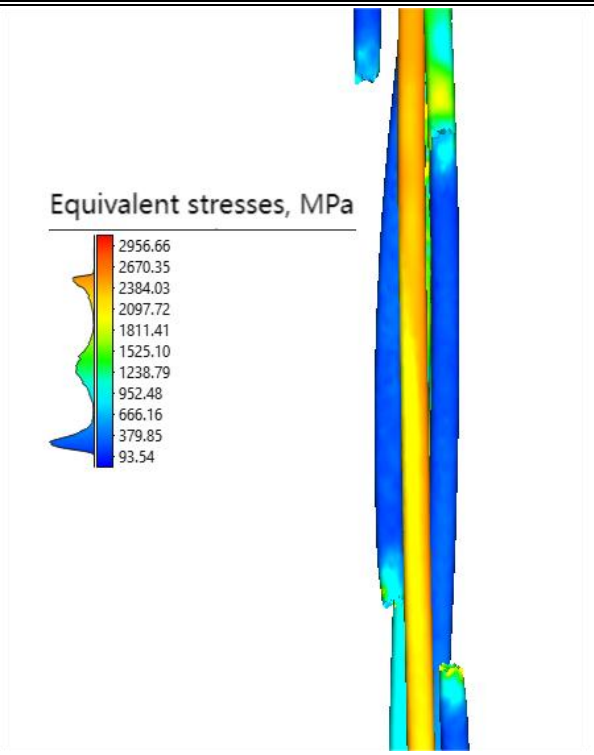


Fig. 2 Results of modeling of metal cord breakage

As can be seen from the model, the fracture obeys the classical principles of plastic deformation of the material. Because of the small iteration step, the simulation shows the formation of a neck and the moment of rupture, which is simulated by dividing the finite element grid. At a stretching rate of 1 mm/s, the formation and destruction of the neck takes an average of 0.2 seconds.

Similar models of metal cord stretching were constructed, but using a different law of material damage – Cocroft-Latham and Lemaitre [2, 3].The results of material destruction in these models show inadequate behavior of the wire under tension, showing a relative elongation of the wire in the range of 4.5-5%, which is approximately 1.85 times higher than the actual mechanical properties of steel 80.

The stretching diagram of a multilayer metal cord is shown in Figure 3.

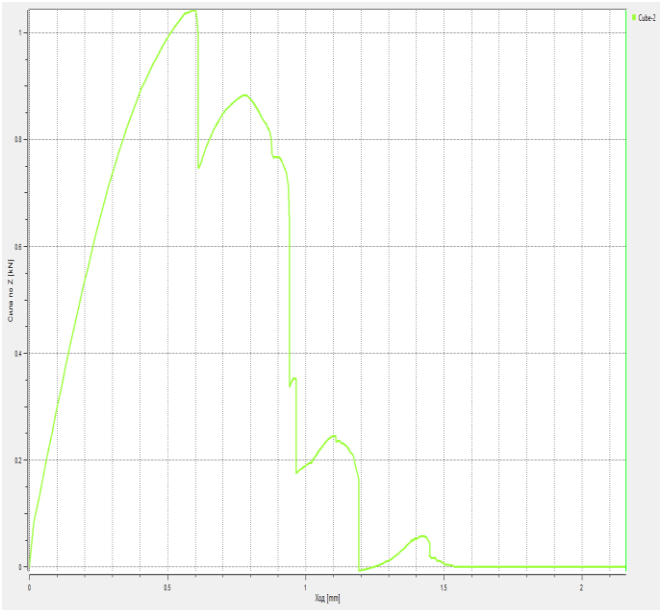


Fig. 3 Metal cord stretching diagram

The tensile diagram of a multi-layer metal cord shows the zones of increasing the breaking force during the destruction of wires.

This is due to the redistribution of loads on the wires in the structure due to the transverse displacement of the wires. First of all, the wire farthest from the center of mass of the cross-section of the metal cord is torn. The remaining wires continue to resist plastic deformation during a significant movement (0.5-0.6 mm). Subsequently, the break occurs almost simultaneously for the remaining wires. Last of all, the wire of the first layer breaks due to a smaller torsional deformation during twisting. In general, the aggregate strength of the studied metal cord is 8-10% less than the tensile strength of wires.

When the diameter of the wires increases, the stiffness of the wire rods is higher. As a result, more stable contact points of wires in the metal cord structure are formed during twisting. When such a structure is deformed, the destruction pattern is more predictable and uniform. Breaks are formed in approximately one zone, which is no more than 10% of the metal cord pitch.

Thus, a possible way to increase the aggregate strength of the metal cord can be to twist the metal cord with a large number of wires of the second layer and a core of one wire, as well as increase the diameter of the wires for more stable contact of the wires in the metal cord structure.

In addition, numerical models of stranding of multilayer types of metal cord of the following structures are constructed: 1+3x0. 25 HT, 1+3x0. 30 HT, 1+3x0. 35 HT, 1+4x0. 25 HT, 1+4x0. 30 HT, 1+4x0. 35 HT, 1+5x0. 25 HT, 1+5x0. 30 HT, 1+5x0. 35 HT. The basic parameters of the model are similar to a single-layer metal cord. The number of finite elements for each wire is at least 80,000. After modeling the twist and obtaining the initial level of wire position in the structure, as well as the initial level of equivalent residual stresses, the corresponding models of metal cord rupture were constructed.

As a result of numerical tests, the values of stresses and deformations for the moments of wire destruction in the metal cord structure up to complete destruction are determined. The results are shown in Figure 4 as a diagram.

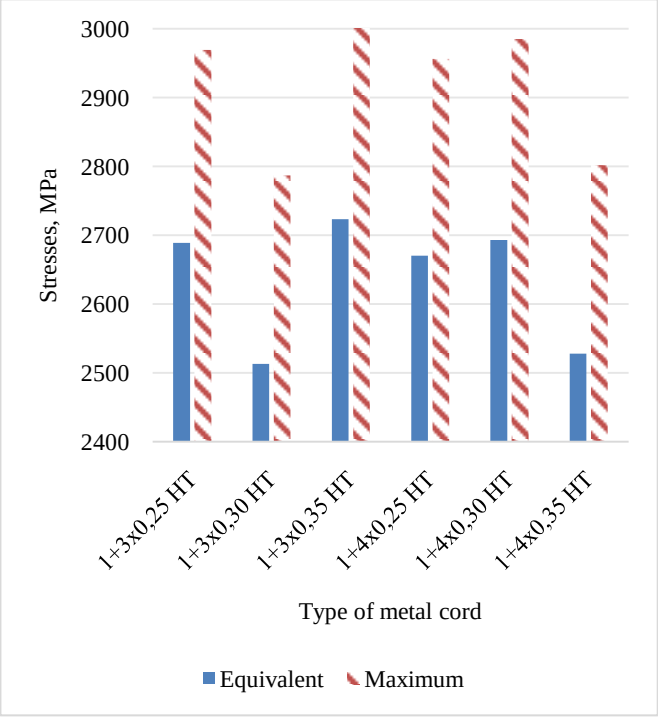


Fig. 4 Metal cord break stresses

Based on the simulation results, the dependences of the stress value during the destruction of the metal cord on the wire diameter for various metal cord structures are obtained.

For a metal cord of the 1+3 construction, the dependency looks like this:

$$\sigma = 77200d^2 - 45980d + 9359 \quad (1)$$

For a metal cord of the 1+4 construction, the dependency looks like this:

$$\sigma = -37600d^2 + 21140d - 265 \quad (2)$$

where σ – equivalent stresses at the moment of wire break, MPa;
d – wire diameter.

The analysis shows that with an increase in the diameter of the wires, there is no significant increase in the fracture stresses. These stresses correspond to the strength class of the metal cord. The exception is metal cords of the 1+4x0. 35 HT and 1+3x0. 30 HT designs, in which the twisting process led to a shift of the wires to a non-equilibrium state with a distortion of the shape of the bulk spiral. Such defects in the twist can be prevented by increasing the tension during the twist. The pattern of contact interaction of the wires of the second layer in such a design shows restrictions onthe movement of the wires in the tangential direction, which leads to increased (by 12-15%) torsional deformation. At the same time, the equivalent deformation remains unchanged for such a structure. The difference between the maximum voltage and the equivalent voltage at which the metal cord wires break was on average 10%.

References

1. Shrot, Aviral, and Martin Bäker. "Determination of Johnson–Cook parameters from machining simulations." *Computational Materials Science* 52.1 (2012): 298-304.
2. Wójcik, Łukasz, and Zbigniew Pater. "Comparison analysis of cockroft–latham criterion values of commercial plasticine and c45 steel." *acta mechanica et automatica* 12.4 (2018).
3. Lemaitre, Jean. "Coupled elasto-plasticity and damage constitutive equations." *Computer methods in applied mechanics and engineering* 51.1-3 (1985): 31-49.

Microstructural and Mechanical Performance of SiO_2-Reinforced Nickel-Based Nanocomposite Coatings

Regita Bendikiene[1,*], Antanas Ciuplys[1], Deyan Veselinov[2], Hristo Skulev[2]
Kaunas University of Technology, Lithuania[1]
Institute of Metal Science, equipment, and technologies with Center for Hydro- and Aerodynamics
"Acad. A. Balevski" at the Bulgarian Academy of Sciences, Varna, Bulgaria[2]
regita.bendikiene@ktu.lt

Abstract: *Nickel-based nanocomposite coatings reinforced with silicon dioxide (SiO_2) nanoparticles are attracting increasing interest in advanced marine applications due to their superior mechanical properties and resistance to surface wear. In this study, selective Ni-SiO_2 nanocomposite coatings were prepared and investigated to determine the relationship between microstructure, composition, and mechanical properties. The microstructure of the coatings was investigated using scanning electron microscopy (SEM). The analysis showed that the matrix is fine-grained and relatively homogeneous, containing well-dispersed SiO_2 nanoparticles at an amount corresponding to the optimal reinforcement level. Energy-dispersive X-ray spectroscopy (EDS) analysis confirmed that silicon oxide had been successfully incorporated into the nickel matrix and was uniformly distributed within it, and no significant signs of agglomeration were observed in the most effective compositions. Mechanical properties were evaluated by scratch tests to assess the coating's adhesion and resistance to mechanical damage. The results showed that SiO_2 -reinforced coatings exhibit significantly higher scratch resistance and higher critical load values. This improvement is attributed to dispersive strengthening, grain refinement, and the barrier effect created by hard ceramic nanoparticles, which together inhibit plastic deformation and crack propagation. In summary, the results of the study demonstrate the potential of Ni-SiO_2 nanocomposite coatings as durable protective solutions in marine environments, where resistance to mechanical wear and surface damage is particularly important. The study provides insights into how to adjust the microstructure and reinforcement distribution to improve the coating's performance characteristics.*

Keywords*: Ni-SiO_2 NANOCOMPOSITE COATINGS, SILICON DIOXIDE NANOPARTICLES, LASER SINTERING, NANOPARTICLE REINFORCEMENT.*

1. Introduction

The maritime industry is a key component of the global economy: it accounts for more than 80% of global trade in goods. It supports key oil, gas and renewable energy extraction processes [1]. However, the components used in this sector, from ship hulls and propulsion systems to offshore platform equipment, are exposed to extremely harsh operating conditions. Constant exposure to salt water, high humidity, temperature fluctuations and abrasive particles accelerates wear and corrosion, which greatly affects the performance and service life of critical systems. This requires the development and implementation of advanced security technologies to ensure the durability and reliability of marine equipment [2]. Corrosion remains one of the most pressing problems in the marine industry. According to estimates by the National Association of Corrosion Engineers, corrosion-related economic losses in this sector amount to 3% of global gross domestic product. These losses include direct component replacement costs as well as indirect costs resulting from equipment downtime, reduced operational efficiency, and increased risk of environmental incidents [3]. Wear is equally important, especially for moving components such as shafts, bearings and screws, which operate under high mechanical loads and are exposed to abrasive particles. The wear and tear of these parts not only increases maintenance requirements but also leads to higher fuel consumption, lower energy efficiency, and higher greenhouse gas emissions, thus requiring effective solutions [4], [5]. Protective coatings are essential to mitigate these challenges as they improve the durability and functionality of materials in marine environments. The most commonly used coatings are epoxy, polyurethane, ceramic and metal coatings. Despite their widespread use, each type has limitations that require further innovation [2]. Epoxy coatings are favoured for their excellent adhesion, water resistance, and chemical resistance, making them suitable for ship hulls, offshore platforms, and pipelines. However, over time, especially when exposed to UV rays, these coatings become brittle and can crack and peel. Furthermore, their effectiveness depends heavily on proper surface preparation and application, and improper methods reduce their protective capabilities [6]. Polyurethane coatings offer excellent UV resistance and a durable, glossy finish, making them ideal for use on the surface and above the waterline. However, they are less resistant to prolonged immersion in water and can degrade when exposed to aggressive marine chemicals. Furthermore, their curing process requires strict control of environmental conditions such as humidity and temperature, which complicates their application [7]. Ceramic coatings have the properties of hardness, wear resistance, and high temperature resistance, making them suitable for marine components such as propellers and shafts. However, their brittleness makes them prone to cracking under mechanical stress, and their application often requires advanced technology, which increases costs and limits their practicality for large-scale structures [2]. Metallic coatings, such as zinc and aluminium-based systems, provide protective cathodic protection to the underlying metals. Although effective, these coatings are susceptible to erosion in abrasive environments and require frequent recoating. Their effectiveness may also be reduced in areas subject to high mechanical stress or biological contamination [8]. A common drawback of many protective coatings is their environmental impact. Traditional coatings often contain volatile organic compounds (VOCs) and heavy metals, which can leach into the marine environment during degradation and pose a threat to aquatic ecosystems. Maintenance and recoating processes generate additional hazardous waste, and coatings that are prone to degradation or failure increase the risk of corrosion and structural instability, increasing long-term costs and environmental risks. New technologies, such as eco- and nanocomposite coatings, aim to address these challenges by offering improved performance and a smaller ecological footprint. However, these innovative solutions often involve higher initial costs and require specialised knowledge for their application [9]. This research aims to overcome these challenges by developing and evaluating advanced nickel-based nanocomposite coatings reinforced with silicon oxide (SiO_2) particles. These selectively deposited coatings aim to combine the improved mechanical and corrosion properties of nickel with the enhanced wear resistance provided by the SiO_2 particles. Advanced characterisation techniques will be used to investigate the microstructure, adhesion and performance of coatings under simulated marine conditions. The research will prioritise the ability of coatings to withstand the dual stresses of corrosion and abrasion, ensuring their suitability for critical marine applications such as ship components, offshore platforms and subsea systems.

2. Materials and Methods

The substrate material used was martensitic stainless steel 1.4021, also known as X20Cr13 (EN 10088). The substrate plates were supplied by CHIRMED (Poland); with dimensions 20×60×3 mm, and the selectively plated surface area was 20×25 mm. Since the substrate material is primarily used as a base

for coating deposition, its role in the study was limited to the preparation and surface treatment stages. The substrate surface was not subjected for mechanically treatment by grinding/polishing before selective plating. It was used as received. The plated area was masked, and electrochemical surface preparation measures were performed, including electrochemical cleaning, electrochemical etching, and activation of the masked surface. After activation, a nickel interlayer approximately 1 μm thick was deposited by selective plating. This bonding layer was applied to improve the adhesion strength of the subsequent coating and to act as a hydrogen and oxidation barrier. Nickel-based SIFCO Ni 2080 electrolyte was used to deposit the Ni-SiO_2 nanocomposite coating. The electrolyte had a pH of 2.3 and consisted of 20 wt% nickel sulfate, 10 wt% nickel formate, 10 wt% citric acid, 1 wt% aluminium sulfate, and deionised water. To prepare the nanocomposite plating solution, 2 wt% SiO_2 nanopowder with an average particle size of 10 nm was added to the nickel electrolyte. The suspension was dispersed by ultrasonication for 15 minutes before precipitation. During the selective platting process, the electrolyte was continuously stirred with a magnetic stirrer to maintain a stable dispersion of SiO_2 nanoparticles. Ni-SiO_2 nanocomposite coatings were deposited by a selective method. The prepared and activated substrate served as the cathode, and the coating brush served as the anode. During deposition, an electrolyte-saturated brush was moved across the masked substrate area at a speed of 15 m/min. The applied plating voltage was maintained in the range of 6-10 V. After deposition, the coated samples were rinsed with deionised water and dried.

The coating thickness was measured using a CEM DT-156 coating thickness gauge operating on the principle of magnetic induction. Its measuring range is from 0 to 1,250 μm, with a guaranteed reading error of 3% ± 1 μm and an accuracy of 0.1 μm. The probe creates a magnetic field, and the thicker the coating, the weaker the probe "detects" the ferromagnetic substrate; thus, the layer thickness is calculated from the change in the measured magnetic resistance.

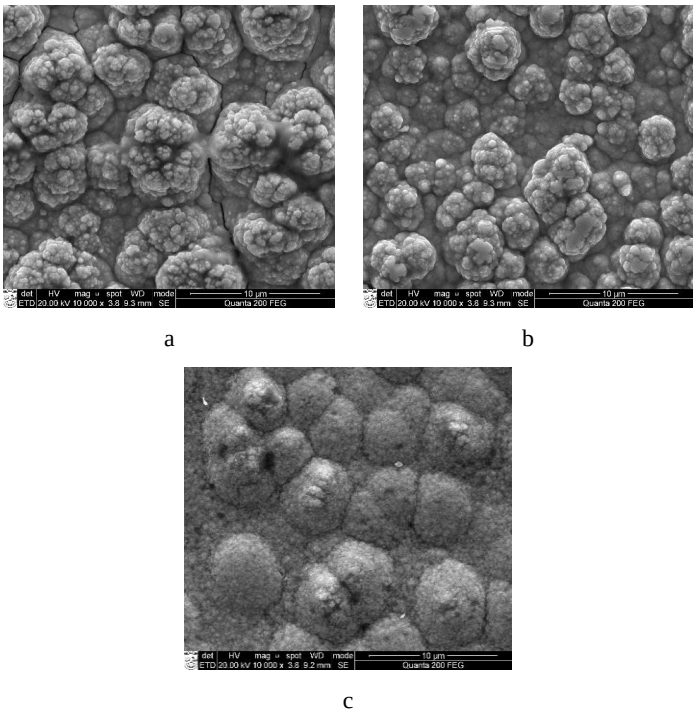
Microstructural analysis of the samples was performed using an FEI Quanta 200 FEG scanning electron microscope (SEM) equipped with a field emission generator (FEG). The microscope was operated under high vacuum to obtain high-resolution images of the sample surface. Before analysis, the samples were prepared using standard metallographic procedures, including cutting, casting, grinding, and polishing.

The elemental composition was determined using an energy dispersive X-ray spectroscopy (EDS) system integrated with a SEM (Bruker XFlash 4030). EDS analysis was performed to determine the chemical composition of the sample, assess the distribution of reinforcing particles (e.g. SiO_2), and detect any impurities or interfacial diffusion. Spectra were collected at random locations using an accelerating voltage of 15 kV to ensure sufficient excitation of characteristic X-rays.

Elemental distribution maps were created using the EDS mapping mode. This allowed us to see the distribution of chemical elements (Al, C, Su, Fe, Ni, Si, O) in the corresponding areas of the studied coatings. The results of EDS mapping allowed us to observe the penetration of SiO_2 particles into the metal substrate, revealed the structural uniformity of the coating, and highlighted the distribution and accumulation of chemical elements.

3. Experimental

SEM and EDS methods were used to study the distribution of SiO_2 nanoparticles in Ni-2%SiO_2 composite coatings and their morphology. SEM images of "Coating 1", "Coating 2", and "Coating 3" show a nodular morphology characteristic of electrochemically deposited coatings on a nickel substrate; however, there are noticeable differences in surface uniformity and density. The "Coating 1" samples exhibit a relatively uneven surface with irregularly shaped protrusions and areas of lower density, which confirms unstable growth conditions (Fig. 1 a).

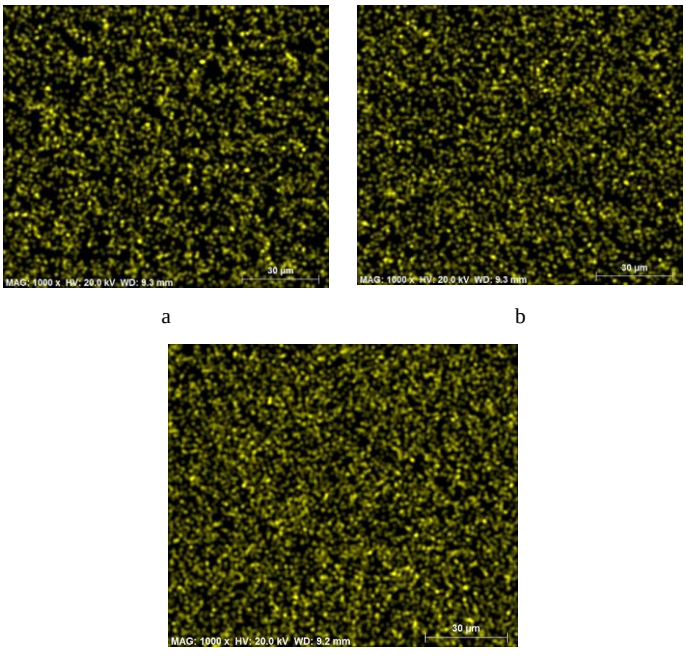


a b c

Fig. 1 *Surface morphology: a – Coating 1; b – Coating 2; c – Coating 3.*

The "Coating 2" exhibits a significantly more uniform nodule structure, characterised by a smaller variation in the range of nodule sizes and a more compact, uniform surface structure. All of this indicates that the conditions for vegetation growth are more stable and that the vegetation density is higher (Fig. 1 b). A nodular morphology is also observed in the "Coating 3"; however, compared to the "Coating 2", its structure is noticeably coarser and less uniform (Fig. 1 c). The surface is characterised by larger nodules, lower density, and localised irregularities.

The SI map, which shows the localised silicon deposits and the uneven distribution of particles (Fig. 2 a), confirms the unstable growth conditions in the "Coating 1".



a b c

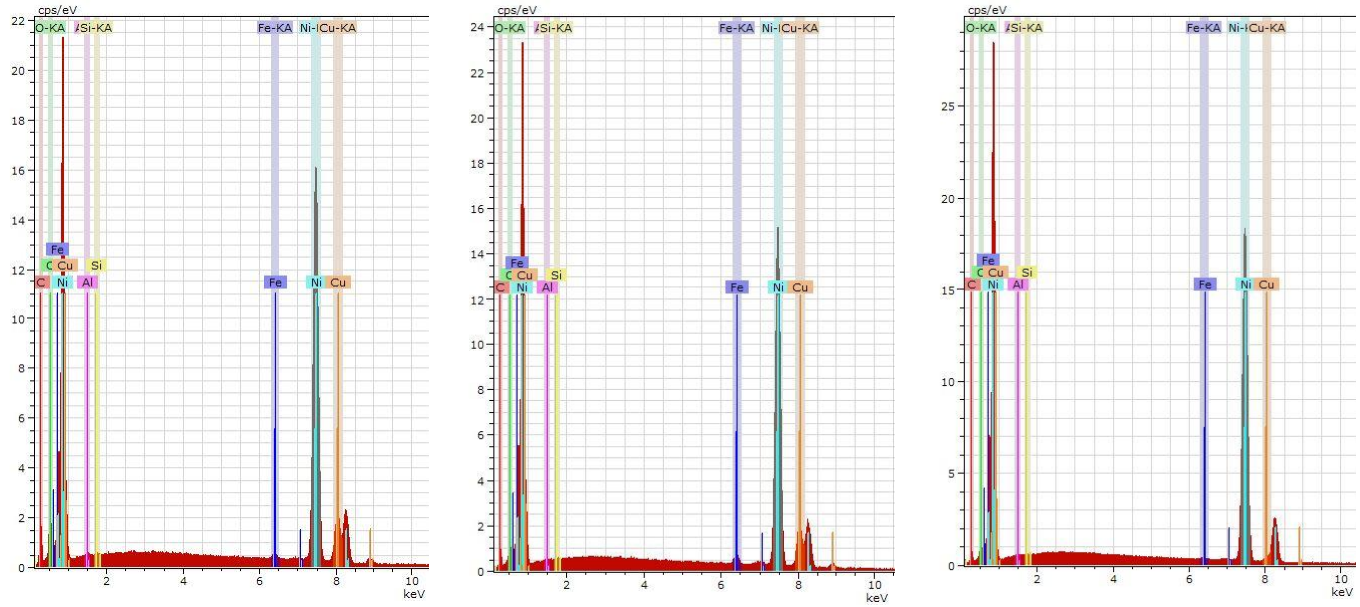
Fig. 2 *SI mapping: a – Coating 1; b – Coating 2; c – Coating 3.*

The corresponding silicon (Si) distribution map of "Coating 2" (Fig. 2 b), reveals a uniform and finely dispersed silicon distribution, indicating effective nanoparticle incorporation and increased coating density.

Visible microcracks and partially flat areas indicate the presence of internal stresses and less controlled growth dynamics in the "Coating 3". These characteristics indicate a reduction in the structural uniformity and density of the coating. This is associated with a less homogeneous distribution of silicon, suggesting that uneven particle penetration and local agglomeration contributed to structural inhomogeneity and the formation of internal stresses (Fig. 2 c).

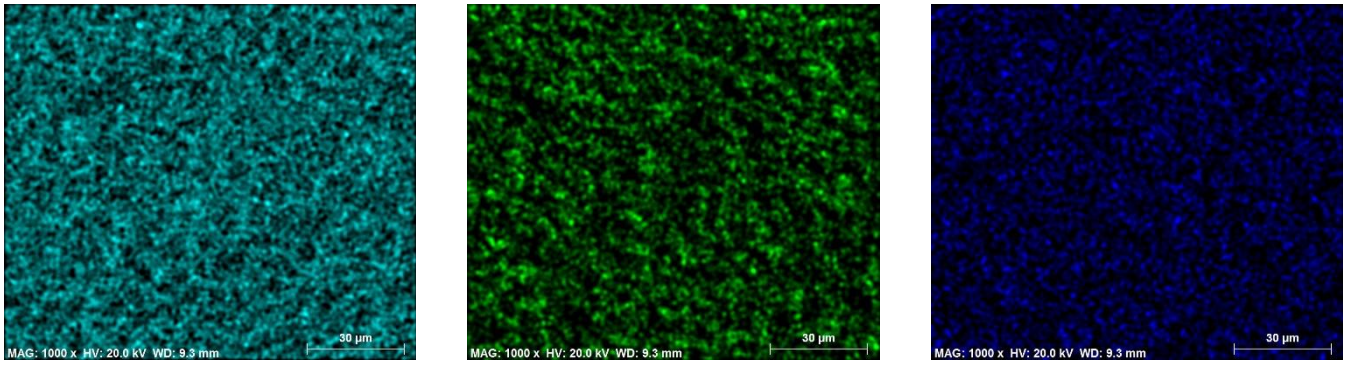
The EDS spectra confirm that the matrix consists of nickel; signals for silicon and oxygen were also detected, confirming the presence of SiO_2 nanoparticles (Fig. 3). The relatively low intensity of the Si peak indicates that the amount of the nanoparticle reinforcement phase is small (2 wt.%) and that the particles are small. The Fe signals detected in the spectra are attributed to the 1.4021 stainless steel matrix; they arise from the interaction of the electron beam with the material under the applied acceleration voltage. Furthermore, the presence of copper is not related to the composition of the coating and is most likely due to secondary factors associated with the brush electroplating process.

In summary, the results of the SEM and EDS analyses indicate that "Coating 2" exhibited the most favourable balance between coating growth and nanoparticle incorporation, resulting in the densest and most structurally homogeneous coating, whereas "Coating 1" and "Coating 3" exhibited greater heterogeneity associated with a less controlled particle distribution.



a b c

Fig. 3 *EDS spectra: a – Coating 1; b – Coating 2; c – Coating 3.*



a b c

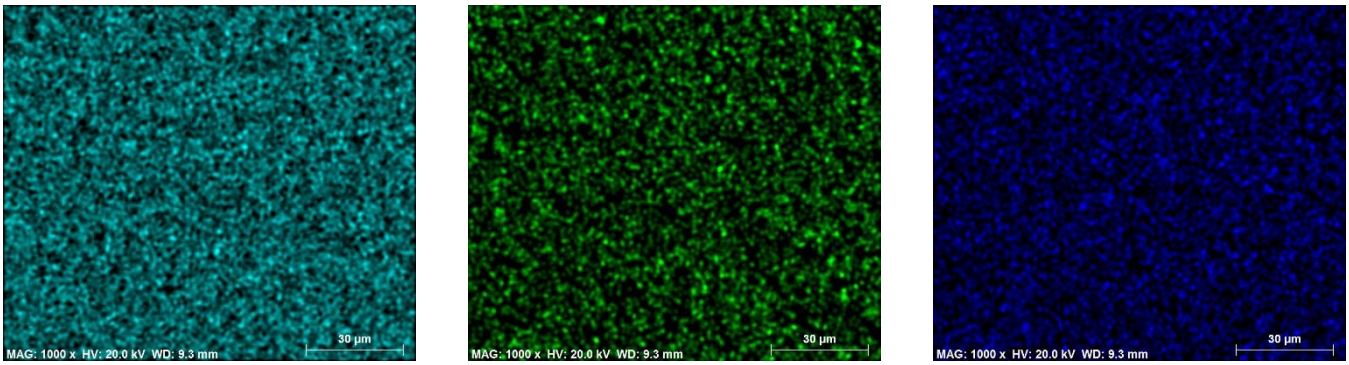
Fig. 4 *"Coating 1". Elemental map of: a – nickel map; b – oxygen map; c – iron map.*

The distribution map of the elements in the "Coating 1" shows a continuous but locally heterogeneous Ni matrix (Fig. 4 a), which is consistent with the heterogeneous morphology of the nodules observed in the SEM images (Fig. 1 a).

The Si and corresponding oxygen (O) signals confirm the presence of SiO_2 nanoparticles; however, their distribution is uneven, indicating partial agglomeration. The O map (Fig. 4 b) shows a slightly more dispersed distribution compared to Si, which confirms that slight surface oxidation also contributes to this. The Fe signal is clearly visible (Fig. 4 c) throughout the study area, which clearly indicates the influence of the substrate, caused by limited coverage density or reduced thickness in certain areas. These results confirm once again that the microstructure of the first layer is not homogeneous, the particles are distributed unevenly, and the surface is not fully compacted.

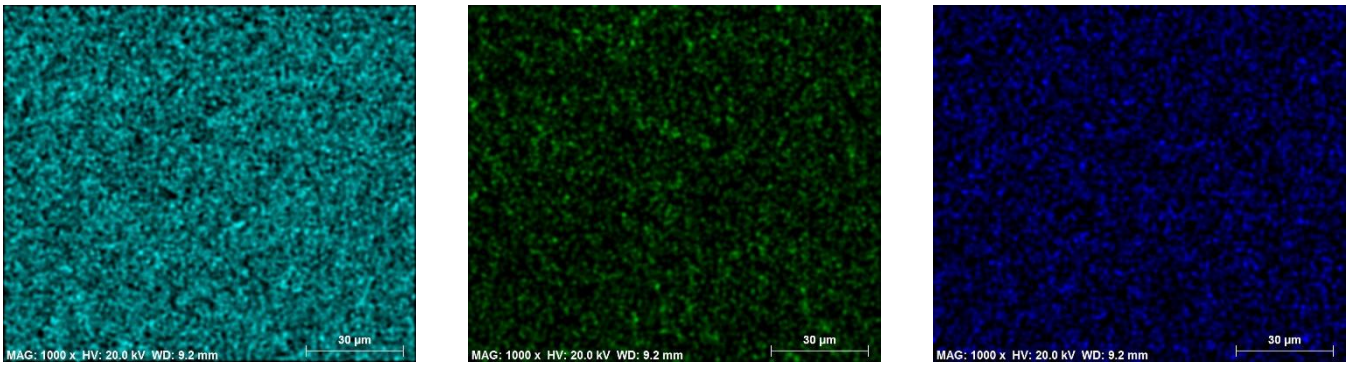
The distribution map of the "Coating 2" shows that a highly homogeneous and continuous Ni matrix has formed (Fig. 5 a), which confirms stable coating growth and greater structural integrity compared to the first coating. The distribution of silicon (Si) and the corresponding oxygen (O) on the surface (Fig. 5 b) is extremely fine-grained and homogeneous, which confirms that the SiO_2 nanoparticles penetrate effectively without forming distinct clusters. Unlike in the "Coating 1", the Fe signal here is significantly weaker and more diffuse (Fig. 5 c), which confirms the

limited influence of the substrate and suggests that the coating is denser and more uniform.



a b c

Fig. 5 *"Coating 2". Elemental map of: a – nickel map; b – oxygen map; c – iron map.*



a b c

Fig. 6 *"Coating 3". Elemental map of: a – nickel map; b – oxygen map; c – iron map.*

All elements are evenly distributed, which is consistent with the refined morphology of the nodules observed in the SEM images, confirming that "Coating 2" has a more homogeneous microstructure and higher coating density compared to "Coating 1".

The Ni distribution map of "Coating 3" shows a continuous Ni-rich matrix (Fig. 6 a); however, it appears slightly less regular than in "Coating 2", with minor local variations in intensity that correspond to the coarser and less compact surface morphology observed by SEM (Fig. 1 c). The oxygen distribution map is visible across the entire surface (Fig. 6 b), confirming the presence of an oxide-containing dispersed phase; however, its distribution appears slightly less uniform than in the "Coating 2" and more closely resembles a somewhat disordered particle arrangement. Meanwhile, the Fe map (Fig. 6 c) is fainter than that of the first layer, indicating that the upper layer still covers the bedrock fairly well, although it appears slightly lighter than the densest parts of the second layer. This confirms the earlier findings that, in terms of the influence of the substrate, "Coating 3" is not as defective as "Coating 1", but structurally it is less homogeneous and less dense than "Coating 2".

4. Conclusions

Based on a comprehensive analysis of all the studies conducted, namely, SEM observations, elemental distribution maps, and EDS spectra, clear qualitative differences are evident in the microstructure of the Ni-SiO_2 nanocomposite coatings obtained under different deposition conditions. The "Coating 1", plated at a voltage of 4 V, exhibits the most heterogeneous structure, characterised by irregular node morphology, uneven silicon distribution, and the strongest iron signal, indicating a partial substrate effect and a very low film density. Meanwhile, the "Coating 2", plated using a higher voltage (8–10 V), exhibits a highly homogeneous and densely deposited nodular surface characterised by an even distribution of silicon, a continuous nickel matrix, and the weakest iron signal, which confirms better nanoparticle penetration and better coating compaction. The "Coating 3", plated at a voltage of 4 V and a shorter time (1 min), also forms a uniform coating on the substrate surface; however, its surface is rougher; furthermore, the presence of microcracks and a less uniform distribution of Si indicate insufficient growth and lower structural stability compared to "Coating 2". The Fe signal in the "Coating 3 is weaker than in the "Coating 1", which confirms the reduced influence of the substrate; furthermore, the shorter curing time limits the coating thickness and uniformity. To summarise the results obtained, it can be concluded that increasing the deposition voltage to 6–10 V results in more uniform particle penetration and the formation of a more compact layer, whereas a lower voltage and shorter deposition time lead to a non-uniform and less stable microstructure.

Acknowledgments

This research was supported by the Lithuanian Academy of Sciences and the Bulgarian Academy of Sciences within the framework of the bilateral research project "Design and performance evaluation of selective nickel-based nanocomposite coatings reinforced with silicon oxide for advanced marine applications".

5. References

1. The Economist Group, "Global Maritime Trends 2050 | LR." Accessed: Jan. 06, 2025. [Online]. Available: https://www.lr.org/en/knowledge/research/global-maritime-trends-research-programme/

2. H. Liang et al., "Technologies in Marine Antifouling and Anti-Corrosion Coatings: A Comprehensive Review," vol. 14, p. 1487, 2024, doi: 10.3390/coatings14121487.
3. E. Bowman, N. Thompson, D. Gl, O. Moghissi, M. Gould, and J. Payer, "International Measures of Prevention, Application, and Economics of Corrosion Technologies Study," Mar. 2016.
4. C. Zhao, L. Ying, C. Nie, T. Zhu, R. Tang, and R. Liu, "Investigation of the Corrosion–Wear Interaction Behavior of 8Cr4Mo4V Bearing Steel at Various Corrosion Intervals," Coatings 2024, Vol. 14, Page 1245, vol. 14, no. 10, p. 1245, Sep. 2024, doi: 10.3390/COATINGS14101245.
5. J. Liu et al., "Wear Characteristics Caused by Ti3AlC2 Particles under Impact-Sliding Conditions in Marine Engine," Journal of Marine Science and Engineering 2024, Vol. 12, Page 1777, vol. 12, no. 10, p. 1777, Oct. 2024, doi: 10.3390/JMSE12101777.
6. S. Verma, S. Mohanty, and S. K. Nayak, "A review on protective polymeric coatings for marine applications," J Coat Technol Res, vol. 16, no. 2, pp. 307–338, Mar. 2019, doi: 10.1007/s11998-018-00174-2.
7. A. Pistone, C. Scolaro, and A. Visco, "Mechanical Properties of Protective Coatings against Marine Fouling: A Review," Polymers (Basel), vol. 13, no. 2, p. 173, Jan. 2021, doi: 10.3390/polym13020173.
8. B. Syrek-Gerstenkorn, S. Paul, and A. J. Davenport, "Sacrificial Thermally Sprayed Aluminium Coatings for Marine Environments: A Review," Coatings 2020, Vol. 10, Page 267, vol. 10, no. 3, p. 267, Mar. 2020, doi: 10.3390/COATINGS10030267.
9. M. S. Selim et al., "Advanced Bioinspired Superhydrophobic Marine Antifouling Coatings," Superhydrophobic Coating - Recent Advances in Theory and Applications, Sep. 2023, doi: 10.5772/INTECHOPEN.1002806.

Experiment preparation with Phase Changing Materials for industrial application

Veneta Yosifova, Milena Haralampieva, Posen Petrov
Institute of Information and Communication Technologies[1]
veneta.christova@iict.bas.bg, milena.haralampieva@iict.bas.bg, rosen.petrov@iict.bas.bg

Abstract: *This article summarizes the preliminary preparations for conducting experiments with phase change materials to determine their behavior during continuing heating and cooling processes. The goal is to summarize conclusions about the possibilities of using these materials in boilers and other water-heating tanks for industrial and domestic applications. The techniques, materials, and equipment that will be used are described, as well as the theoretical behavior of the materials that will be compared.*
Keywords*: ENERGY EFFICIENCY, PHASE-CHANGING MATERIALS, HOT WATER STORAGE, INTELIGENT SOLUTIONS*

1. Introduction

Achieving a highly efficient building that ensures optimal thermal comfort and quality of life brings enormous benefits in terms of return on investment, energy savings, longer service life, significantly improved productivity and comfort for residents, while also causing minimal impact on the surrounding environment. Regardless of whether it concerns single-family houses, public buildings, or industrial premises, all new buildings are built according to the new European requirements for energy efficiency. They require less pollution, cleaner air and, at the same time, a reduction of cost, especially from the use of energy for heating. For existing buildings, measures must be taken to increase their energy efficiency in all aspects of consumption - heating, ventilation, air conditioning, water supply, lighting, etc.

Studies show that a large proportion of European consumers still use water heaters for water heating, [1]. This is why new, efficient solutions for heating water that consume less energy are being developed. The problem with water heaters is that they heat a large amount of water that may not be used at a certain time. In this way, energy consumption is unjustified. Another disadvantage associated with the use of traditional boilers is the accumulation of limescale, which leads to a decrease in efficiency and the need for repairs. One of the options chosen by European households is tankless water heaters. They are compact and space saving. They supply hot water, with no preheating and waiting-time required. This also avoids running out of hot water during peak consumption in the morning or evening hours, when the consumption is higher. In countries with milder and warmer climates, they are also used for outdoor use. These water heating systems have a longer life, do not require complex maintenance and in long term prove to be effective. The possibilities for their integration into installations powered by renewable energy sources are also developing, which will further improve their energy efficiency, [2]. Unfortunately, tankless water heaters are only suitable for family houses with up to several households. They cannot be used in larger buildings such as industrial, agricultural and public, since the consumption of hot water is significantly higher and the purchase of a large number of these devices becomes unjustified.

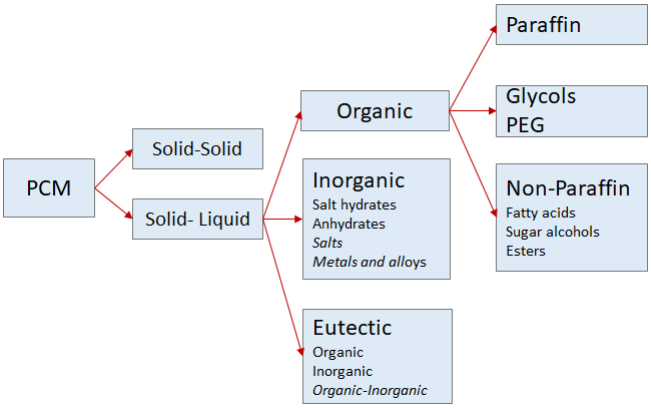
The phase change materials (PCM) store and release heat at the temperature at which it melts or solidifies. It can hold a large amount of thermal energy per unit volume because it relies on latent heat, which is greater than sensible heat. Latent heat can be used by solid-gas, solid-liquid, and liquid-gas transition states, with the solid-liquid transition being the most preferred because the volume doesn't change much.

The use of PCM for latent heat storage allows energy storage even with a small temperature difference if integrated into a hot water tank. This combination increases energy capacity and improves performance under specific load patterns, [3].

This article is related to a project for developing a water tank with an integrated phase change material into the construction to increase energy efficiency. The publication outlines the preliminary studies and prerequisites for conducting experiments with PCM to determine their real qualities and the possibilities for their use in boilers. Chapter 2 examines the essence of PCM and their application possibilities. Chapter 3 describes the preparation for conducting experiments with PCM. The last chapter draws conclusions about the conduct of the experiment and the expected results.

2. Application of Phase Change Materials

Phase Change Materials (PCMs) are an extremely suitable solution for the regulation of thermodynamic processes. This is because they store and release thermal energy when they change their state (from one phase to another). When this happens, they release a large amount of energy in the form of latent heat of fusion. In the opposite case, when heated, the material absorbs a large amount of energy and retains it. The types of PCM are mainly Solid-Solid and Solid-Liquid, and their subdivisions are described in Figure 1.



Фиг. 1 *Types of PCMs*

PCMs can be widely used in various industries due to their beneficial characteristics. Their most common applications are:

Construction – used as a component of materials for various surfaces – walls, floors, ceilings to maintain temperature, by absorbing heat during the day and returning it at night.

Energy storage from solar panels – on the same principle of absorbing and releasing heat, PCMs, such as Sodium sulfate decahydrate, help solar systems to be more efficient.

Refrigeration – refrigerators, refrigerating trucks and cold storages use these materials (e.g. mix of ammonium chloride and water) to ensure cold temperatures in emergency situations, such as power outages, technical malfunctions, etc.

Textiles – Paraffin wax is most often used for clothing that protects against extreme hot or cold temperatures.

Heat pumps – materials (paraffin-based PCMs or salt hydrates) store excess heat generated during the operation of the heat pump. When demand increases, the stored energy is released. The frequency of switching on and off is reduced, which helps save energy and extend the life of the compressor.

Table 1 summarizes the main advantages and disadvantages of working with phase change materials:

Table 1 *– PCMs Advantages and Disadvantages*

Advantages	Disadvantage
Energy efficiency	High price of some materials
Temperature control	The organic materials have low durability
Environment-friendly	Requires extensive research in the field

Given the potential of these materials, their research is essential for achieving high energy efficiency in the above-described industries, [4]. In water heaters, research and improvement of the use methodology are yet to be conducted, but the current results are promising, [5].

In one of the studies on the subject, the boiler system is used as the main heating unit through hot water, and the PCM-based waste heat recovery system is used as the air heating unit. In experiments conducted at 24-minute intervals, interesting conclusions have been made, proving the possibilities of achieving high energy efficiency (between 24% and 51%, depending on the state of the PCM) in building heating systems. The maximum efficiency of the PCM heat exchanger is about 13%, achieved around the time of the phase change, in which latent heat is obtained. This efficiency is an addition to the heating of the building with a boiler system. This is because the heat exchanger system supported by the PCM is used as a supplement to the building heating unit. The combination of PCM with the building heating unit shows that hybridization positively affects the system and, therefore, lower energy consumption may be possible thanks to the energy stored in the PCM, [6].

To achieve even higher energy efficiency, the combination with a renewable energy source is suitable. In another study, a PCM layer was integrated within a solar collector connected to a hot water tank system. In this way, hot water with a constant temperature close to the melting temperature of the PCM can be produced for a long period of operation. The results of the annual performance study of the system show that the production of hot water with a constant temperature throughout the year can be achieved with an appropriate choice of effective parameters. At high water flow rates through the system, multiple collectors can be used in a sequential configuration. By using two consecutive collectors, the system performance is increased by more than two times compared to that of a single solar collector, [7].

Several main economic advantages of using FPM in hot water heaters can be outlined. The first of these is that fewer boilers can cover the hot water demand, which in turn saves usable space. In addition, the integration of such a system allows energy to be consumed in evening peak tariff windows, when there is no high demand, and the stored heat to be released when needed, [8].

3. Experiment preparation

The experiment aims to investigate the behavior of three types of phase change materials (PCMs): paraffin, sodium thiosulfate pentahydrate ($Na_2S_2O_3 \cdot 5H_2O$), and sodium acetate trihydrate ($NaCH_3COO \cdot 3H_2O$), in order to select the most suitable material for use in a hot water heater (Figure 2). Their properties and characteristics will be subjected to real experiments and will be examined closely. The conclusions from the experiments performed will be useful in determining the material that will be used for a real water heating system, which will be the subject of further studies (Figure 3).



Fig. 2 *(Left to Right) Paraffin, Sodium thiosulfate pentahydrate and Sodium acetate trihydrate*

The properties of the selected materials are described in Table 2. They may vary depending on the quality and purity of the material. The selection of these materials is related to their good thermodynamic performance and their temperature compatibility with water heating vessels.

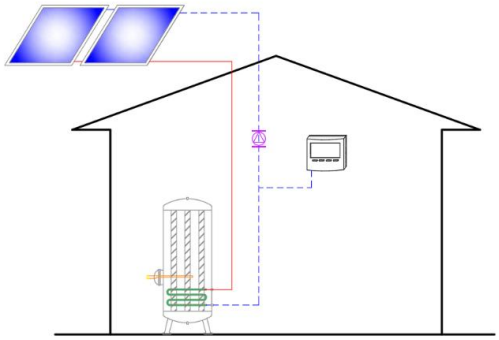


Fig. 3 *PCMs water tank with solar panel integration*

Table 2 *– PCMs Characteristics*

Material	Melting temperature T□ (°C)	Latent heat λ (kJ/kg)	Advantages	Disadvantages
Paraffin - Organic C_nH_{2n+2}	~55–58	150 – 210	Stable Safe No overcooling Non-corrosive	Low thermal conductivity Slower heat transfer
Sodium thiosulfate pentahydrate - Salt-hydrate $Na_2S_2O_3 \cdot 5H_2O$	~48	200 – 250	High density and thermal conductivity Good heat transfer Low cost	Super cooling Possible phase separation
Sodium acetate trihydrate - Salt-hydrate $NaCH_3COO \cdot 3H_2O$	~58	260 – 290	Very high thermal conductivity Suitable melting temperature Affordable	Need for thickeners/nucleators for stability

Paraffin is chemically inert, does not react with most building materials and has excellent resistance to repeated heating and cooling cycles, during which it does not overcool and its structure

does not separate. Salt hydrates are non-toxic and safe, their practical use is mainly in medicine. Although some salt hydrates show a tendency to phase separation or overcool, the selected materials are among the most stable in their group and this behavior can be controlled by appropriate engineering solutions, additives or optimization of the hot water tank. With the right choice of container for storing the material, the risk of corrosion is minimal, which allows for reliable long-term operation.

The experiment will observe the behavior of materials during heating and cooling, primarily in terms of changing their structure and the process of phase change with temperature, and their thermodynamic properties.

One of the reasons for choosing these materials is that they are widely available on the European market. They exist in various degrees of purity. Their price is relatively low compared to other PCMs with similar characteristics. Their application in the chemical, pharmaceutical, and food industries makes them widely available and maintains stable and competitive market prices, [9].

Regarding engineering compatibility and integration possibilities, the different phase transition mechanisms of organic and inorganic PCMs allow different combinations through which the properties of the materials complement each other – stability, high latent heat, and different temperature behavior. The selected materials can be encapsulated or integrated into modular systems that do not require complex technological modulations, thus reducing integration costs.

The experiment to test paraffin, $NaCH_3COO \cdot 3H_2O$ and $Na_2S_2O_3 \cdot 5H_2O$ is planned to be conducted in a laboratory environment, where their temperature behavior will be monitored under identical conditions (Figure 4).



***Fig 4**: Experimental setup*

The following equipment will be used:

- Glass flasks with the same geometry and volume;
- Electric heating plate with the ability to change the heating intensity;
- Thermographic camera for non-contact measurement and recording of the temperature in different areas of the set in real time. FLIR X6800sc MWIR (Figure 5) with a resolution of 640 × 512 and a temperature range: - 45°C to +600°C, from 250°C to 2000°C will be used;
- Thermometers for detecting temperature inside the material and ambient temperature;
- Scale for precise measurement of equal amounts of material. Equal portions of 250 ml of each material will be used to avoid errors caused by the amount of material;



***Fig 5**: Thermographic imaging with FLIR X6800sc MWIR*

- Precision microscope for monitoring corrosion processes. A modern Olympus BX53M microscope (Figure 6) is used, which has high-intensity White LED illumination with constant color temperature, versatile observation methods (brightfield, darkfield, DIC, polarization, MIX), and seamless integration with PRECiV software for digital imaging and reporting.

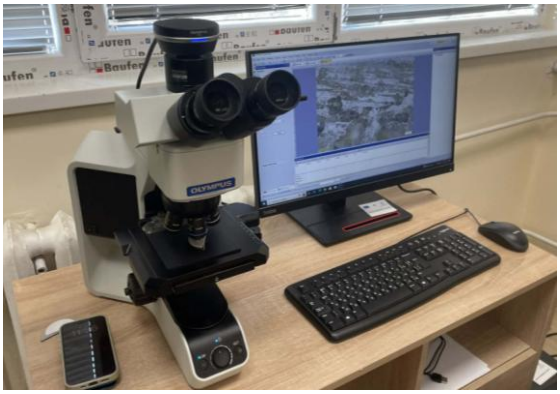


***Fig 6**: Olympus BX53M microscope setup*

The flasks are centrally located on the heating plate to ensure the most even heat transfer conditions. Maintaining a constant situation and heating conditions is extremely important for a reliable comparison of materials, since the charging/discharging behavior of PCM is highly sensitive to boundary conditions and heat transfer area. For this reason, the temperature must be constantly monitored.

Basic safety guidelines should be followed for each experiment to reduce the risks associated with chemicals and ensure the safety of the researchers. Safety glasses, a lab coat, closed-toe shoes, and gloves appropriate for the specific chemicals being handled should be worn. The work area should be kept clean and flasks should be kept away from the body when mixing or diluting chemicals. Chemical materials should be disposed of in designated waste containers according to specific disposal instructions.Through the experimental setup thus established, the following processes will be observed:

1. Heating the materials from room temperature 22-24°C until their phase state changes (to about 75-80°C). Their physical state will be monitored and their temperatures recorded at regular intervals, recorded using a stopwatch.

2. Non-invasive (without intervention) cooling of the materials to convert them to their original physical state. Again, their physical state will be monitored and their

temperatures recorded at regular intervals of time, detected by a stopwatch.

3. In addition to the heating and cooling processes (50-100 cycles expected), the development of corrosion in a metal element will be observed under a microscope to determine the interaction of materials with the surrounding systems in the heating container. Corrosion in such vessels is extremely dangerous because it can lead to the malfunction of the entire system. For this reason, techniques for preventing corrosion should be selected during the production of the product. This improves its life cycle and safety, [10].

4. Conclusion

In the search of intelligent solutions for water heating, one of the modern solutions stands out - the use of phase changing materials. In order to develop a water heating system with an integrated phase-change material to increase energy efficiency, the properties and behavior of the material must be studied in an environment resembling the real one. Through solid theoretical preparation and a number of experiments, conclusions will be drawn about the possibilities of using paraffin, $NaCH_3\ COO{\cdot}3H_2\ O$ and $Na_2\ S_2\ O_3\ {\cdot}5H_2\ O$. According to the results obtained, these experiments will show which of these materials will be most suitable for incorporation into a water heating system. Such a system, especially connected to a renewable energy source, would be extremely energy-efficient, since the PCM helps retain heat and thus the consumption of heating energy would decrease. The future of water heaters undoubtedly includes the use PCM, which requires their experimental study to obtain reliable results.

Acknowledgment

This research was conducted with the financial support of the Bulgarian National Science Fund under Grant No. КП-06-М87/6/09.07.2025

References

1. Pezzutto, S.; Croce, S.; Zambotti, S.; Kranzl, L.; Novelli, A.; Zambelli, P. Assessment of the Space Heating and Domestic Hot Water Market in Europe—Open Data and Results. Energies 2019, 12, 1760. https://doi.org/10.3390/en12091760
2. Eccotemp Europe, Why European Homes are Switching to Tankless Water Heating, April 2025, link (last accessed: 03.2026)
3. Luisa F. Cabeza, Manuel Ibáñez, Cristian Solé, Joan Roca, Miquel Nogués, Experimentation with a water tank including a PCM module, Solar Energy Materials and Solar Cells, Volume 90, Issue 9, 2006, Pages 1273-1282, ISSN 0927-0248, https://doi.org/10.1016/j.solmat.2005.08.002.
4. Thermtest Instruments TM, Understanding Phase Change Materials (PCM), December 2024, link (last accessed: 03.2026)
5. Balci OM, Ezan MA, Turhan KZ. A heat recovery unit with phase change material for combi-boilers. Energy Storage. 2019; 1:e81. https://doi.org/10.1002/est2.81
6. Hakan Caliskan, Habib Gurbuz, Yasin Sohret, Durukan Ates, Thermal analysis and assessment of phase change material utilization for heating applications in buildings: A modelling, Journal of Energy Storage, Volume 50, 2022, 104593, ISSN 2352-152X, https://doi.org/10.1016/j.est.2022.104593.
7. Vahid Madadi Avargani, Brian Norton, Amir Rahimi, Hajir Karimi, Integrating paraffin phase change material in the storage tank of a solar water heater to maintain a consistent hot water output temperature, Sustainable Energy Technologies and Assessments, Volume 47, 2021, 101350, ISSN 2213-1388, https://doi.org/10.1016/j.seta.2021.101350.
8. Mick McKeever, Validating the Performance of a Prototype Phase Change Material for a Thermal Energy Storage Tank, Connected to a Micro-CHP, SDAR Journal of Sustainable Design & Applied Research, Volume 3, Issue 1, Article 2, 2015
9. White, Mary Anne and Kahwaji, Samer and Noël, John A., Recent advances in phase change materials for thermal energy storage, Chem. Commun, 2024, Жол 60, Иссуе 13, пп 1690-1706, http://dx.doi.org/10.1039/D3CC06063B
10. R.S. Barot, Parth Patel, Avadh Patel, Amar Patel, Corrosion prevention and industrial economic analysis aspects for water heater, Materials Today: Proceedings, Volume 28, Part 3, 2020, pp1795-1800, ISSN 2214-7853, https://doi.org/10.1016/j.matpr.2020.05.196.

Synthesis of polyphase materials containing pseudowollastonite

Bojidar Jivov[1], Mihaela Aleksandrova[1], Vladimir Petkov[1], Marieta Gacheva[1]*, Mariela Dimitrova[2], Stancho Yordanov[1], Dimo Mihaylov[1]

[1]Bulgarian Academy of Sciences, Institute of Metal Science, Equipment and Technologies with Hydro- and Aerodynamics Centre "Acad. A. Balevski", 67 "Shipchenski prohod" Blvd., 1574 Sofia, Bulgaria, e-mail: mvgacheva@abv.bg
[2]Bulgarian Academy of Sciences, Institute of Electrochemistry and Energy Systems "Academician Evgeni Budevski", 1574 Sofia, Bulgaria

Abstract: *Based on waste biogenic calcium carbonate $CaCO_3$ and silicon dioxide SiO_2, polyphase materials with a predominant content of calcium silicate phases and a limited presence of silicon dioxide were synthesized in laboratory conditions. When preparing the experimental samples, solid-phase synthesis and thermal treatment modes with a maximum temperature of up to 1300°C were used. During the X-ray phase analysis of the obtained experimental samples, the presence of $Ca_3(SiO_3)_3$ pseudowollastonite (dominant phase) was registered, β-Ca_2SiO_4 and SiO_2 cristobalite. The main possibilities for further expedient modification of the used technological regimes are analyzed. The prospects for potential application of the synthesized phases for the preparation of various functional materials are considered. The study is consistent with modern trends in the use of technological approaches that allow the utilization of waste materials.*
Keywords: *CALCIUM SILICATE MATERIALS, PSEUDOWOLLASTONITE, DICALCIUM ORTHOSILICATE*

1. Introduction

A main direction in the development of modern materials science is the study of phase formation in various oxide systems in a wide concentration and temperature range [1]. Based on the established processes of phase formation, appropriate technological approaches have been developed for obtaining materials with different structural and operational characteristics [2-4].

Modern silicate technologies allow the production of a current assortment of traditional, standard and innovative products with successful market realization [5-9]. Industrial enterprises equipped with specialized facilities (tailored to the specifics of the technological methods used) have been built, ensuring the implementation of cost-effective production processes and obtaining materials with a certain phase composition and appropriate functionality [10,11].

In this aspect, calcium silicates are considered a particularly promising group of materials, for the production of which various technological methods have been developed [12,13]: high-temperature solid-phase synthesis, hydrothermal synthesis, sol-gel synthesis, precipitation and others. Materials obtained through high-temperature synthesis are characterized by a more distinct crystal structure and lower porosity when compared to products prepared through other technological methods (e.g. hydrothermal synthesis).

Calcium silicate materials combine a number of favorable characteristics [12-18]: good mechanical resistance, thermal insulation properties, moisture resistance, fire resistance, non-flammability, workability, relatively low weight, biocompatibility, recyclability, environmental friendliness, durability and a long service life.

Tricalcium silicate Ca_3SiO_5 (alite, $3CaO.SiO_2$ or C_3S according to CCN) and dicalcium orthosilicate β–Ca_2SiO_4 (belite, $2CaO.SiO_2$ or C_2S according to CCN) represent a significant part of the phase composition of Portland cement clinker and significantly determine its characteristics [19]. As functional fillers, calcium silicate phases are present in various product categories (plastics, rubber, paints, paper, etc.) [12]. Various modifications of calcium silicate biomaterials have been developed for use in implantology and dentistry [20]. Dicalcium orthosilicate (Ca_2SiO_4) is applicable in the food industry as an anti-caking agent [12].

Calcium silicate materials in the form of thermal insulation and refractory elements (plates, slabs, blocks and others) are foundactive use in modern residential, public and industrial construction [14-18]. The performance characteristics of the various products allow the implementation of modernenergy-efficient and environmentally friendly design solutions with a high level of safety. A standard approach is the construction of long-lasting thermal insulation, interior partitions, suspended ceilings and other structural and decorative interior elements, as well as cladding of fireplaces, wet rooms and building facades [15-17]. Wollastonite ($CaSiO_3$) is a full-fledged, environmentally friendly and safe alternative substitute for asbestos materials [14,15].

Calcium silicate materials are used for the construction of various fire protection structures in the energy, metallurgical, chemical, silicate and oil refining industries and other manufacturing sectors. In this aspect, an effective solution is the construction of fire protection barriers and the lining of high-temperature industrial facilities, chimneys, pipelines, various industrial equipment, installations, doors, walls, ceilings, beams, columns, shafts and metal structures [12,15].

During their normal operation, the materials do not emit toxic products andlimit the development of fungal cultures on the products.

The favorable performance characteristics of silicate products and their importance for various economic sectors are a prerequisite for the development of functional materials with the presence of silicate phases [15]. The synthesis of materials with a phase composition formed by the joint presence of various calcium silicate and other phases (combining their specific characteristics) allows the production of materials with diverse properties, adapted to specific application possibilities [21]. At the same time, a current environmental interest is the use of technological approaches that allow for the effective and cost-effective utilization of various waste raw materials, sustainable in the natural environment [22-25].

The main objective of the present work is to study the phase composition of experimental samples obtained by solid-phase synthesis based on waste biogenic carbonate raw material and silicon dioxide SiO_2.

2. Experimental procedures

When preparing the experimental samples, standard laboratory equipment was used: a precision balance model RSV 200-2 KERN, a Sartorius MSU225P analytical balance, a scale up to 10 kg, a porcelain ball mill with a working volume of 50 L (rotation speed up to 260 rev/min) and a set of grinding bodies, an "Astel" laboratory dryer, a set of standard laboratory sieves, an agate mortar, corundum crucibles, laboratory glass baths and others.

The thermal treatment of the experimental compositions was carried out in a laboratory programmable muffle furnace (with Kanthal Super heating elements), equipped with an electronic programmer, allowing controlled change and maintenance of the temperature regime parameters: rate of temperature increase and decrease, isothermal holds, and others.

In the preparation of the batch compositions, waste biogenic calcium carbonate $CaCO_3$ and SiO_2 (Fused silica, Dupre Minerals Limited) were used. As a promising raw material for introducing CaO into the reaction system, waste shells (from marine organisms) formed from calcium carbonate $CaCO_3$ were used. The provided amount of waste shells was subjected to mechanical processing by primary crushing and wet grinding for 24 h and drying treatment (at 90°C for 3 h).

The required quantities of the obtained fraction $CaCO_3$ (after grinding) and SiO_2 were weighed, mixed and subjected to joint wet grinding in a laboratory mill (for 3 h). After completion of the

milling process, the compositions were dried (at 90°C for 3 h), finally homogenized in an agate mortar and sieved (through a 0.315 mm sieve) to a suitable fractional composition. The prepared batch compositions were placed in corundum crucibles (in an amount of 15 g) and introduced into the working space of the furnace before the start of the thermal treatment.

The thermal treatment of the compositions was carried out in an air environment by applying two temperature regimes with three isothermal holds and different maximum temperatures:

- first temperature regime 900°C (30 min), 950°C (30 min) and maximum temperature 1250°C (1 h);
- second temperature mode 900°C (30 min), 950°C (30 min) and maximum temperature 1300°C (1 h).

After completion of the heat treatment, the samples were subjected to free cooling (in the furnace space) to room temperature.

The experimental samples were studied with a PANalytical Aeris X-ray diffractometer with Cu-Kα radiation (λ=1.5406Å) and θ-θ Bragg-Brentano geometry. The initial X-ray diffraction patterns were obtained at room temperature, constant scanning speed and reflection angle 2θ in the range 7-90° with a step of 0.02°. The obtained diffractograms were interpreted using the PDF 2-2022 database, ICDD.

An Epsilon 1 spectrometer (Panalytical) with an Ag X-ray tube at a voltage of 50 kV and a maximum power of 10 W was used to determine the elemental composition.

3. Results and Discussion

Based on waste biogenic calcium carbonate $CaCO_3$ and SiO_2, polyphase materials with a predominant content of calcium silicate phases and a limited presence of silicon dioxide were obtained in laboratory conditions. In preparing the experimental samples, solid-phase synthesis was used, carried out through two heat treatment regimes, characterized by the application of two intermediate isothermal holds (at 900°C for 30 min and 950°C for 30 min), but with different maximum final temperatures at 1250°C and 1300°C for 1 h (Figure 1).

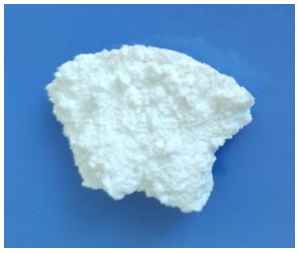


Fig 1. *Fragment of an experimental sample, obtained at a maximum temperature of 1300°C.*

The X-ray phase analysis (Figure 2) revealed the presence of $Ca_3(SiO_3)_3$ pseudowollastonite (PDF 01-089-6485),β-Ca_2SiO_4 (PDF 01-077-0388) and SiO_2 cristobalite (PDF 01-076-0939).

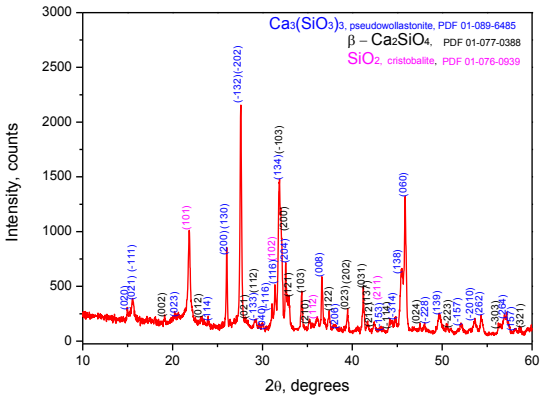


Fig 2. *X-ray phase analysis of an experimental sample, obtained at a maximum temperature of 1300°C.*

The oxide content of the experimental samples was determined (Table 1). The obtained samples showed the presence of oxide impurities in different concentrations (Al_2O_3-1.988%, TiO_2-0.098%, V_2O_5-0.053%, Fe_2O_3-0.071%, SrO-0.248%), which is interpreted as a consequence of the use of waste biogenic raw material and the specificity of the material of the laboratory crucibles used.

Table 1. *Oxide content determined.*

Oxides	Concentration, %
Al_2O_3	1.988
SiO_2	44.950
CaO	52.591
TiO_2	0.098
V_2O_5	0.053
Fe_2O_3	0.071
SrO	0.248

The applied technological approach allows the use of the main capabilities of classical solid-phase synthesis and successful recycling of naturally sustainable waste materials of biogenic origin.

The existing possibilities for potential application of the synthesized polyphase material are determined by the specific characteristics of the established phase composition.

A suitable prospective direction is the use of the material as a full-fledged filler in combination with various polymer compositions or binders.

Compositions prepared on the basis of the synthesized polyphase material and additionally introduced plastic clays allow the molding of blanks with a variety of geometries. The preparation of durable samples is carried out after drying and final high-temperature thermal treatment (according to a developed regime) of the materials.

The considered technological scheme is applicable for obtaining cladding elements, profiles and other products with specific functional characteristics potentially applicable in construction and other technical fields.

The obtained experimental results are a prerequisite for optimizing the used technological regimes and further development of an additional series of compositions. The main technological direction is the implementation of synthesis at lower temperature values and the production of materials with modified polyphase or monophase composition (for a specific target need).

Appropriate technological modifications include the application of mechanochemical activation of the compositions, limited introduction of additional components, modifiers and appropriate technological additives.

At the same time, the introduction of SiO_2 (into the compositions) via a suitable waste raw material (with significant economic importance) is considered a feasible option. This allows the use of a cost-effective and environmentally friendly technological approach based on two waste raw materials, applicable for the introduction of the two oxide components into the compositions.

4. Conclusions

In a summarized form, some of the prevailing trends and prospects regarding the main areas of application of calcium silicate materials are discussed.

Based on waste biogenic $CaCO_3$ and SiO_2, polyphase materials with a dominant presence of calcium silicate phases and a negligible content of silicon dioxide were obtained.

The experimental samples were prepared in laboratory conditions by classical solid-phase synthesis under thermal treatment regimes up to 1300°C and isothermal retention of 1 h. The approach used allows for effective and cost-effective utilization of waste raw material, stable in the natural environment.

The X-ray phase analysis of the obtained samples demonstrated the presence of $Ca_3(SiO_3)_3$ pseudowollastonite (dominant phase), β-Ca_2SiO_4 and SiO_2 (cristobalite).

The presence of impurities (in concentrations from 0.053 to 1.988%) was found in the samples studied, which is due to the use of biogenic waste raw material and the material of the crucibles used.

The recorded phase composition is a fundamental prerequisite for specifying the prospects for potential application of the obtained material. The technological possibilities for the preparation of various products with specific functional characteristics have been analyzed.

Some of the existing opportunities for optimizing the conditions of the technological regimes have been examined, in accordance with certain further priorities.

5. References

1. A. M. Alper (Editor), "Phase diagrams in Advanced ceramics", Academic press, London, 1995.
2. R. B. Heimann, "Classic and advanced ceramics: from fundamentals to applications", John Wiley & Sons, 2010, 573.
3. C. B. Carter, M. G. Norton, "Ceramic materials: Science and engineering", Book, Springer New York, NY, 2016, 766.
4. K. P. Misra, R. D. K. Misra, "Advanced Ceramics", In Ceramic Science and Engineering, 21-43, Elsevier, 2022.
5. W. Holand, G. H. Beall, "Glass-Ceramic Technology", Book, 3rd Edition, Publisher, Wiley-American Ceramic Society, 2019, 448.
6. J. E. Shelby, "Introduction to glass science and technology", 3rd ed., Royal Society of Chemistry, 2020.
7. R. Giordano, "Ceramics overview", British Dent. J. 232(9), 2022, pp. 658-663.
8. B. C. Wyatt, S. K. Nemani, G. E. Hilmas, E. J. Opila, B. Anasori, "Ultra-high temperature ceramics for extreme environments", Nat. Rev. Mat., 2023, pp. 1-17.
9. S. J. Ikhmayies (Editor), "Advanced Ceramics", Book, Publisher Springer Cham, 2024, 303.
10. D. W. Richerson, W. E. Lee, "Modern ceramic engineering: properties, processing and use in design", Book, 4th Edition, CRC Press, 2018, 812.
11. T. A. Otitoju, P. U. Okoye, G. Chen, Y. Li, M. O. Okoye, S. Li, "Advanced ceramic components: materials, fabrication, and applications", J. Industrial and Engineering Chemistry 85, 2020, pp. 34-65.
12. E. Gerasimov, A. Gerasimov, A. Atanasov, V. Toshev, D. Petkov, D. Ivanov, L. Georgieva, L. Pavlova, N. Drenska, P. Vinarov, P. Petrov, S. Buchvarov, S. Panova, S. Bagarov, S. Serbezov, S. Stefanov, S. Djambasov, T. Stoikova, T. Dackova, H. Berlinov, "Technology of ceramic products and materials", Book, Edited by Prof. Dr. S. Buchvarov, IK "Sarasvati", Sofia, 2003, (in Bulgarian).
13. K. Mishagin, E. Gotlib, E. Yamaleeva, A. Sokolova, A. Khatsrinov, "Comparison of the properties of calcium silicates derived from different raw materials", E3S, Web of Conferences 410, 2023, 01001.
14. C. Yang, F. Zhou, Q. Chen, G. Shi, M. M. Kaziana, M. Gasper, "Development and application of modern building ceramic materials", Research and Application of Materials Science ,Vol. 5, No.2, 2023, 25-32.
15. S. Wu, M. Chen (Editors), "Silicate building materials", Book, Trans Tech Publications, 2014, 390.
16. S. Schiavoni, F. D'Alessandro, F. Bianchi, F. Asdrubali, "Insulation materials for the building sector: A review and comparative analysis", Renewable and Sustainable Energy Reviews, Volume 62, 2016, pp. 988-1011.
17. L. Aditya, T. M. I. Mahlia, B. Rismanchi, H. M. Ng, M. H. Hasan, H. S. C. Metselaar, Oki Muraza, H. B. Aditiya, "A review on insulation materials for energy conservation in buildings", Renewable and Sustainable Energy Reviews, Vol. 73, 2017, pp. 1352-1365.
18. M. B. Revuelta, "Construction Materials, Geology, Production and Applications", Publisher Springer Cham, 2021, 602.
19. A. K. Chatterjee, "Cement Production Technology, Principles and Practice", Book, 1st Edition, Pub. Location Boca Raton, Imprint CRC Press, 2018, 439.
20. R. A. Youness, D. M. T. El-deen, M. A. Taha, "A Review on calcium silicate ceramics: properties, limitations, and solutions for their use in biomedical applications, Silicon, 15, 2023, 2493-2505.
21. M. Georgieva, Lakov, L., Jivov, B., Gacheva, M., "Synthesis of calcium silicates based on calcium oxide and quartz glass". International Journal "NDT Days", Volume VII, Issue 1, 2024, pp. 7-13.
22. E. Amasuomo, J. Baird, "The concept of waste and waste management", J. Manag. Sustain., 6, 4, 2016, 88-96.
23. A. P. M. Velenturf, P. Purnell, "Resource recovery from waste: Restoring the balance between resource scarcity and waste overload", Sustainability, 9, 9, 2017, 1603.
24. F. Medici, "Recovery of waste materials: technological research and industrial scale-up", Materials, 15, 685, 2022, 1-3.
25. A. Trinca, V. Segneri, T. Mpouras, N. Libardi, G. Vilardi, "Recovery of solid waste in industrial and environmental processes", Energies, 15, 2022, 7418.

Increasing the Durability of Agricultural Working Bodies by Creating Nanostructured Coatings Using Plasma Jet Spraying

Corneliu Munteanu[1], Iurie Melnic[2*], Bogdan Istrate[1], Fabian Cezar Lupu, Vitali Vișanu[2], Constantin Zîrnescu[2], Vladimir Badiul[2]

[1] "Gheorghe Asachi" Technical University of Iasi, 700050 Iasi, Romania
[2] Technical University of Moldova, 168, Ștefan cel Mare Blvd., Chișinău, Republic of Moldova
*iurie.melnic@im.utm.md

Abstract: *The article reveals a new method that relates to the treatment of active surfaces of agricultural working bodies, in particular harrow discs, by applying nanostructured coatings using atmospheric plasma jet spraying (APS). The process consists of preparing the surface by corundum blasting at a pressure of 5.5 bar, followed by preheating to 150°C and depositing a nanostructured powder of the WC-Co 88/12 type.*

The technical novelty lies in the synergetic optimization of the deposition parameters: current intensity of 550 A, hydrogen flow rate of 9 L/min, spraying distance of 100 mm and a high scanning speed of 500 mm/s, under forced post-deposition cooling.

The technical result obtained by applying this process consists of creating a protective layer with porosity below 1.2%, adhesion of over 65 MPa and a hardness of 1150-1250 HV0.3, ensuring an increase in the durability of the working element of up to 2.8 times under conditions of severe abrasive wear.

Keywords: *DURABILITY, WEAR PERFORMANCE, AGRICULTURAL WORKING TOOLS, PLASMA-JET SPRAYING.*

Introduction

Agricultural machinery production is constantly evolving. At the same time, methods and techniques for producing the best parts and working components for performing various mechanized technological operations under challenging conditions are also being refined.

Increasing the durability of agricultural working tools of farming machines, such as plows, harrows, cultivators, seeders, etc. is one of the main problem areas in production of agricultural machinery. As a result of soil cultivation these machines are subject to severe abrasive wear.

Analysis of plasma-jet spraying on the active part of working tools of agricultural machines allows to evaluate the resistance to abrasion and corrosion. So, the use of such working bodies increases productivity, reduces costs and ensures the main good results in modern agriculture [1, 2].

Formulation of the problem

To ensure efficient soil cultivation and improve the quality of technological processes, the working parts of agricultural tillage machines must be highly wear-resistant. However, during soil cultivation, the active elements of all tillage machines (including disc harrows) are often subject to significant wear due to abrasive soil particles.

It should be noted that these working elements must have significant impact resistance [3, 4].

A known process for hardening the working parts of agricultural machinery is the use of traditional material heat treatments (quenching and tempering) applied to 65G steel or boron-alloyed steels, achieving a hardness of approximately 48-52 HRC [5].

The proposed technical solution for hardening the agricultural working parts has several drawbacks:

1) limited resistance to severe abrasive wear in heterogeneous soils;

2) rapid changes in the geometry of the harrow disc cutting edge;

3) the need for frequent replacement of parts, which increases operating costs.

During 2024-2026 it was conducted tests of disc harrows in accordance with the current standards for testing agricultural machinery and their working parts [6, 7, 8]. It means also using of efficient methods to improve needed parameters.

Analysis of recent research and publications

All agricultural working bodies wear out faster as the amount of sand particles in the soil increases, which requires improving the mechanical properties of the surfaces of the processed working elements [3, 4].

That assumes a relationship between the wear of the active area of the working parts of the machine, the size of the sand particles and the optimization of their mechanical properties to increase the wear resistance of the working bodies of agricultural machinery which is crucial for increasing the service life of the active areas [5, 6].

Therefore, the active area of the working bodies, especialy of tillage machines must have significant impact resistance [1, 4, 6]. It means using effective methods to improve the parameters of the active surface of the working bodies of agricultural machinery, and subsequently conducting tests of these machines in accordance with current standards for testing.

Plasma-jet thermal spray deposition is one of the effective methods for improving the main parameters of the working elements material of machines for farming, considered an advanced method capable to achieve high-quality surface depositions [5, 7].

Currently, the application of this method is generally limited to coatings up to 100 μm [8, 9].

Another process of thermal spraying deposition in atmospheric plasma jet (APS) of tungsten carbide (WC-Co) or ceramic mixtures (Cr2O3-SiO2-TiO2) powders is known, using standard operating parameters according to the technical data sheets of powder manufacturers, [1, 7, 10].

To improve the microstructural and tribological properties of coatings on the active areas of studied harrow discs and the quality of the agricultural working bodies, three types of coatings were applied to the active areas of the discs [7, 8]:

- W_2C/WC12Co (Metco71NS);
- Cr_2O_3-4SiO_2-3TiO (Metco136F);
- Co25.5Cr10.5Ni7.5W0.5C (Metco45CNS).



Figure 1. Atmospheric plasma jet thermal spraying coating process

Experimental coatings on harrow discs were applied using a Sulzer Metco 9MCE deposition system operating on Ar (5.3 bar, 45 Nl/min) and H_2 (3.5 bar, 7.0 Nl/min).

After mechanical grinding and intensive sandblasting, samples with thermally applied APS were tested on the active areas of the harrow discs of the working parts of agricultural disc harrows.

The experimental setup for the study included a rotating support, an automated arm connected to a Sulzer 9MB sprayer, and a sample holder (Fig. 1).

In order to to determine the main parameters of the material of the studied coatings obtained by thermal spraying with an atmospheric plasma jet, such as adhesion to the substrate, coefficient of friction (COF), Young's modulus (modulus of elasticity), rigidity (stiffness) and hardness a tribological analysis was carried out.

Tribological tests were held by a group of researchers from the Technical University of Moldova (Republic of Moldova) and the Technical University "Gheorghe Asachi", Iasi (Romania) in a specialized laboratory of the Technical University "Gheorghe Asachi", Iasi, Romania (Fig. 2).



Figure 2. Conducting tribological tests in the laboratory of Technical University „Gheorghe Asachi", Iasi, Romania

In these conventional solutions, the thermal regime is optimized for general depositions, without taking into account the specifics of abrasive stresses in heterogeneous agricultural soils.

The technical solution presented has the disadvantage that standard sputtering processes (characterized by low scanning speeds of 200-300 mm/s and large sputtering distances of over 120 mm) often lead to thermal degradation of carbides through the decarburization phenomenon [5, 7].

During the flight of particles in the plasma jet with temperatures exceeding 10,000 K, the hard WC (tungsten carbide) phase decomposes into more brittle and less hard phases, such as W2C or metallic tungsten. This chemical and structural transformation process results in a layer with high porosity (above 2-3%) and a coarse microstructure.

Excessive porosity allows moisture and acids from the soil to penetrate, leading to corrosion of the interface between the layer and the substrate, which causes premature exfoliation of the coating. Also, structural degradation limits the hardness of the layer below the threshold of 1000 HV, an insufficient value to ensure long-term protection against silica (quartz) fractions present in the soil, which have a comparable or higher hardness.

The purpose of the innovation is to increase the durability and resistance to abrasive wear of agricultural working bodies by creating a coating with a nanometric, dense and ultra-hard structure, without affecting the mechanical properties of the metal substrate.

Rezults and discussion

The stated problem is solved by using plasma-jet spraying to produce a nanostructured coating, which involves strict heat transfer control using a current of 550 A, a hydrogen flow rate of 9 L/min and a high scanning speed of 500 mm/s at a distance of 100 mm. This ensures a particle temperature sufficient to melt the binder phase without degradation of the nanometric carbide cores, resulting in a layer with a porosity of less than 1.2% and a hardness exceeding 1150 HV0.3.

The essence of the innovation consists in solving the problem of increasing durability of active areas of agricultural working bodies by applying a well-studied technological regime that allows preserving the nanometric structure of the WC-Co powder (type Metco 71NS or similar) in the deposited layer.

The technical result is that the process of producing nanostructured coatings by plasma jet spraying to increase the durability of agricultural working elements ensures obtaining a hardness of 1150-1250 HV0.3, 20-30% higher than standard methods, reducing the porosity of the layer below 1.2-1.5%, preventing the infiltration of corrosive agents from the soil and increasing the service life of metal working elements by up to 3 times in abrasive soil conditions.

The peculiarities of the process of making nanostructured coatings are ensured by a researched technological regime and can be applied by selecting as the base material a working element with a metallic surface (disks, cutters, knives, blades) made of boron alloyed steel (27MnCrB5) or spring steel (65G), having a thickness of 4-6 mm.

The actual deposition is performed using an atmospheric plasma spraying installation, fed with a nanostructured powder of the WC-Co 88/12 type (cobalt cemented tungsten carbides), with an average carbide crystallite size below 500 nm.

The working parameters used to obtain the nanometric structure are:

- electric current intensity: 550 A;
- arc voltage: 65-70 V;
- primary plasma gas flow rate (Argon): 45 L/min;
- secondary plasma gas flow rate (Hydrogen): 9 L/min;
- spraying distance: 100 mm;
- torch scanning speed: 500 mm/s.

By applying this process, a protective layer with a thickness of 250-300 μm is obtained, characterized by a porosity of 1.1% and an average microhardness of 1210 HV0.3. Laboratory tests (according to ASTM G65 standard) have demonstrated a reduction in mass loss through abrasive wear of 2.8 times compared to untreated discs and an increase in the adhesion of the layer to the support of up to 68 MPa.

Further research

Further research into ways to increase the durability of agricultural machinery by creating nanostructured coatings using plasma jet spraying relates to substantiating the application modes and parameters for APS coatings and conducting further experiments directly related to the working parts of transplanting machines and seeders [11, 12, 13].

Acknowledgments

This work and research were supported by a grant from the Romanian Ministry of Education and Research, CNCS-UEFISCDI, project number PN-IV-P8-8.3-ROMD-2023-0108, within the PNCDI IV.

Conclusions

1. Morphological analysis of the studied coatings W_2C/WC12Co (Metco71NS), Cr_2O_3-4SiO_2-3TiO (Metco136F) and Co25.5Cr10.5Ni7.5W0.5C (Metco45C-NS), applied to the active surface of harrow disks using the atmospheric plasma spraying method, revealed shortcomings that allowed us to draw conclusions regarding the spraying process and methods for improving operating parameters.

2. A study of coated samples followed by tribological analysis of surface scratches on three groups of samples revealed shortcomings and next steps for improving the atmospheric plasma spray (APS) thermal deposition process.

3. The features of the process of manufacturing nanostructured coatings are provided by the studied technological regime and can be implemented by choosing as the main material of the working element with a metal surface (discs, cutting elements, knives) on such agricultural machines as plows, scaricators, disc harrows, seeders, transplanting machines, etc. made of boron-alloyed steel (27MnCrB5) or spring steel (65G) with a thickness of 4-6 mm.

4. Excessive porosity of the coatings obtained using the studied APS modes allows moisture and acids from the soil to penetrate inside, causing corrosion of the interface between the layer and the substrate, which leads to premature delamination of this coating. Also, structural degradation limits the layer hardness below the threshold of 1000 HV, which is insufficient to provide long-term protection against silica fractionspresent in the soil, that have comparable or higher hardness.

5. The innovative proposal involves the actual deposition being carried out using an atmospheric plasma spraying unit, into which nanostructured powder of the WC-Co 88/12 type (tungsten carbides bonded with cobalt) with an average carbide crystallite size of less than 500 nm is fed.

6. The operating parameters and modes of the system used to produce the nanometric structure are as follows:

- Electric current: 550 A;
- Arc voltage: 65-70 V;
- Primary plasma gas flow rate (argon): 45 l/min;
- Secondary plasma gas flow rate (hydrogen): 9 l/min;
- Spray distance: 100 mm and torch scanning speed: 500 mm/s.

7. By applying the proposed process of atmosferic plasma spray termal deposition, a protective layer with a thickness of 250-300 μm is obtained, characterized by a porosity of 1.1% and an average microhardness of 1210 HV0.3.

8. Theoretical studies and laboratory tests (in accordance with the ASTM G65 standard) have shown a reduction in mass loss due to abrasive wear by 2.8 times compared to untreated discs and an increase in layer adhesion to the substrate to 68 MPa.

References

1. MUNTEANU, C., MELNIC, IU., ISTRATE, B., HARDIMAN, M., GAIGINSCHI, L., LUPU, F., ARSENOAIA, V., CHICET, D. ZÎRNESCU, C., BADIUL, V. A Comprehensive Review of Improving the Durability Properties of Agricultural Harrow Discs by Atmospheric Plasma Spraying (APS). In: Coatings 2025, 15(6), 632; ISSN 2079-6412.
https://www.mdpi.com/search?q=&journal=coatings&sort=pubdate&page_count=50

2. MUNTEANU, C., MELNIC, IU., ISTRATE, B., LUPU, F., M., VIȘANU, V. Study of harrow discs coated by plasma-thermal method. *XIII International Scientific and Technical Congress "AGRICULTURAL MASHINERY"* 25.06-28.06 2025, Varna, Bulgaria. In: *International Scientific Journal "Mechanization in agriculture & Conserving of the resources", Vol. 69 (2025), Issue 2, pg(s) 46-49.* ISSN print 2603-3704, ISSN web 2603-3712.
https://repository.utm.md/bitstream/handle/5014/35970/Journal-Mechanization-Agriculture-Conserving-Resources-2025-V71-nr2-p46-48.pdf?sequence=1
https://stumejournals.com/journals/am/2025/2/46

3. MUNTEANU, C., MELNIC, IU., ARSENOAIA, V., ISTRATE, B., LUPU, F., VIȘANU, V., ZÎRNESCU, C., BADIUL, V. Wear Performance of Agricultural Harrow Discs Coated by Plasma-Jet Thermal Deposition. XXIII International Scientific Congress "MACHINES. TECHNOLOGIES. MATERIALS", 25-28.03.2026, Borovets, Bulgaria. In: International Journal for Science, Technics and Innovations for the Industry „MACHINES. TECHNOLOGIES. MATERIALS", Vol. 20 (2026), Issue 3, pg(s) 81-84. ISSN PRINT 1313-0226, ISSN WEB 1314-507X.
https://repository.utm.md/bitstream/handle/5014/35967/Journal-Machines-Technologies-Materials-2026-V20-nr3-p81-84.pdf?sequence=3

4. BARZEGAR, M., HASHEMI, S., NAZOKDASTB, H. Evaluating the draft force and soil-tool adhesion of a UHMW-PE coated furrower. In: Soil Tillage Res., Vol. 163, 2016. pp. 160-167.

5. BÎRSAN, I., SĂNDULACHE, C. Cercetări privind uzura abrazivă a oțelurilor pentru agricultură. Buletinul Tehnic ISIM, vol. 12, pp. 45-50, 2023.

6. MUNTEANU, C., ISTRATE, B., LUPU, F., BENCHEA, M., MELNIC, IU., VIȘANU, V. Increasing the Mechanical Characteristics of the Disc Harrow Component by APS Thermal Coatings. In: Thermal Spray 2025: Proceedings from the International Thermal Spray Conference May 6–8, 2025; Vancouver, Canada. Vancouver: Published Online: May 05 2025, Paper No: itsc2025fm01, pp. iii-v; 3 pages. pp. 508-514.
https://doi.org/10.31399/asm.cp.itsc2025p0508

7. ARSENOAIA, V., MUNTEANU, C., LUPU, F., ISTRATE, B., LUPU, F., BENCHEA, M., MELNIC, IU. Field Performance and Wear Behavior of Atmospheric Plasma Spraying (APS) Coated Discs Used in Agricultural Disc Harrows. In: Agriculture 2026, 16(1), 114; ISSN 2077-0472.
https://ibn.idsi.md/sites/default/files/imag_file/agriculture_16-00114-v2%20%281%29_compressed.pdf

8. MUNTEANU, C., MELNIC, IU., ISTRATE, B., BENCHEA, M., BADIUL, V., ZÎRNESCU, C. Tribological Analysis of Plasma Spray Thermal Deposition on the Active Area of Harrow Discs. X International Congress "Industry 4" 10-13.12.2025, Borovets, Bulgaria. In: International Journal for Science, Technics and Innovations for the Industry „MACHINES. TECHNOLOGIES. MATERIALS", Vol. 19 (2025), Issue 12, pg(s) 466-469. ISSN PRINT 1313-0226, ISSN WEB 1314-507X.
https://repository.utm.md/bitstream/handle/5014/35975/Journal-Machines-Technologies-Materials-2025-V19-nr12-p466-469.pdf?sequence=1

9. MUNTEANU, C., CIMPOIESU, R., LUPU, F., NAZAR, B., ISTRATE, B., MELNIC, IU., VIȘANU, V. Corrosion and Thermal Shock Behavior of Atmospheric Plasma Spraying Coatings on Agricultural Disc Harrows. In: Applied Sciences 2026, 16(8), 3703; ISSN 2076-3417.
https://www.mdpi.com/2076-3417/16/8/3703

10. MUNTEANU, C., TUFESCU, A., LUPU, F., ISTRATE, B., BENCHEA, M., MELNIC, IU., VIȘANU, V., ARSENOAIA, V. Explicit FEM Analysis of Soil-Disc Interaction for APS-Coated Notched Harrow Discs in Representative Agricultural Soils. In: Applied Sciences 2026, 16(1), 395; ISSN 2076-3417.
https://www.mdpi.com/2076-3417/16/1/395

11. MELNIC, IU., MELNIC, V. Mathematical modeling of the operating system of the carousel type transplanting machine. III International Scientific Conference "Mathematical modeling", Borovets, Bulgaria, 11-14 decembre 2019. In: International Scientific Journal "Mathematical modeling", Vol.3, Issue 4. 2019. pp.124-126, Print ISSN 2535-0986, Web ISSN 2603-2929.
https://stumejournals.com/journals/mm/2019/4/124

12. MELNIC, IU., SCLEAR, P. Theoretical research of tractive resistance of rotary type seeders. VII International Scientific Congress "Agromachinery" Burgas, 26-29 june 2019. In: International Scientific Journal "Mechanization in agriculture & Conserving of the resources", nr.3. 2019, pp.85-87, ISSN print 2603-3704, ISSN web 2603-3712.
https://stumejournals.com/journals/am/2019/3/85

13. MELNIC, IU., BADIUL, V., MELNIC, V., CĂTANĂ, M. Study of the technological process of operation of transplanting machines. XII International Scientific and Technical Congress "AGRICULTURAL MASHINERY" 26.06-29.06 2024, Varna, Bulgaria. In: International Scientific Journal "Mechanization in agriculture & Conserving of the resources", Issue 2, 2024. pp.30-32. ISSN print 2603-3704, ISSN web 2603-3712.
https://stumejournals.com/journals/am/2024/2/30